THESIS

EVALUATION OF NEW REACTIVE FRP REINFORCEMENT ASSEMBLIES FOR REINFORCED CONCRETE TRANSPORTATION STRUCTURES

Submitted by

Christopher Bright

Department of Civil and Environmental Engineering

In partial fulfillment of the requirements

For the Degree of Master of Science

Colorado State University

Fort Collins, Colorado

Summer 2014

Master's Committee:

Advisor: John van de Lindt
Co-Advisor: Rebecca Atadero

Donald Radford

ABSTRACT

EVALUATION OF NEW REACTIVE FRP REINFORCEMENT ASSEMBLIES FOR REINFORCED CONCRETE TRANSPORTATION STRUCTURES

This thesis evaluates two new glass-fiber reinforced polymer concrete reinforcement systems which have been designed to serve as a non-corrosive alternative to steel reinforcement in reinforced concrete bridge girders. Due to the nature of the reinforcement geometry, these systems react in a way to introduce compressive confinement into the concrete in the inner regions of the system units. The introduction of this compressive confinement zone will increase particle interaction effects which results in increased shear and tensile force resistance contributed by the affected concrete. The system is also well integrated into the surrounding concrete matrix, therefore eliminating the potential for debonding failures. A proof of concept is conducted in order to evaluate a set of alternative reinforcement system prototypes. Before the reinforcement systems are evaluated, technical literature pertaining to alternative reinforcements is reviewed.

Select specimens provided evidence of sufficient mechanically constrictive behavior. Indications of good bond strength and shear strength contribution from the flexural reinforcement systems were also found. Parameters which control the structural behavior of the reinforcement system were identified.

TABLE OF CONTENTS

LIST OF TABLES

LIST OF FIGURES

Chapter 1

Introduction

Fiber reinforced polymer (FRP) composites have been progressively implemented into construction practices for reinforced concrete (RC) structures over the past several decades. This is largely in response to the demand for non-corrosive alternative reinforcements needed to avoid the ever expanding problem of corrosion damage in conventional steel bar concrete reinforcement (rebar). While corrosion is a potential problem for nearly all steel RC members, it affects transportation structures to a greater degree, due to unprotected weather exposure in combination with the practice of applying deicing chlorides to road surfaces. Approximately 15% of the RC bridges in the United States have been deemed structurally deficient as a result of reinforcement corrosion alone (Koch *et al.* 2001). The design life of many of these bridges is approaching, so expensive rehabilitation or even total replacement will likely be needed. The projected cost of these repairs have been estimated to approach $8.3 billion dollars (Koch et al., 2001). By using non-corrosive materials as an alternative to steel, the deterioration that leads to this costly maintenance can be avoided for future structures.

The application of FRP as a non-corrosive reinforcing material for concrete transportation structures is used in various ways. Internal reinforcement, acting as a direct replacement for steel rebar, is sometimes used for new construction. One example of such an application is the Cookshire-Eaton bridge in Quebec, Canada, which demonstrates the use of GFRP bars as primary bridge deck reinforcement (El-Salakawy, et al. 2005). However, FRP is also commonly used as a post-construction strengthening tactic for existing structures exhibiting early structural deficiencies or requiring increased strength.

FRP presents many advantages, such as providing greater tensile strength than steel, it is lightweight (one-sixth to one-fourth the density of steel), allowing for easier transport and placement (ACI Committee 440, 2006). Using FRP also yields an environmental impact reduction of about 50%, as compared to steel from manufacturing to demolition and reuse (Katz, 2004).

Despite the advantages of its non-corrosive nature, internal FRP reinforcement has received limited acceptance from the construction and engineering community since there is still little common knowledge and experience for its use in RC structures (Porter & Harries, 2007). Other issues seem to impede acceptance as well. For example, there is currently a lack of uniformity between commercial manufacturers, which makes reliable design difficult with varying properties and deformation geometries. FRP reinforcement also typically has a higher initial cost (Okelo & Yuan, 2005). The ductility of steel allows for yielding before failure, which acts as an early indicator to complete failure. However, ductility is not exhibited in FRP, and this is often viewed as a disadvantage of this material. The stress-strain behavior of FRP is nearly linear, which means that tensile failure of FRP reinforced concrete is more sudden than that of steel reinforced concrete.

Using a new kinematically active FRP reinforcement system, this research develops a reinforcement solution to some of the intrinsic issues that have limited the use of FRP as internal concrete reinforcement in new transportation structures. By imparting compressive forces to surrounding concrete, the shear strength can be improved due to forced confinement effects (Ahmed, El-Salakawy, & Benmokrane, 2010). The bond strength is also improved with the use of complex reinforcement geometries that promote good incorporation of the reinforcement structure into the surrounding concrete matrix.

Two types of kinematically active GFRP reinforcement systems are evaluated in this research. The first of which is referred to as Type II reinforcement and is an assembly composed of six intertwining helical cords of FRP (3 CW and 3 CCW). When deflection occurs in the tensile zone of the concrete beams, this assembly shows constrictive behavior similar to that of an arterial stent. (Kleinstreuer, et al. 2008) The other reinforcement system (Type III) is a mat consisting of several FRP cords cast in a sinusoidal shape, and paired together with opposing patterns. The opposing pairs are then arranged in an interlocking fashion. As these cords are forced to “straighten” from beam deflection and tensile forces, the cords impart opposing lateral forces through the adjacent concrete matrix. These opposing forces should create a localized constriction effect in the concrete as well.

1.1 Objectives

The primary goal of this research is to explore the possible advantages of manipulating FRP geometry in a way to address typical issues that have historically contributed to limited use of FRP in RC structures. Specifically, the work described in this thesis addresses the following objectives:

Objective 1: Experimentally observe and measure the increase of flexural and shear strength achieved in the beam specimens, as compared to a control specimen using conventional FRP reinforcement.

Objective 2: Characterize changes in the deflection behavior of the beam, as compared to a control specimen using conventional FRP rebar.

Objective 3: Observe bond strength effects, as compared to a control specimen using conventional FRP bar reinforcement.

1.2 Concept

The concept design of the proposed reinforcement system intends to improve upon the functionality of concrete reinforcement. The following components of reinforcement strength and performance are addressed by this design:

- Tensile reinforcement strength
- Shear contribution of flexural reinforcement
- Bond strength

These components are addressed by different aspects of the reinforcement geometry. The traits of the geometric properties are similar for the two proposed specimen reinforcement systems.

1.2.1 Tensile Strength

Concrete found in the tensile region of traditional reinforced concrete beams contributes little to beam strength after cracking occurs. Tensile loading is primarily resisted by the reinforcing bars, while the primary function of the surrounding concrete is to serve as a protective barrier for the reinforcement and hold it at an adequate position to adequately resist tensile forces. The concept design of the proposed reinforcement configuration utilizes portions of the concrete in the tensile region for flexural strength contributions.

Internal static friction forces at crack interfaces are increased through the application of constriction in the off-axis direction of the beam. This is achieved through the design of the reinforcement geometry which compresses its shape when tension is applied. The reinforcement systems achieve “constrictive zones” with specific kinetically reactive geometries that exhibit a collapsing behavior when axial forces are applied. The tension in the reinforcement causes the curvature of the reinforcement cords to straighten. When these cords are confined by a rigid matrix, such as concrete, the matrix is forced into compression. The anticipated location of the constriction zone areas are shown by the blue shapes in the illustration in Figure 1. As can be seen in Figure 1, they are assumed to be circular in nature for simplicity (and computational purposes) but may have a different shape in reality.

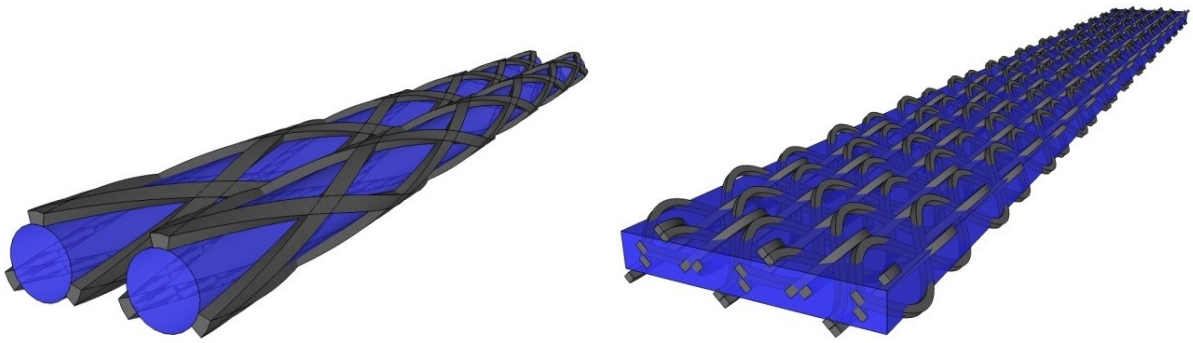

Figure 1: Theoretical constriction zone locations

The compressive forces create increased normal stresses at crack interfaces, which subsequently increase the interfacial static friction, promoting stiffness of the concrete in tension. A network of the interacting cement and aggregate particles link to form a loading path for a portion of the tensile forces to be carried by the concrete in the compression zone. With concrete contributing to tensile strength, the reinforcement is relieved of some loading, increasing the overall capacity of the system. This action is demonstrated in Figure 2. The axial tensile loading of the beam in flexure is shown by the black arrows, while the constrictive force of the reinforcement reaction is shown by the gray arrows. Representative interaction forces (normal and shear) are indicated at the crack interface.

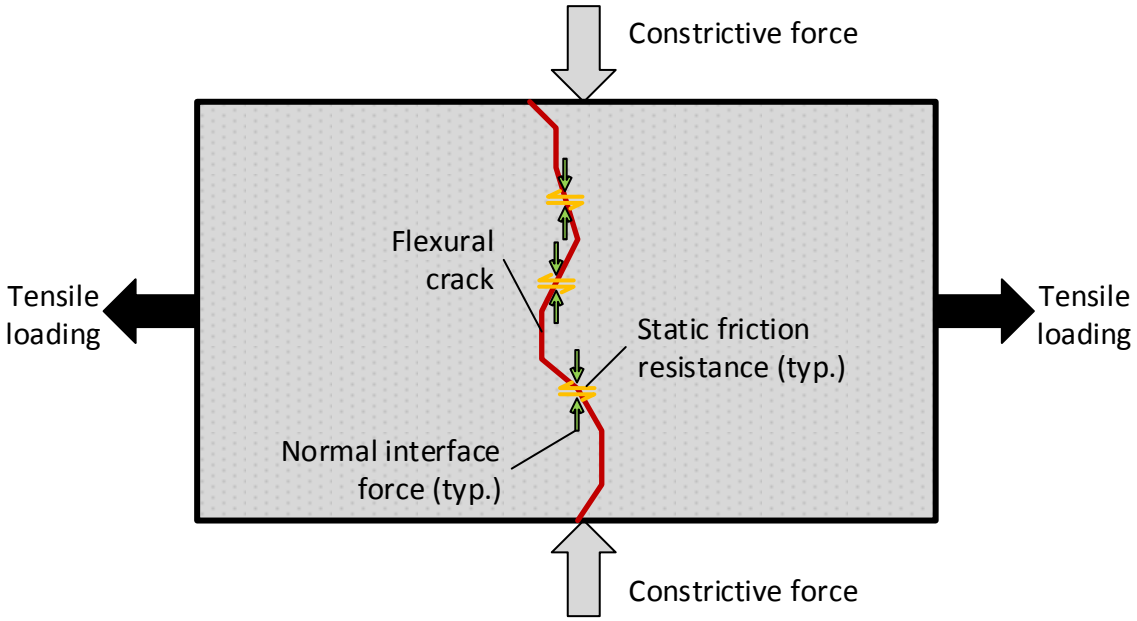

Figure 2: Constriction contribution to flexural strength

1.2.2 Shear Strength

The vertical travel component of the proposed reinforcement system will also provide contribution to shear strength. According to ACI 440.1R-06 “Guide for the Design and Construction of Structural Concrete Reinforced with FRP Bars” (2006), “Orientation of the fibers in an off-axis direction across the layers of fiber will increase the shear resistance, depending upon the degree of offset”. Therefore, the components of the reinforcement crossing the shear cracking interface will take on a portion of the shear stress in its strong axis, as the diagram in Figure 3 demonstrates. This is expected to be reasonably stronger than the typical dowel action strength that is observed with straight-rod reinforcement. The portion of this shear stress that is taken depends at what orientation the cord and shear interface intersect. With a cross-helical or multi-wave configuration, this advantageous alignment is possible in most shearing orientations regardless of where cracking occurs along the reinforcement.

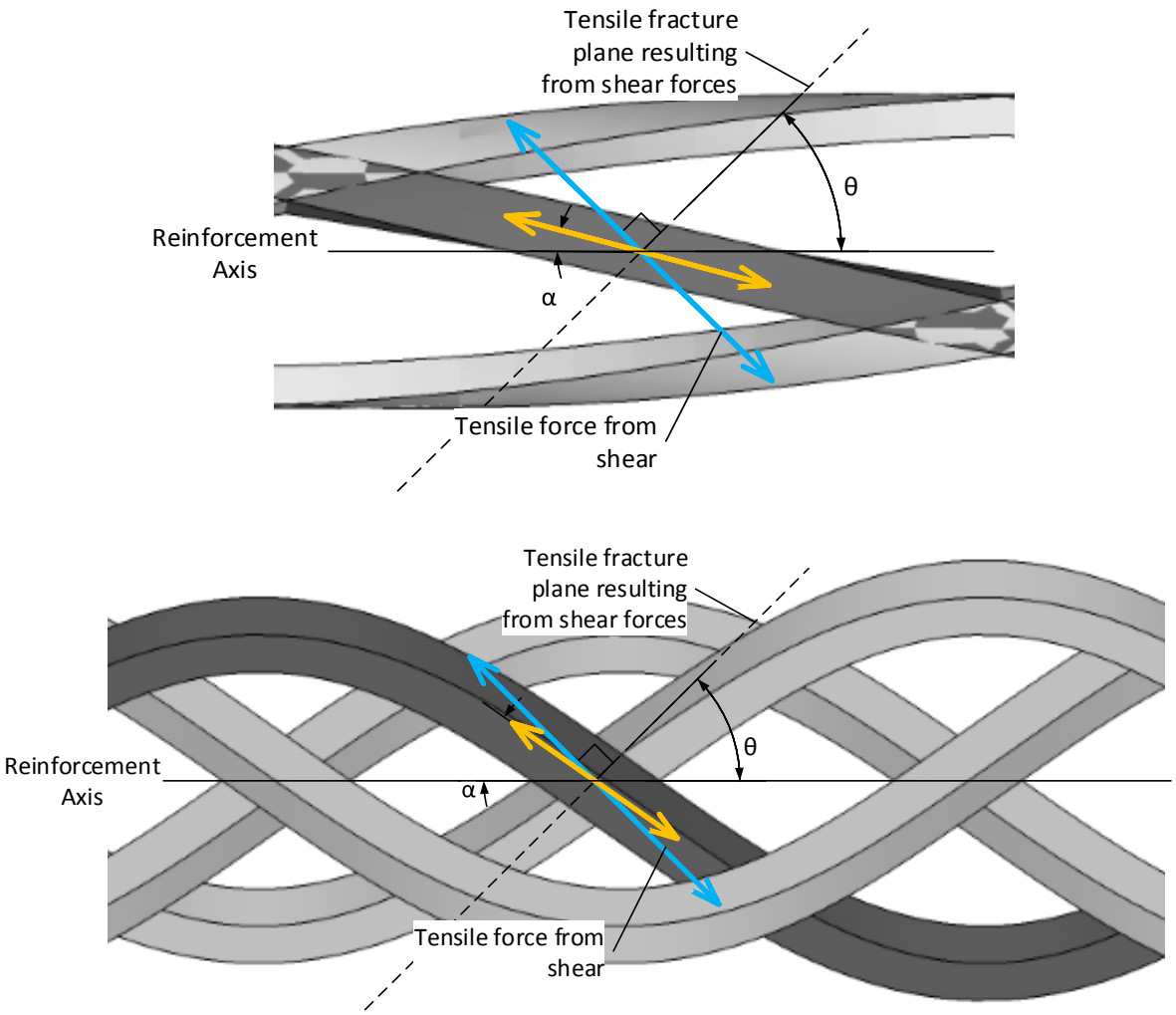

Figure 3: Shear strength mechanics of concept flexural reinforcement

Contributions to shear strength also result from the aforementioned constrictive action described in section 1.1.1. The constrictive action is anticipated to help bind together the cracked concrete of the beam as well as increase the shear friction forces at the shear cracking interface. A diagram of these forces is shown in Figure 4.

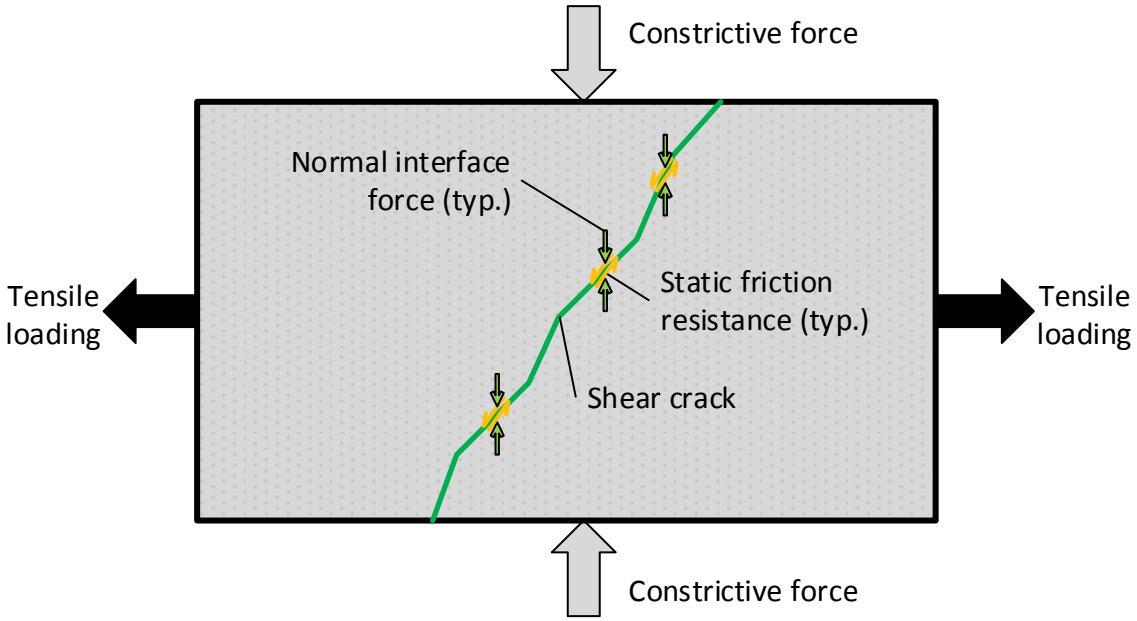

Figure 4: Constriction contribution to shear strength

1.2.3 Bond Strength

Current applications of internal FRP reinforcements exhibit highly variable bond strength due to the high variability of deforming techniques (e.g. sand-coating, fiber wrapping, resin deformations, etc.) and material properties (Harajli & Abouniaj, 2010). This issue is addressed by the proposed reinforcement system by the high integration of the reinforcement geometries into the surrounding concrete matrix. Rather than relying on shear forces at the surface treatments of the reinforcement for bond strength, the shape of the reinforcement resists pull-out forces directly at the “saddle” region shown in red in Figure 5.

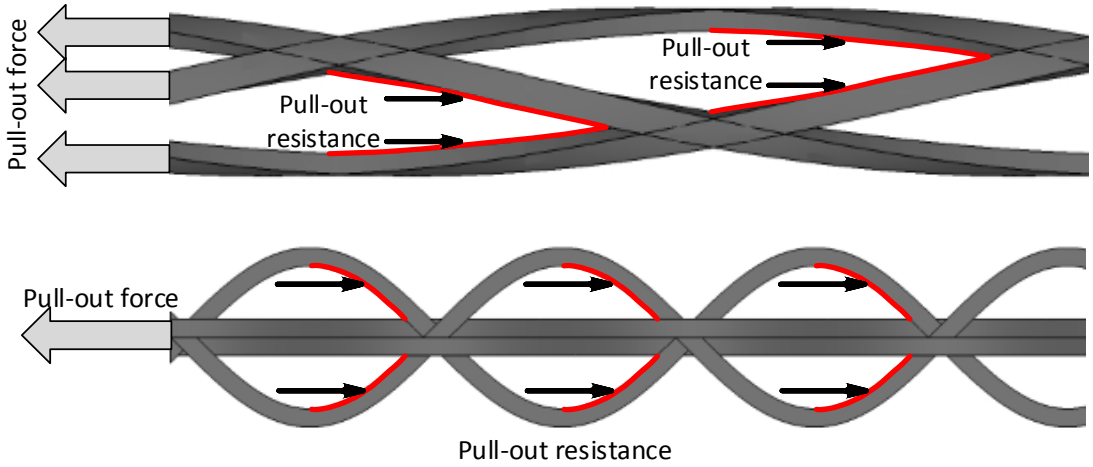

Figure 5: Mechanical bond reactions of helical (upper) & wave (lower) reinforcement

1.3 Methodology

The experimental phase of this project consisted of the fabrication and testing of twelve model beam specimens. Each specimen was laid out as a simply supported specimen with a third-point loading configuration. The beam specimen was monitored for deflection, reinforcement strain, and applied forces in order to determine general structural behavior of the new system. Specimens are also compared with traditional FRP straight bar reinforced beams of a similar design. Each type of specimen was fabricated with and without shear reinforcement in order to provide isolated performance of failure modes in shear and flexure. The results of the testing procedures are then used for a cross-examination of performance in order to determine unique structural traits, performance controlling parameters, and fitness for structural application. The failure modes observed in the specimens are then used to validate the concept design and make recommendations as to whether a more comprehensive quantitative study should be undertaken.

1.4 Organization of Thesis

This thesis is divided into five chapters. The first and current chapter introduces the concept and investigates the demand for alternative reinforcement development. This is followed by the literature review (Chapter 2) which summarizes the background of composite development, as well as the state of current research and guideline publications involving the use of GFRP materials as primary alternative reinforcement. Know characteristics of commercially available GFRP reinforcement that is relevant to the concept reinforcement system is then reviewed. This is followed by a review of studies performed on other proposed composite based alternative reinforcement systems. A summary is then provided on studies involving composites with similar fiber geometry to the reinforcement system. This chapter is concluded with coverage of the mezzo-scale behavior of the concrete under the proposed loading configuration from the constriction action of the concept reinforcement system.

The Chapter 3 outlines the methods used to design, fabricate, and evaluate the concept reinforcement system. This begins with a description of the acquisition of the material properties used for the design and analysis of the GFRP reinforced concrete specimens. The design procedures of the specimen beams are then described in detail. This is followed by a description of the fabrication

processes of all of the GFRP reinforcement components along with a description of the beam casting procedures. Details of the instrumentation of the beam specimens are then described. Finally, a description of the testing procedures is provided.

Chapter 4 provides a detailed description and interpretation of the results of the experimental testing. This is organized beginning with the chronological outline of testing events highlighting correlations between loading, deflection, and strains with visible beam cracking and failures. General deflection behaviors are then analyzed with attention given to beam stiffness. Exploration of internal concrete damage observations are then described in a section on the section analysis of one of the specimen beams. The reinforcement strain behavior is then described and interpreted. A comparative analysis of the beam specimens is then presented at the end of the chapter.

The final Chapter (5) presents the conclusions, contributions, and recommendations of future work for continuing investigations of this reinforcement concept.

Chapter 2

Literature Review

2.1 Background

The use of composite fibrous material has taken many roles in other fields and applications before it slowly became accepted as a concrete reinforcement alternative. With its initial development near the end of World War II fiber reinforced polymer (FRP) composites have a strong beginning in the aerospace industry, where they are still widely used today. The first US Department of Transportation funded project in 1988 entitled “Transfer of Composite Technology to Design and Construction of Bridges” was carried out by Plecnik and Ahmed (ACI Committee 440, 2006). This pioneering research preceded an expansion in further investigation of FRP reinforced structures, which has collectively produced several codes and guidelines for FRP reinforced concrete design. This recent interest in the implementation of FRP reinforcement for concrete structures is supported by various studies of the economic and environmental benefits offered by FRP.

2.1.1 Research Trends

Research topics that investigate FRP use for reinforced concrete are disproportionately greater in the repair/retrofit fields. Internal FRP reinforcement research seems to trend mostly towards bridge deck applications, bond properties, and shear behavior of FRP reinforced beams.

In 2004, an NSF-sponsored workshop was held in order to identify past trends and future needs for FRP research. This workshop concluded that for more thorough acceptance and utilization of FRP reinforcements research topics should focus on solving issues primarily related to durability and performance. It also addressed the importance of the advancement of new materials and system designs (Porter & Harries, 2007). The system designs being called for could include the innovative reinforcing schemes presented in this research.

2.1.2 Active Building Codes and Design Guidelines

Due to the anisotropic nature and high tensile strength of FRP, proprietary design guidelines must be followed for a successful reinforced concrete system. There are currently only a few publications dedicated to providing specifications for the use of FRP as concrete reinforcement. Some of the major organizations that have produced such documents in recent years are; the Japanese Society of Civil Engineers (JSCE), the Canadian Standards Association (CSA), and the American Concrete Institute (ACI).

Much of the specimen design and background information for this research is based on the ACI 440.1R-06. This publication has been derived from international sources of experimental, analytical, and field observation studies. According to this publication, despite several successful applications of FRP reinforcement, there is still great demand for continued research to improve the performance of FRP reinforcement for factors such as fire resistance, durability, bond fatigue, and bond splicing (2006).

2.1.3 Economic and Environmental Effects

Much attention is focused on FRP as a reinforcement alternative, due to the existing state of the US economy in combination with an aged infrastructure with many facilities nearing the end of their design lifespans. A study initiated by the National Association for Corrosion Engineers (NACE) and released by the Federal Highway Administration (FHWA) indicated that of the 583,000 bridges in the US, about 35,250 have been deemed structurally deficient due to corrosion of steel reinforcement. The rehabilitation and future maintenance of these deficient bridges is estimated to cost up to $8.3 billion dollars in the next 10 years. This value can be increase by a multiple of 10 to account for indirect costs to people and industries affected by these actions (Koch et al., 2001). These estimates serve as a good indicator of the importance for a solution to concrete reinforcement corrosion. A reliable non-corrosive alternative could greatly reduce these costs for the future.

Katz (2004) performed an environmental impact evaluation of the use of FRP reinforcing bars as a direct replacement for steel rebar. This study included a “cradle to grave” analysis of similarly designed bridge decks considering the erection, maintenance, and disposal periods of the structures lifetime. The maintenance stage showed the most significant difference of 36% in the point system of the Eco Indicator 99 lifecycle impact assessment tool. This point spread can be owed to the nearly non-existent amount of

maintenance required by the FRP reinforced deck. The resulting data from the Eco-indicator 99 analysis concluded that an environmental load reduction of approximately 50% could be achieved through the use of FRP reinforcement rather than conventional steel rebar.

2.2 Conventional FRP Concrete Reinforcement

Literature published regarding the structural performance of conventional GFRP bars was examined in order to develop a background on the benefits and faults of the currently commercially available material. This information is used to address the inherent issues of GFRP reinforcement. The different factors of reinforced concrete structural behavior have been categorized and described in the following sub-sections.

2.2.1 Bond

ACI 440.1R-06 (2006) states that bond force is primarily transferred by the following factors:

- Adhesion resistance (chemical bond)
- Friction resistance
- Mechanical interlock (interface irregularities)

While adhesion and friction resistance are expected to have negligible change with the use of the proposed reinforcements, the mechanical interlock function is expected to be improved greatly. Unlike the mechanical bond that is achieved by surface deformities in straight FRP bars, the interlocking action will be achieved through the integration of the reinforcement geometry as described in section 1.2.3 of this thesis.

Studies of bond performance of FRP internal reinforcement have been an area of demand for future research in FRP concrete reinforcements (ACI Committee 440, 2006; Porter & Harries, 2007). Studies conducted by Okelo and Yuan (2005) indicated that bar diameter, spacing, and embedment all have large influences on reinforcement bonding as well as bar deformation geometry. Standardizing the deformation contribution of bond effects presents a challenge since there is no current publication stating manufacturing standards (such as ASTM A 616/A applies for steel reinforcement). Several techniques for bar geometry deformation are currently used which include sand-coating, surface texturing, helical wraps,

grooving, and resin deformation. Each of these forms of geometry deformation exhibit different mechanical properties, making standardization of performance prediction difficult.

While evaluating the bond strength guidelines published in ACI 440.1R-06, Harajli and Abouniaj (2010) compared the bond performance and behavior of both ribbed and fiber wrapped GFRP reinforcing bars with spliced and pullout specimen configurations. Their observations concluded that bond strength is largely dependent on the mechanical actions controlled by surface deformations since the ribbed reinforcement exhibited more splitting failures in the concrete matrix rather than pullout debonding. It was also stated that regardless of the reinforcement type, the GFRP bond strength was observed to be two to three times lower than steel reinforcement. This work indicates that capitalizing on the mechanical action of the concept reinforcement bond strength can greatly be increased.

2.2.2 Deflection

The serviceability design recommendations of ACI 440.1R-06 (2006) indicate that FRP reinforced beams are by nature less stiff than steel reinforced beams. The following traits of FRP reinforcement are the cause of this reduced stiffness in FRP reinforced concrete beams:

- Relatively lower modulus of elasticity than steel
- Brittle-elastic nature
- Bond characteristics

As a result of this decreased stiffness, ACI 440 states that serviceability deflection criteria typically control the design.

The ACI 440.1R-06 refers to the ACI 318 “Building Code Requirements for Structural Concrete” (2011) for controlling deflections. Two design methods are provided in this code for one-way flexural members; the direct method of limiting computed deflections and the indirect method of limiting member thickness. The direct method is required to be used by the ACI 440.1R-06 due to the different material properties of steel reinforcement for which the ACI 318 minimum thickness requirements are based on.

Traditional methods for calculating deflection involve the use of the effective moment of inertia (I_e), however, it was proposed by studies from Bishoff and Gross (2011) that this over-predicts the true deflection values. Empirical factors are applied to the traditional deflection calculations, as prescribed by ACI 440.1R-06. However, the application of these factors is limited to rectangular sections of specific

elastic modulus to design strength ratio (E_f/f_{fu}) ranges. Bishoff and Gross have proposed the use of the following more widely accurate equation for determining the effective moment of inertia:

$$I_e = \frac{I_{cr}}{\left[1-\eta\left(\frac{M_{cr}}{M_a}\right)^2\right]} \leq I_g \qquad \textit{where: } \eta = 1 - \frac{I_{cr}}{I_g} \qquad \textit{[2.1]}$$

2.2.3 Flexure

The flexural design guidelines stated in ACI 440.1R-06 (2006) specify that the flexural capacity is dependent on the selection of the two modes of failure; concrete crushing or FRP rupture. Since FRP rupture is often sudden and catastrophic, this decision allows for the marginally more progressive option of concrete crushing failure to serve as a harbinger to collapse.

The failure mode is controlled with the reinforcement ratio parameter. The concrete crushing mode is achieved by setting the reinforcement ratio to be greater than the balanced reinforcement ratio ($\rho_f > \rho_{fb}$). The contrary of this is used for FRP rupture ($\rho_f < \rho_{fb}$). The following equation is used to obtain the balanced reinforcement ratio:

$$\rho_{fb} = 0.85\beta_1 \frac{f_c'}{f_{fu}} \frac{E_f \varepsilon_{cu}}{E_f \varepsilon_{cu} + f_{fu}} \qquad \textit{[2.2]}$$

The effect of this controlling parameter was validated by Kassem, et al. (2011) with their experimental evaluation of twenty-four full-scale concrete beams reinforced with either carbon, glass, or aramid FRP bars. In each specimen, the concrete crushing failure mode ($\rho_f > \rho_{fb}$) was designed for the beam, and all beams failed accordingly. In the interest of observing the tensile capacity of the proposed reinforcement systems, the FRP rupture mode is used for the design of the experiment specimens.

2.2.4 Shear

ACI440.1R-06 (2006) specifies that the shear contribution of FRP reinforcing bars is comparatively worse than that of steel reinforced members due to the low stiffness of the FRP flexural reinforcement. The effect of the low stiffness in the flexural reinforcement leads to a reduced depth to the neutral axis, ultimately reducing the compressive zone found in the member cross-section and increasing the shear crack width. This results in a reduction in shear contribution from the compressive zone and aggregate interlock. This aspect of shear strength is addressed with the constrictive action described in section 1.2.1 where aggregate interlocking and compressive stresses are recovered.

A study conducted by Maitra, et al. (2010) investigated load transfer of aggregate interlocking in unreinforced concrete pavement. The work confirmed that load transfer is dependent on not only aggregate geometry, nature of the fractured surface, and fracture area; but also joint opening and load magnitude. The opening and load characteristics are proposed to be controlled by the constriction aspect of the proposed reinforcements. By inducing compressive forces, crack openings in the effective region of the reinforcement presumably close increasing the normal interaction forces of the crack interface. It is assumed that this will heighten the effect of aggregate interlock for shear.

Direct shear strength contribution of the flexural reinforcement through the dowel action of the FRP bars is also postulated to be worse than that of steel due to weak the interlaminar shear strength of FRP (ACI Committee 440, 2006). Interlaminar shear strength is low in FRP because of the uniaxial nature of the fibers. FRP does not typically include fibers which transcend the layers that are bonded by the relatively weak epoxy matrix. However, it is also stated in ACI 440.1R-06 that off-axis orientation of fibers increases the shear resistance of the reinforcement, varying with the degree of offset. Off-axis fibers that can contribute to shear strength are found in both of the concept reinforcement designs as described in section 1.2.2.

2.3 Alternative FRP Reinforcements

Hybrid reinforcement systems (HRS) have become a popular alternative reinforcement concept that utilizes the advantages of FRP materials. They are often pursued due to their potential for achieving simulated ductility through progressive failure. There have been multiple approaches to designs of HRS rebar that involve variations in fiber orientation and material.

As an alternative to the linear failure behavior and poor bond strength typically observed in FRP rebar, Harris, et al. (1998) studied the performance FRP rebar that is created by strategically braiding yarns of various fiber materials before embedding the braid in a polymer matrix via a pultrusion process. This HRS rebar exhibited a bi-linear stress-strain behavior by inducing progressive failure in a two-step process. This type of behavior simulates ductility, allowing for a limit-state design approach that would otherwise not be possible with conventional straight-fiber FRP rebar. Bond strength of the braided rods also shows improvement over conventional FRP reinforcement since the braiding naturally provides a

textured surface to the rebar. While this solution addresses several inherent issues of FRP reinforcement, it would not be a viable alternative for most transportation structures since this method requires high modulus materials in order to function as equivalent to steel reinforcement. Aramid and carbon reinforcement strands were used for the braided fibers, which have a relative cost of approximately 15-20 and 8-60 times the price of e-glass fibers, respectively (Mazumdar, 2002). The use of these high modulus fiber materials with their inherent cost mean these braided reinforcements would not be viable for general use in transportation infrastructure.

In an attempt to produce a ductile composite reinforcement, Etman (2011) also investigated a HRS reinforcement, but with distinct differences from Harris's studies. Etman explored the use of unidirectional composite rods composed of a solid steel or aluminum core, surrounded by one or two layers of glass, carbon, or a combination of the two fibers. This study was able to achieve ductility with these HRS rebar, but combinations of carbon fibers and an aluminum core prove to be less efficient than conventional steel. This was determined to be an insufficient solution for use in general transportation structures because these rebars still contain a metallic core, and thus the potential for corrosion of the steel or alkaline damage of the aluminum is still present. The materials proposed for this arrangement are also more costly than steel or pure GFRP reinforcement.

2.4 Braided Composite Mechanics

Studies in braided composites were reviewed for their mechanically similar behavior to the proposed reinforcements. An article produced by Harte and Fleck (2000) investigated the mechanical properties of several coupon samples of braided composite tubes under tensile forces. These tubes were composed of braided GFRP at varying helix angles in order to compare the effect that the braid helix angle had on the failure mechanics of the samples. It was found that the helix angle was the primary influential parameter in the behavior of these composites, and that with a smaller helix angle the strain measure in the axial direction of the tube decreased when put into tension. This indicated that in order to avoid excessive deflection of the reinforcement units, smaller helix angles are more likely to produce stiffer reinforcement reactions.

Also found in the Harte and Fleck studies was a critical initial helix angle of $\theta < 45°$ that was identified to be the range at which the tube deformation maintained diameter-reducing (constrictive) properties when put into tension. This was determined with an analytical outline of the braided composite mechanics using the following equations defining the transverse strain between strands (e_t) with respect to the initial helix angle (θ_0) and the deformed helix angle (θ):

$$e_t = ln\left(\frac{sin\,2\theta}{sin\,2\theta_0}\right) \qquad [2.3]$$

This analysis indicates that the prototype design of the concept reinforcement must maintain a helix angle of $(\theta < 45°)$.

A similar study by Ayranci and Carey (2010) investigated the effects of radius of curvature to the analysis of elastic behavior of braided composites. It compared numerical analysis results providing longitudinal elastic modulus of flat unit cell (assumed in the Harte and Fleck studies) and curved unit cells of various curvatures. The results of which were validated with the use of experimental data of braided aramid FRP specimens. The results of these observations concluded that the curvature does affect the longitudinal elastic modulus of the composite greatly. The observed difference in longitudinal elastic modulus between a braided tube of a similar radius of curvature as the concept reinforcement (30 mm (1.2 in)) and a flat braided section was reported to be about 1.54%. The accuracy of which this occurs is not relevant to this research. However, the analytical results of the helix angle effects were in good agreement with the Harte and Fleck findings.

2.5 Concrete Particle/Aggregate Behavior

The shear strength of reinforced concrete increases after initial cracking due to particle and aggregate interaction. Ahmed et al. (2010) showed that shear strength supplied by stirrups is provided not only by the direct axial tension at the point intersection of crack faces and stirrups, but also by the confinement effects caused by the stirrups. This confinement maintains smaller shear cracking allowing for greater aggregate interaction between the crack faces. The confining effect will also be present in the compression zones of both helical and wave reinforcement assemblies, regardless of the presence of stirrups.

Chapter 3

Methods

This chapter discusses the processes used in the experimental evaluation of the novel FRP reinforcements. An explanation of key decisions methodology and data acquisition techniques are provided below.

3.1 Collecting Material Properties

Material properties of the different components of the experimental test specimens were required in order to perform an accurate design of the beam specimens. Small representative samples of the GFRP and concrete components were independently created and tested in order to determine the material properties of these elements representative of the materials as they were fabricated in the lab.

3.1.1 GFRP Material Properties

Fabrication methodologies have a significant effect on the way that a composite material ultimately performs. Physical properties such as fiber volume fraction and selection of matrix material are often governed by the fabrication of the FRP material. Therefore a uniform fabrication method was used in all components of this study in order to maintain consistency in material quality. This allows for more direct comparative analysis.

There are several commonly used methods for manufacturing FRP components. Typically commercially manufactured FRP rebar is produced using the pultrusion fabrication method. For this process, yarns of glass fibers are drawn through a thermoset resin bath and then immediately through a heated die which simultaneously shapes the composite materials and cures the resin. While pultrusion is very practical for high-volume continuous cross-section items; its limitations in geometric complexity and requirements for specialized machinery make it an impractical method for the reinforcement prototypes presented in this study (Mazumdar, 2002).

The filament winding process is ideal for producing tubular composites much like the helical reinforcement in this study. This process involves emitting a resin impregnated fiber yarn from a moving

dispenser onto a rotating cylindrical mandrel. However, the use of this process is impractical for this study due to the low-volume of units required, high initial capital needed for the specialty equipment required, and the incompatibility of this process with other reinforcement designs (Mazumdar, 2002).

The highly customizable production and low capital costs associated with the hand lay-up method, wherein yarns of glass fiber are coated with an epoxy resin and placed by hand onto a form, made it the technique of choice for this study. This allows for the practical production of a relatively low quantity of FRP units to be created. The flexibility of this method allows for all FRP units to be fabricated in a similar manner, which yields consistent material.

The glass fiber component of the GFRP composite is Owens Corning ME 3021, a unidirectional continuous fiber composed of Owens Corning Advantex fibers, which exhibit improved acid resistance over traditional E-glass fibers. The manufacturer supplied material properties of these fibers embedded in general purpose polyester resin with a 35.5% class fiber content are listed in Table 1. This material was chosen due its suitability for general GFRP applications, low cost, and versatility.

Table 1: Owens Corning ME3021 roving composite specifications

Property [Test method]	**Dry Range [MPa (psi)]**	**Wet Range [MPa (psi)]**
Tensile Strength [ASTM D 638]	59 - 98 (8,500 - 14,000)	58-94 (8,500 – 14,000)
Tensile Modulus [ASTM D 638]	7,542 - 14,893 (1,094,000 - 2,160,000)	5,626-11,562 (816,000 - 1,677,000)
Flexural Strength [ASTM D 790]	166 – 307 (24,000 – 44,500)	132-259 (9,280 – 37,600)
Flexural Modulus [ASTM D 790]	6,939 – 12,065 (1,006,000 – 1,750,000)	6,053 – 13,217 (878,000 – 1,917,000)

The polymer matrix selected for the GFRP composite is a general purpose epoxy resin manufactured by System Three. It is a two-part (epoxy resin and hardener) system that yields a medium-modulus hardened epoxy. The cured material properties of this resin are shown in Table 2.

Table 2: System Three Multi-purpose Epoxy Resin Cured Properties

Property [Test source]	Property Value
Tensile Strength [ASTM D638]	51.71 MPa (7,500 psi)
Tensile Elongation [ASTM D638]	11%
Tensile Modulus [ASTM D638]	2,240.80 MPa (325,000 psi)
Flexural Strength [ASTM D790]	86.184 MPa (12,500 psi)
Flexural Modulus [ASTM D790]	(350,000)
Heat Deflection Temperature	119°F
Compressive Yield Strength [ASTM D695]	(12,000 psi)
Compressive Ultimate Strength [ASTM D695]	(12,500 psi)

A series of five sample GFRP rods were fabricated using the standard hand-layup method. The yarns were cast into a straight channel, as described in detail in section 3.3.1.

The sample specimens were tested in tension according to the ASTM D7205 Standard Test Method for Tensile Properties of Fiber Reinforced Polymer Matrix Composite Bars (2012). The coupons were loaded into a United SFM-300KN testing machine shown in Figure 6 where the applied loading was measured by an internal load cell, and strain was measured with an extensometer. The results of these tests are shown in Table 3.

Figure 6: GFRP sample specimen in testing machine

Table 3: Sample GFRP Rod Test Data

Sample ID	Width [mm (in)]	Height [mm (in)]	Area [mm^2 (in^2)]	Ultimate Tensile Force [kN (lb)]	Ultimate Tensile Stress [MPa (ksi)]	Young's Modulus [MPa (ksi)]
S11	3.96 (0.156)	5.11 (0.201)	20.3 (0.0314)	9.68 (2,180)	309 (69.4)	34,400 (4,990)
S12	2.87 (0.113)	5.03 (0.198)	14.5 (0.0224)	7.98 (1,790)	357 (80.1)	35,200 (5,110)
S13	3.61 (0.142)	4.88 (0.192)	17.6 (0.0273)	7.97 (1,790)	292 (65.7)	50,900 (7,390)
S14	3.51 (0.138)	4.95 (0.195)	17.4 (0.0269)	7.94 (1,790)	295 (66.3)	36,000 (5,220)
S15	3.56 (0.140)	5.21 (0.205)	18.5 (0.0287)	9.25 (2,080)	332 (72.5)	41,200 (5,970)
Average	3.51 (0.138)	5.05 (0.199)	17.7 (0.0274)	8.72 (1,960)	320 (71.9)	40,400 (5,860)

3.1.2 Concrete

The model beam specimens are designed to simulate general structural performance that could be expected in a typical GFRP reinforced bridge component using commercially available GFRP reinforcing rods. Therefore, concrete properties that would typically be required for transportation structures were selected from the AASHTO LRFD Bridge Design Specifications (2006). The specifications require the use of Class A general structural use normal weight concrete. The required properties of this concrete are listed in Table 4 below.

Table 4: AASHTO Class A Concrete Specifications

Minimum Cement Content	277 kg/yd^3 (611 lb/yd^3)
Maximum W/C Ratio (by weight)	0.49
Air Content Range [%]	6.0±1.5%
Coarse Aggregate	25.4 mm (1.00 in) - No. 4 sieve
28-Day Compressive Strength	27.6 MPa (4 ksi)

Due to the low volume of concrete required for the model specimens (making a redi-mix truck delivery impractical), the premixed Quikrete Mix #1101 was selected. Using the manufacturer's provided properties to approximate water/mix (w/m) ratios; three sets of concrete sample test cylinders were cast at varying strengths. These sample cylinders were tested, according to the ASTM C39 Standard Test Method for Compressive Strength of Cylindrical Concrete Specimens, in order to determine an

appropriate w/m for the desired concrete ultimate strength (f_c') of 27.58 MPa (4,000 psi). The results from the tests are displayed in Table 5 below.

Table 5: Quickrete Mix #1101 test cylinder data

Cylinder ID	w/m	Target Strength [MPa (psi)]	Actual Strength [MPa (psi)]
1.1	0.0937	27.58 (4,000)	ERROR[1]
1.2			35.01 (5,078)
1.3			38.89 (5,641)
1.4			37.07 (5,377)
2.1	0.103	24.13 (3,500)	29.45 (4,271)
2.2			29.34 (4,255)
2.3			29.42 (4,267)
2.4			32.02 (4,644)
3.1	0.112	20.68 (3,000)	19.03 (2,760)
3.2			20.00 (2,901)
3.3			20.00 (2,901)
3.4			19.28 (2,796)

The values produced by this test are used to derive equation [3.1] for the w/m ratio as a function of desired strength. For concrete with an ultimate strength of 27.58 MPa (4,000 psi), equation [3.1] results in a w/m ratio of 0.1025. This ratio is used for the casting of the specimen beams.

$$\left(\frac{w}{m}\right) = -0.00003 f_c'[MPa]^2 + 0.0004 f_c'[MPa] + 0.1143 \qquad [3.1]$$

3.2 Specimen Design

The concept reinforcement systems presented in this study are being evaluated for their potential as corrosion-free alternatives to steel bar reinforcements in transportation structures. This is the first evaluation of this novel concept, thus simple testing conditions are selected in order to obtain data on standard structural performance characteristics. A rectangular beam girder design was used as the specimen model prototype. Simple beam mechanics allows for reliable interpretation and analysis of the reinforcement system. Select dimensions of the prototype beam were maintained throughout this study to grant simplified comparative analysis procedures between each specimen. The dimensions of the

[1] Results for cylinder 1.1 discarded due to equipment error

prototype were then reduced to a 1:3 scale for laboratory testing to ease replication efforts and loading frame requirements. These dimensions are listed in Table 6.

Table 6: Specimen dimensions

Dimension	Prototype	Model
Beam length	4572 mm (15 ft)	1524 mm (5 ft)
Beam width	609.6 mm (24 in)	203.2 mm (8 in)
Clear cover	50.8 mm (2 in)	16.93 mm(0.6667 in)

3.2.1 Fiber Nomenclature

In order to clarify the difference between the specific components used in the GFRP components, the following descriptive nomenclature is used throughout this document.

- Strand – A single glass fiber unit.
- Yarn – A collection of glass strands that are wound on a spool by the manufacturer.
- Cord – A single GFRP component that makes up the unit assembly of the concept reinforcements.

3.2.2 Reinforcement

The beam specimens were designed with three unique flexural reinforcement types. Each flexural reinforcement type was included in two identical beams with shear reinforcement and two without. The combination of these reinforcement configurations created six unique beam reinforcement assemblies. Identical pairs of each of these beam specimens (twelve total) were created and tested.

The tensile design properties of the GFRP were taken as the average of the results from the sample coupon test listed in Table 3:

- Ultimate tensile stress (f_y): 320 MPa (71.9 ksi)
- Modulus of elasticity (E_f): 40,400 MPa (5,860 ksi)

Just as conventional steel reinforcement requires bar deformations to ensure adequate bond to the surrounding concrete, GFRP requires some form of mechanical resistance at its interface with concrete. Several techniques have been employed with commercially produced GFRP bars to achieve a

similar effect. Some of the more commonly found techniques in commercial FRP reinforcement are; sand-coating, surface texturing, helical wrapping, deep denting (grooving), and deformations in the resin. Sand-coating was selected for this study due to its compatibility with the hand lay-up fabrication method, and its ability to achieve adequate bond (Okelo & Yuan, 2005).

3.2.2.1 Flexural Reinforcement Design

The geometric parameters of the specimen flexural reinforcement were chosen to allow for examination of the following three major characteristics:

- **Kinematic action vs. Axial loading**

  The effect of the constrictive action of the proposed reinforcement is compared with the direct axial force transfer mode of traditional rebar. This is the primary investigation of this research.

- **Helical vs. Wave**

  Two different geometries are tested to achieve the desired constrictive action. Both helical and wave forms naturally tend to straighten when put in tension, which is the desired mechanical reaction. The effectiveness of one shape over the other is compared.

- **High vs. Low wavelength**

  Since there is no previous research on reinforcement geometries of this kind, little is known about the effects of geometric parameters. The wavelength of the waveform (or helix observed in two-dimensional geometry) appears to be the most influential parameter for the function of this reinforcement. The helical reinforcement is designed with high-wavelength geometry, and the wave is designed at low-wavelength in order to isolate the effects of the form. By choosing practical high and low values of the wavelength dimension, the approximate value of the wavelength with the highest tensile resistance while also providing good constrictive behavior is targeted. The dimensions of these parameters are shown in Table 7.

Table 7: Specimen reinforcement wave geometry

Reinforcement type	Cord Angle	Cord Wavelength
II	10°	905.1 mm (35.63 in)
III	45°	59.32 mm (2.335 in)

A complete detailed record of the design calculations and the reinforcement shop drawings can be found in Appendix A and Appendix B respectively. The general flexural reinforcement design configurations are categorized into the following three groups:

- ***Type I (Control)***

  Composed of a collection of twelve straight rods with a square cross-section.

  The bars are placed in three rows consisting of four bars. This configuration is shown in Figure 7. The horizontal spacing of the rebar is 914.57 mm^2 (1.4176 in^2), while the vertical clear spacing of the rows is 16.9 mm (0.667 in). This flexural reinforcement type will be applied to beams to be used as control specimens.

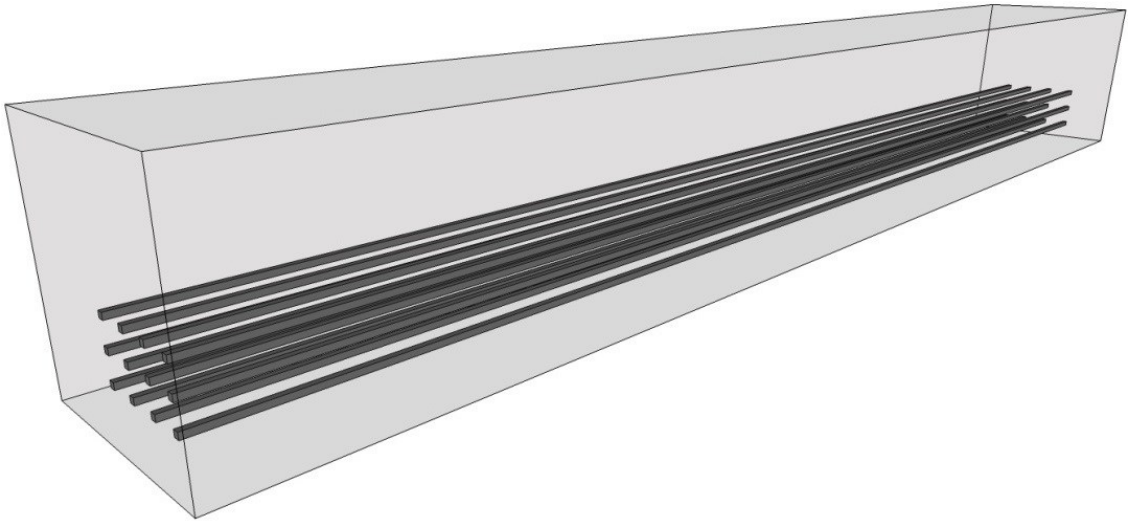

Figure 7: Type I flexural reinforcement

- ***Type II***

  Assemblies consisting of cords cast in an interlaced triple-helix configuration.

  Two of these assemblies will be placed at an even spacing in a row in the conventional location for flexural reinforcement.

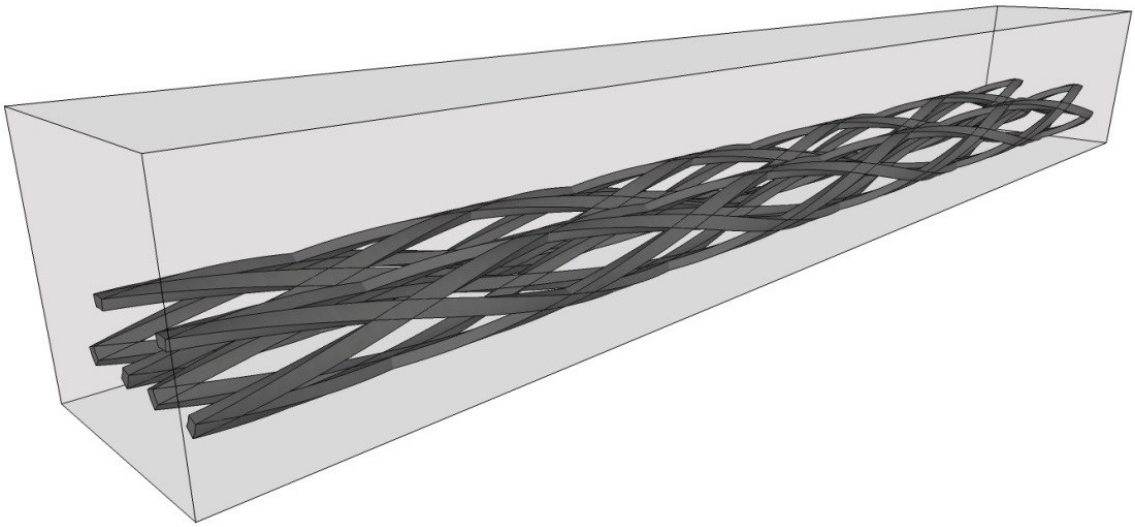

Figure 8: Type II flexural reinforcement

- ***Type III***

  A single mesh assembly consisting of twenty FRP cords formed in sinusoidal shapes that are bonded together. The cords are interlaced to form a mat configuration

  The mat will be placed flat in the tensile region of the beam.

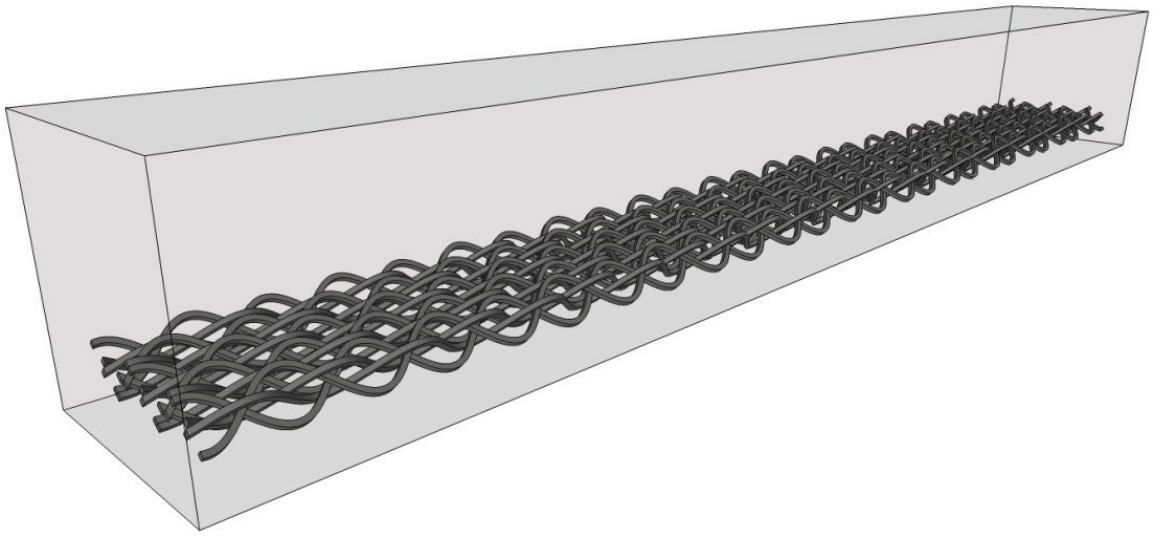

Figure 9: Type III flexural reinforcement

The cross-sectional dimensions were kept similar between all specimens to ease comparative analysis practices and reduce the skewing of results from size effects. The effective depth of the reinforcement (d) and cross-sectional area of the reinforcement (A_f) are specified in Table 8.

Table 8: Specimen reinforcement dimensions

Reinforcement Type	**Reinforcement Area** (A_f)	**Effective Depth** (d)
I	374.7 mm^2 (0.5808 in^2)	164.9 mm (6.493 in)
II	380.1 mm^2 (0.5892 in^2)	160.6 mm (6.323 in)
III	374.2 mm^2 (0.5800 in^2)	163.7 mm (6.444 in)

3.2.2.2 Shear Reinforcement Design

The notation and description of the two shear reinforcement varietals are as follows:

- ***Type a***

  Standard shear reinforcement as prescribed by the ACI 440.1R-06. This reinforcement is used to increase the shear strength of the beam so that it should fail in flexure only, providing an event that will present data on the performance of the flexural reinforcement being observed.

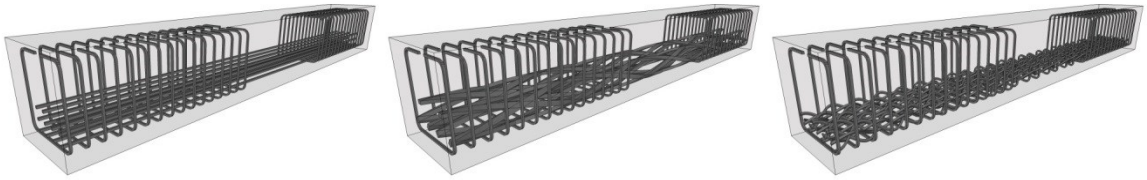

Figure 10: Beam specimens with shear reinforcement

- ***Type b***

  Shear reinforcement will be completely omitted from the beam specimen as seen in Figure 7-Figure 9 which allows the beam to fail in shear, enabling experimental determination of shear strength gain provided by the prototype flexural reinforcement.

3.2.3 Specimen ID Nomenclature

For the twelve beam specimens presented, the following identification system shown in Table 9 has been devised.

Table 9: Specimen nomenclature

Flexural reinforcement	Shear reinforcement	Replicate	Specimen ID
I	a	1	Ia-1
		2	Ia-2
	b	1	Ib-1
		2	Ib-2
II	a	1	IIa-1
		2	IIa-2
	b	1	IIb-1
		2	IIb-2
III	a	1	IIIa-1
		2	IIIa-2
	b	1	IIIb-1
		2	IIIb-2

Truncations of the specimen ID indicate all specimens within the nominal grouping. (i.e. type IIa indicates all type II flexural reinforce specimens with shear reinforcing)

3.3 Specimen Reinforcement Fabrication

While the general lay-up procedure remained uniform for each type of reinforcement, the processes by which lay-up forms were created and used varies. Logistical and geometric restrictions resulted in different requirements for each of the reinforcement types. Custom lay-up forms were created in the lab and were used in different ways.

The basic structure of all of the forms consisted of a silicone channel, supported by a rigid structure. Molds were created for casting the silicone channels using various techniques as required by the differing geometries and complexities of the required GFRP components. A two-part tin-catalyzed silicone was chosen as the form channel material. This allowed for cured GFRP units to easily be removed from the form, while also allowing for multiple uses of the lay-up forms.

3.3.1 GFRP Coupon Fabrication

The five GFRP coupons described in section 3.1.1 consisted of a 610 mm (24 in) straight section with two 152 mm (6 in) hooked regions at each end to promote a sufficient bond for anchorage to the testing machine load heads. The upper image in Figure 11 demonstrates the GFRP coupon without the anchorage components.

The hooked ends of sample coupons were cast into anchors made of steel pipe filled with an epoxy resin (see Figure 11). The steel anchors were equipped with a slotted plate on the coupon end to prevent bond failure between the pipe and the epoxy anchor. A nut was welded to the loading end to be attached to the loading machine.

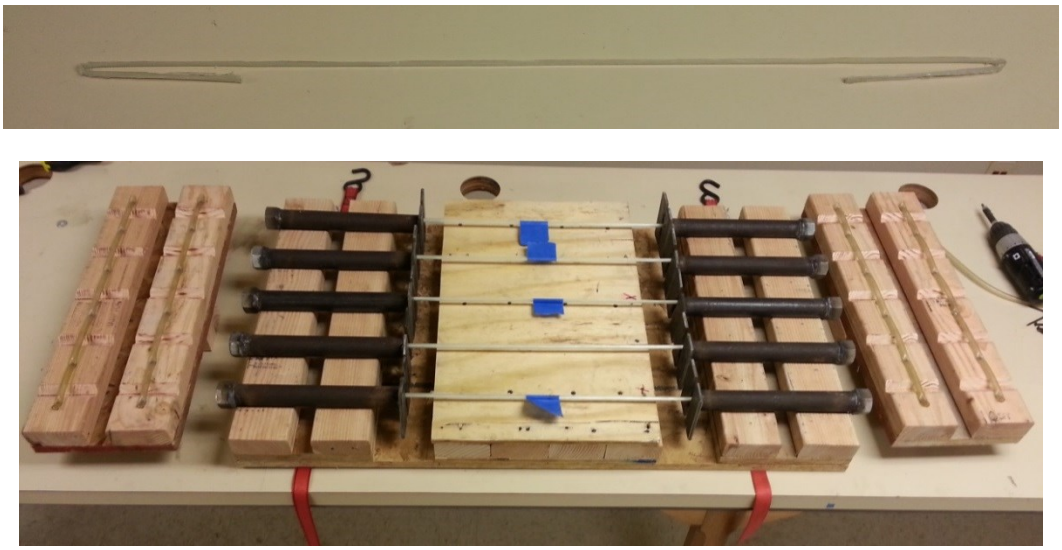

Figure 11: GFRP coupon fabrication - (top) w/o anchorage (bottom) anchorage casting frame

During the fabrication of the GFRP coupons, the number of yarns required to fill the lay-up form was exactly 10 yarns per coupon. This value was then divided by the cross-sectional area of the coupon to get a yard density value of 0.566 yarns/mm^2 (365 yarns/in^2) Using this approximate yarn concentration value with the component cord cross-sections, the number of yarns per cord were calculated as shown in Table 10.

Table 10: Glass fiber yarn count

GFRP Component	**Cord Area**	**Yarn Count per Cord**
Coupon	17.7 mm^2 (0.0274 in^2)	10
I	31.2 mm^2 (0.0484 in^2)	17
II	31.7 mm^2 (0.0491 in^2)	18
III	18.7 mm^2 (0.0290 in^2)	10
Stirrup	20.2 mm^2 (0.0313 in^2)	11

3.3.2 Type I Fabrication

The type I reinforcement required a straight channel for the GFRP layup procedure. The lay-up channel consisted of a prismatic square cross-section in a silicone medium, supported by a rigid acrylic frame (see Figure 12). The acrylic frame serves a dual purpose. The first function is as a channel from which the silicone form is cast. The second function serves as a straight rigid frame to support the silicone form while the GFRP lay-up is in progress.

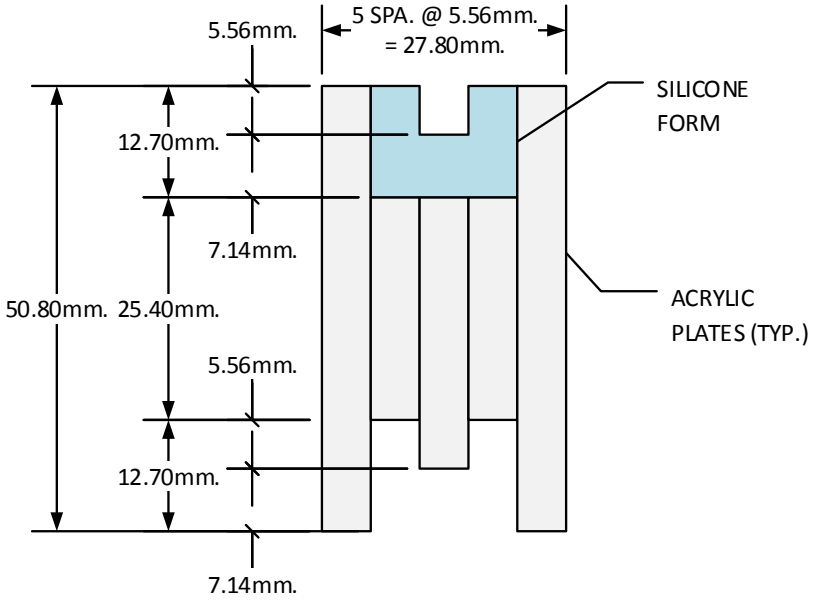

Figure 12: Type I lay-up jig cross-section

The type I reinforcement is fabricated in a 6-phase process in which several custom fabrication components were created and used. Figure 13 illustrates the phases of fabrication for each individual reinforcing rod produced. Arrows indicate the order in which the phases are executed.

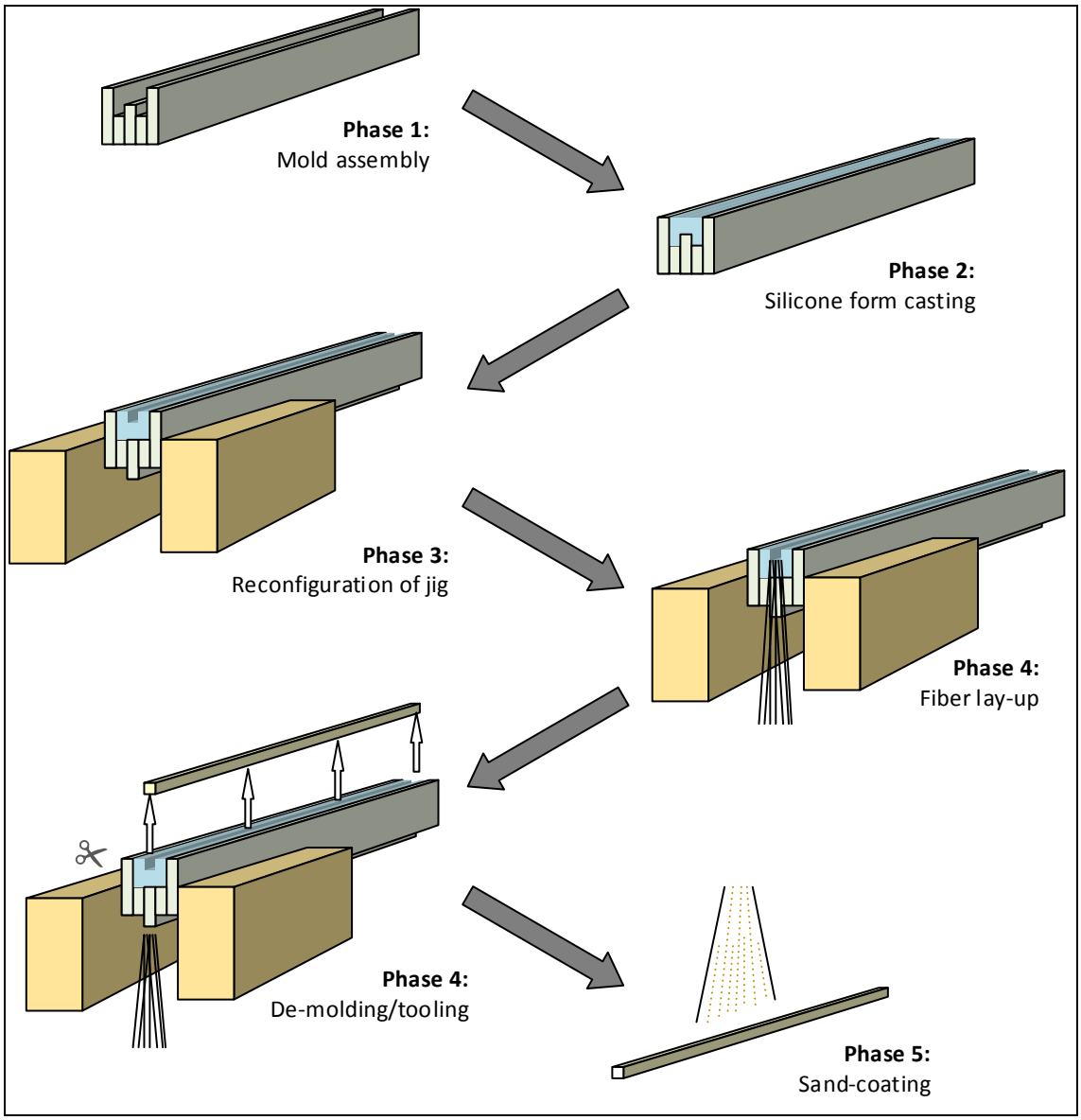

Figure 13: Type I fabrication process

3.3.2.1 Silicone Form

The silicone used for the lay-up form is cast into one side of the form molding side of the frame assembly. The silicone used is the GI-1110 produced by Silicones, Inc., which is specifically formulated for molding. It was chosen for its high flexibility and high chemical resistance, making the de-molding process of the GFRP forms reusable for several of the required castings.

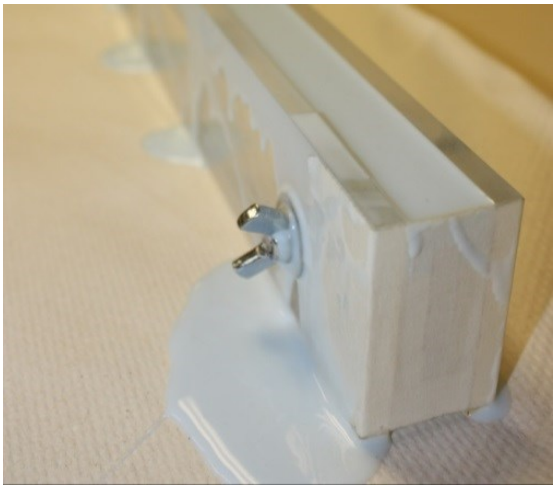

Figure 14: Silicone casting in type I mold

3.3.2.2 Lay-up Jig

After the silicone has fully cured, the acrylic plates which make up the mold were carefully disassembled and the silicone form is removed. The acrylic frame assembly is then reassembled, and the silicone form was fitted into the form support side. Additional support blocks are added to each end of the acrylic frame which provides stabilization and locations for fiber anchors.

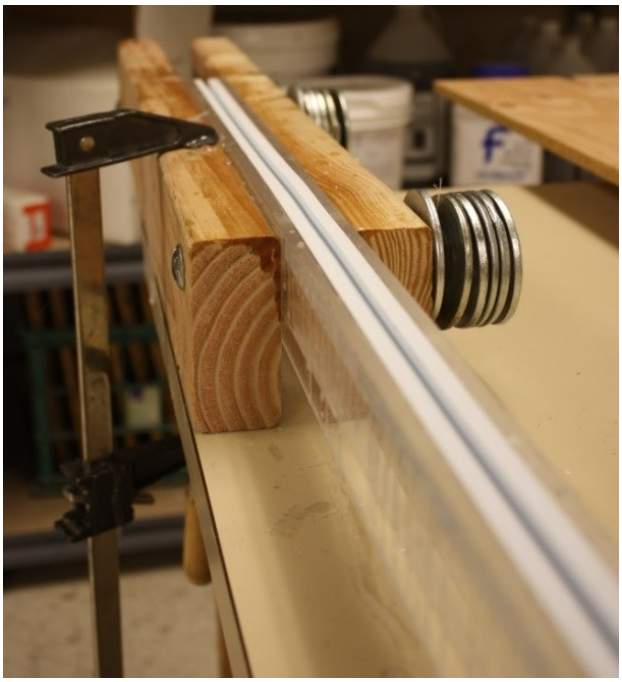

Figure 15: Type I lay-up jig

3.3.2.3 GFRP Lay-up

The lay-up process began with anchoring the first yarn (single unit of fiber grouping wound on a spool) of the ME 3021. The activated epoxy (epoxy/hardener mixture) was then applied as a thin coat onto the empty form in order to ensure full saturation at the fiber/form interface. The yarn was straightened to ensure all fibers in the grouping are aligned and no knotting has occurred. The yarn was then cut to length and a tensioning weight is attached to its free end in order to maintain slight tension in the fibers to keep them aligned during the lay-up process. The yarn was coated in the epoxy resin and placed into the form channel. The yarn was gently pressed into place with a brush to remove voids and promote fiber alignment. This process was repeated until seventeen yarns are saturated and placed.

3.3.2.4 De-mold/tooling

After curing, the GFRP was removed from the form. This begins with cutting the ends of the GFRP rod to remove the tensioning weights, and anchorage point. The silicone form containing the GFRP was then removed from the acrylic frame, and flexed to release the GFRP rod. The rod was then examined for flaws, and if deemed necessary, excess hardened epoxy was ground off. The inspected and cleaned rod was then trimmed to 1.4891 m (58.625 in) to comply with clear cover requirements for a 1.524 m (60.00 in) long beam.

3.3.3 Type II Fabrication

The type II GFRP reinforcement was cast in several large units, requiring two per beam. This process requires a cylindrical form onto which the GFRP composite can be cast, while allowing for a repeatable de-molding procedure. The diagram seen in Figure 16 outlines the multi-stage process that was used to fabricate this reinforcement.

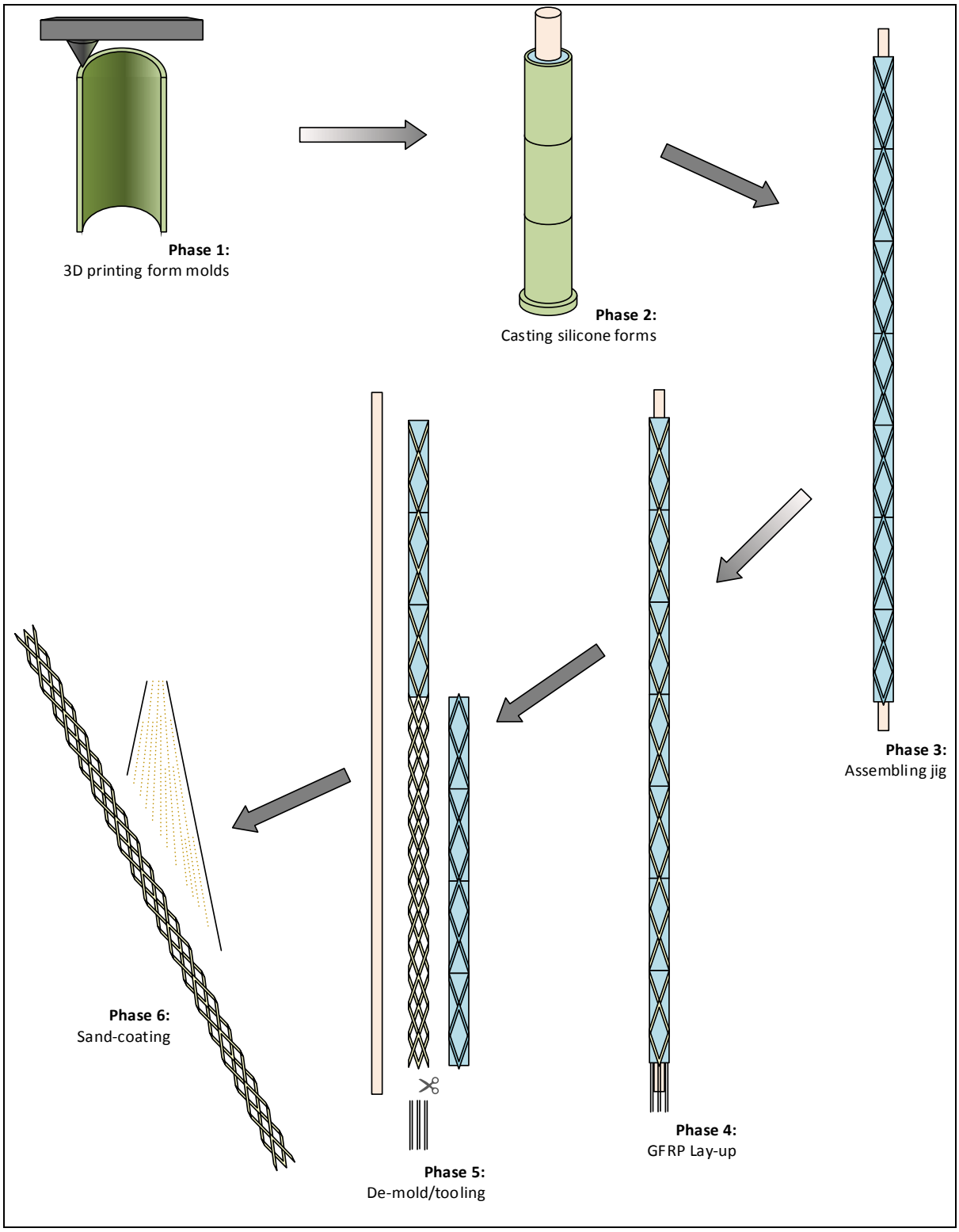

Figure 16: Type II fabrication process

3.3.3.1 Form Molds

Due to the complex geometric requirements for the type II forms, custom 3D printed molds were used to fabricate the silicone form components. The mold was printed with ABS plastic on an Afinia H840 3D printer shown in progress in Figure 17.

Figure 17: 3D printing in progress of type II form molds

Three dimensional shapes for these molds were designed in AutoCAD. The channels that the GFRP are cast into were achieved by the spiraling protrusions on the interior of the mold. The topography of the mold includes centering pegs to keep the inner post at an appropriate distance from the sides of the mold. Pegs and holes are also designed to insure alignment between mold sections. These various components are annotated in Figure 18.

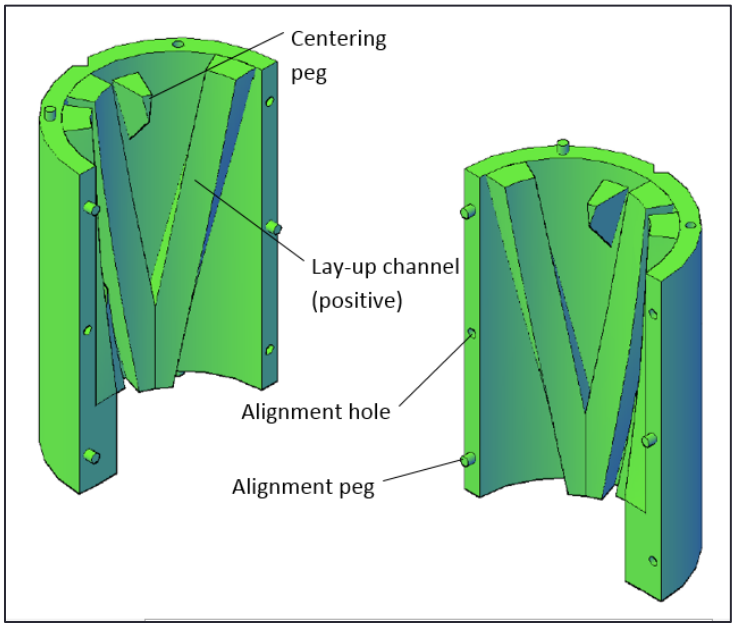

Figure 18: Rendering of the type II mold

The three dimensional drawing was exported into an stereolithography (.stl) file and imported into the proprietary Afinia software. The Afinia software then created a command code that was loaded onto the internal memory of the Afinia H840 printer, and the mold was printed.

The mold was created in three sections to allow for easier de-molding. The forms produced from this mold are a repeatable pattern that was duplicated to provide the silicone forms for the full length of the jig.

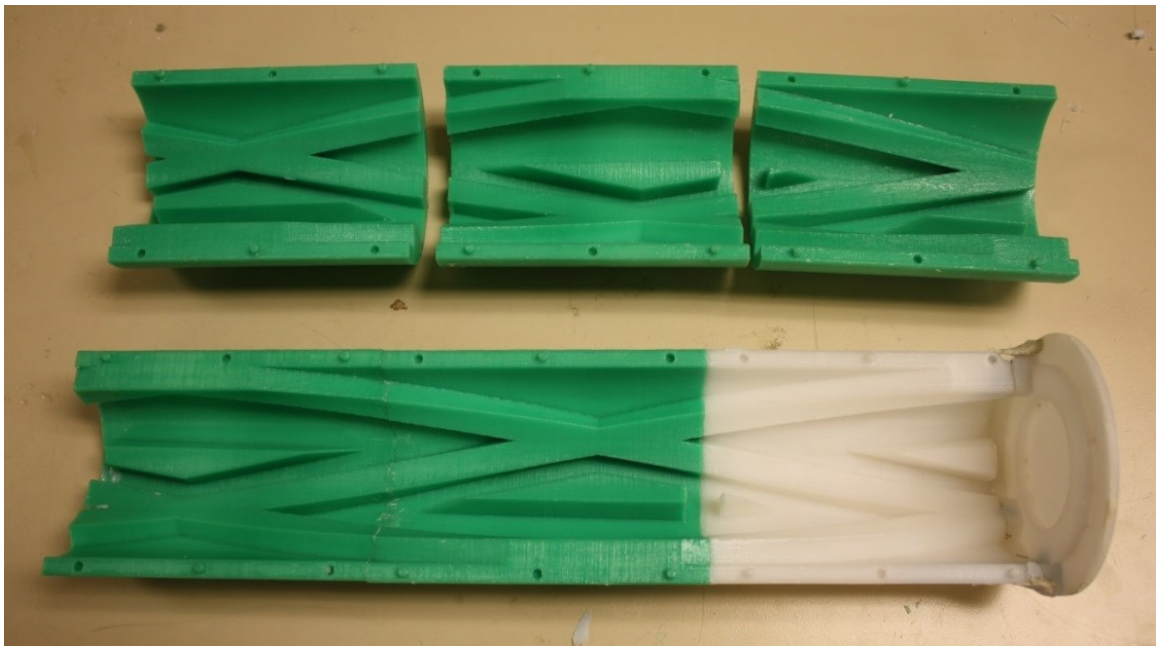

Figure 19: Type II assembled mold unit

3.3.3.2 Silicone Form

The mold was closed around the bottom of the support dowel and the same GI-1110 silicone that is used for the type I forms was poured into the open area between the mold and the dowel. Silicone was allowed to fill the bottom two sections of the mold completely, while the top section is only partially filled.

Figure 20: Type II silicone casting

Although three sections are used, the silicone that fills into the third section of the mold is trimmed away so that a cleanly cut edge can be achieved for proper alignment when the forms are placed in series on the dowel. Figure 21 shows a finished mold section that was replicated seven times in order to complete the type II jig.

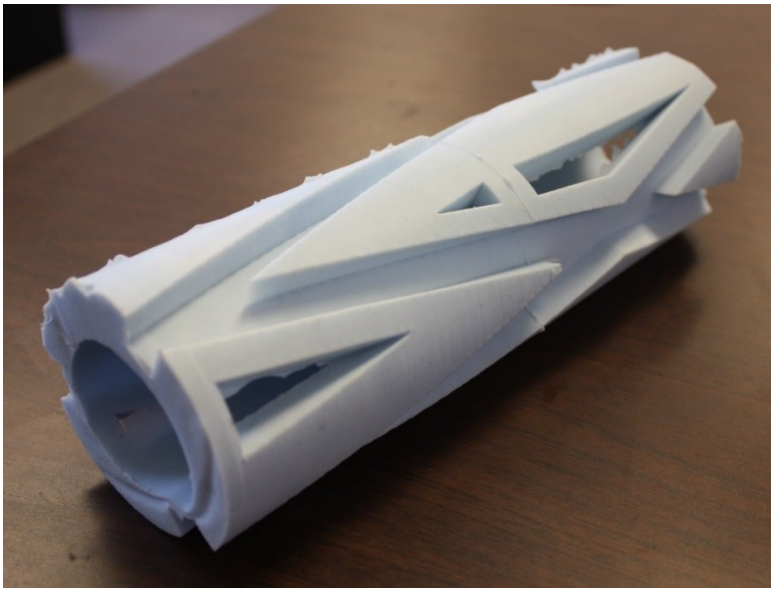

Figure 21: Type II silicone form mold

3.3.3.3 Jig

The form sections were placed in an alternating pattern as demonstrated in Figure 22. With the common ends matching, the groves in the forms are aligned to be continuous for the entire length of the jig.

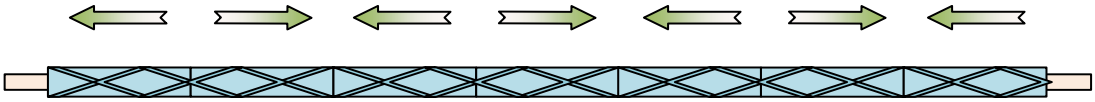

Figure 22: Type II form section configuration

A 3D printed end cap was created and attached to the support dowel at the bottom of the forms. This end cap served to keep the form sections in place, as well as to align the fiber yarns as they are wound through the jig. The jig is suspended from the ceiling for the lay-up process.

Figure 23: Type II lay-up jig

3.3.3.4 GFRP Lay-up

The procedures for the type II reinforcement were similar to that of the type I. A light coating of activated epoxy resin was first applied to the channels of the form. The ME 3021 was anchored at the end of the jig and thoroughly coated with the epoxy resin before being placed into the form channel. After a yarn had been placed into a channel, it was wound around an anchor point, saturated in epoxy, and passed through a new channel. This process was repeated until the yarn passes through each of the six

available channels. A tensioning weight was then fixed to the end of the fiber and suspended below the form. The yarn was then brushed down to remove voids and align fibers in each channel. A total of eighteen yarns were placed in this manner before the GFRP composite was left to cure.

3.3.3.5 De-molding/tooling

After the GFRP had cured, the superfluous fibers attached to anchor points and tensioning weights were then trimmed off. The interior supporting dowel was extracted from the silicone forms. This allows the silicone forms to be collapsed into the center of the GFRP component and removed.

Burs and excessive epoxy build-up were ground away from the GFRP. The type II unit was then trimmed to the same 1.4891 m (58.625 in) as the type I component.

3.3.4 Type III Fabrication

The type III reinforcement assemblies were configured in such a way that the entire reinforcement unit cannot be cast together in the manner that the type II was. The type III reinforcement is composed of a series of interlaced sinusoidal shaped cords of GFRP. This configuration required that one cord be cast at a time using the standard hand lay-up procedures on a collection of “half-wave” shaped silicone forms. These individual cords were manually interlaced and secured together to form the type III mat. The diagram in Figure 24 illustrates this process.

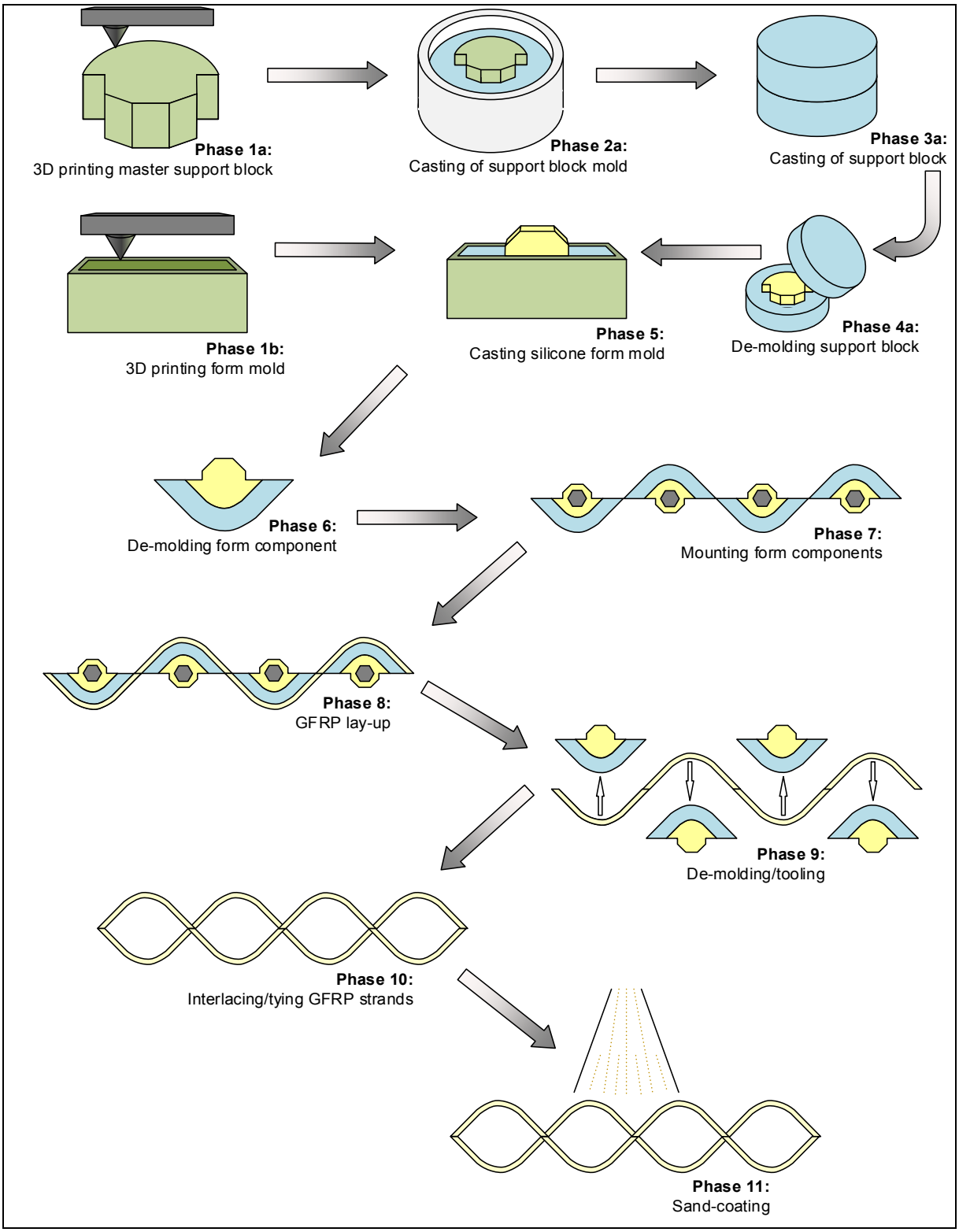

Figure 24: Type III fabrication process

3.3.4.1 Support Block and Form Mold

Similar to the type II form molds, the complex geometry of the type III reinforcement assemblies necessitated the use of custom 3D printed form molds. A rigid support block was required to support the flexible silicone form in the type III jig. In order for adequate functionality, the support block topography was required to have the following features:

- Form curvature – Curved surface at the interface of the silicone form to supply even support along the lay-up channel
- Fastener hole - A method of fixing the support block to a flat panel
- Silicone ties - Geometry that will maintain the attachment of the silicone form to the support block
- Alignment keys – Structures that correspond to shapes in the form mold

The entire type III jig required 130 of the silicone forms, so five molds were created using the master support block to facilitate mass replication. The support block mold was created from two separate silicone pieces that make up a two-part closed mold. Each part of the mold is cast individually with alignment keys, a filler gate, and a vent created during the castings. Figure 25 shows one of the finished support block molds.

The support block was then cast out of epoxy resin. The molds were closed and activated resin was poured into the filler gate. The casting was allowed to fully cure before the support block is de-molded and trimmed. Figure 25 shows the finished support block.

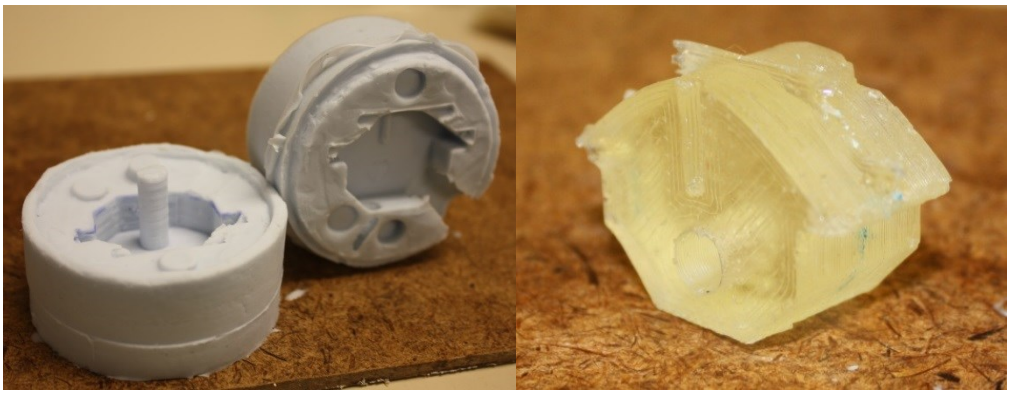

Figure 25: Type III (left) support block mold (right) support block

A mold was required for casting the silicone form onto the support blocks. This was also created with the use of 3D printing. The mold contains the corresponding key ridges to the notches found on the

support block. When in place, the support block was suspended above the bottom of the mold to allow space for the silicone form to be cast as demonstrated in Figure 26.

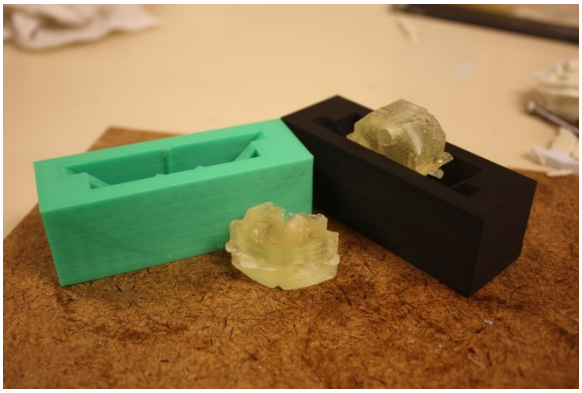

Figure 26: Type III form molds and support blocks

3.3.4.2 Silicone Form

The activated silicone mixture was cast into the form mold with the support block inserted into the mold. Excess silicone was then cast-off level with the top of the mold. After curing, the support blocks with their attached silicone forms are removed from the mold.

3.3.4.3 Mounting Form Components

The forms were fixed to a flat panel in an alternating pattern. The forms were laid out in five rows of twenty-six. Posts were also fixed to the panel to serve as an anchorage and diversion points for the required fiber yarn outside of the silicone forms. A diagram of this configuration is shown in Figure 27. Removable bolts were used as fasteners to allow for repeatable de-molding. Figure 28 shows a series of the mounted forms.

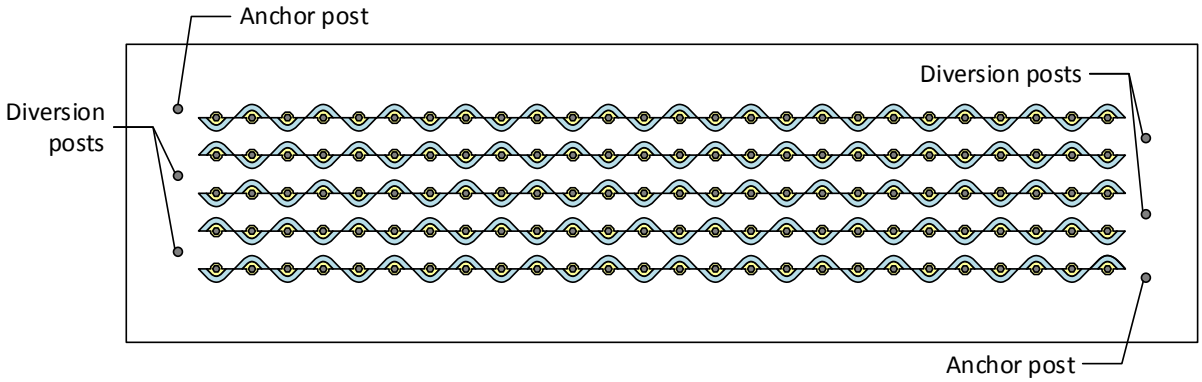

Figure 27: Type III form configuration diagram

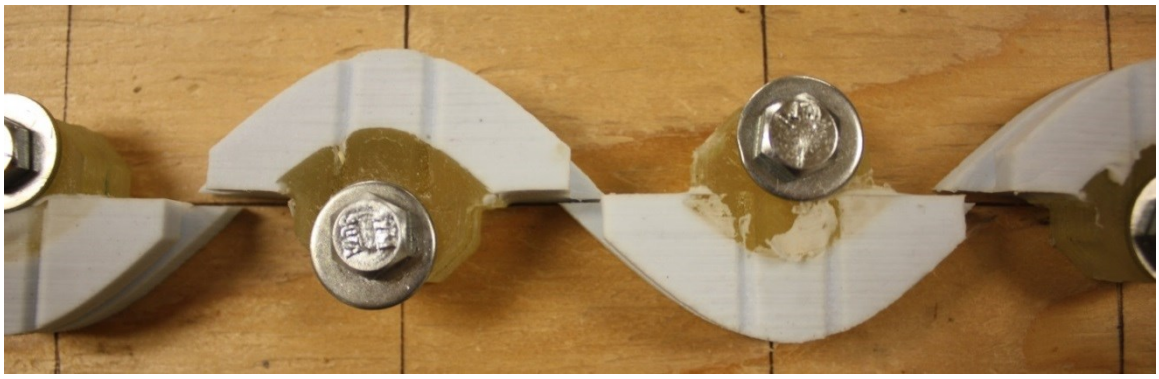

Figure 28: Type III form configuration

3.3.4.4 GFRP Lay-up

A thin coating of the activated epoxy mixture was applied to the casting surfaces of the forms before the fiber yarn is placed. Fiberglass yarns were fixed to an anchor point on the panel on one end of a row of forms. For each of the five rows, the yarn was individually coated with the epoxy and wound into each form notch. When transitioning to the next row of forms, the yarn was strung across the intermediate diversion post, and continued into the next row, as demonstrated in the yarn path diagram in Figure 29. After each the yarn has been cast into each row, a tensioning weight was suspended on the end for the yarn. After a tensioning weight was placed, the form was brushed over to remove voids and align the glass fibers. The process was repeated until a total of ten yarns occupied the jig.

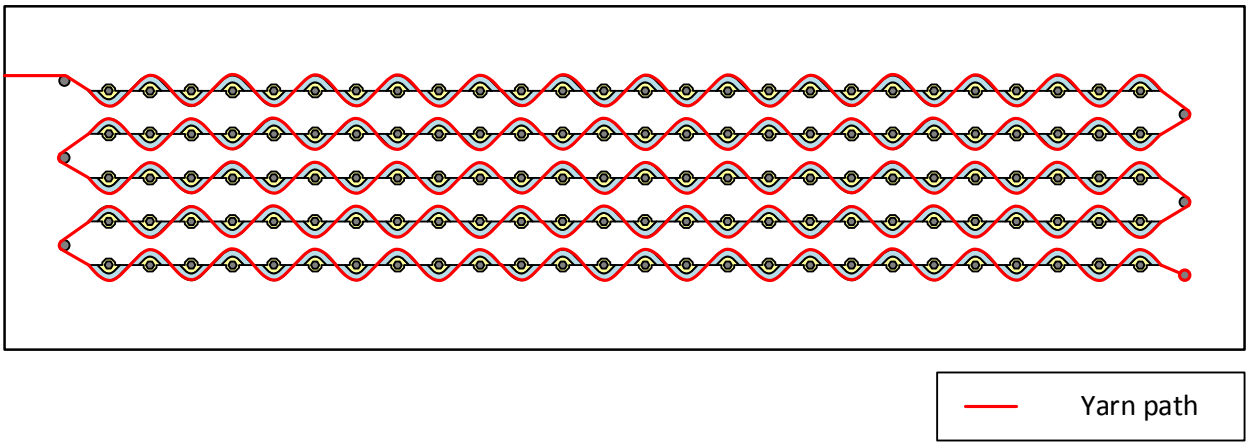

Figure 29: Type III yarn path jig diagram

3.3.4.5 De-molding/Tooling

After the GFRP cords were allowed to cure, they were removed from the lay-up jig. The superfluous fiber material that was attached to the tensioning weights and various posts were removed. Every other silicone form was then removed and the GFRP cords were pried from the remaining forms. The cords were then cut to length as done in the other reinforcement fabrication procedures. The cords were also inspected for major flaws and trimmed of excess cured epoxy.

3.3.4.6 Interlacing

After the individual type III GFRP cords were de-molded and tooled, the cords had to be assembled into a mat configuration. This process began with weaving the individual cords together into a 4-cord unit as shown in Figure 30. The 4-stran unit is configured so a pair of GFRP cords lies independently on a plane that perpendicularly intersects the plan of another pair of cords.

Figure 30: Assembly process of type III reinforcement

Five individual 4-cord units are then fixed together at the extremities of the units. The cross-sections represented in Figure 31 demonstrate the two different possible joining configurations that occur in an alternating pattern along the mat assembly.

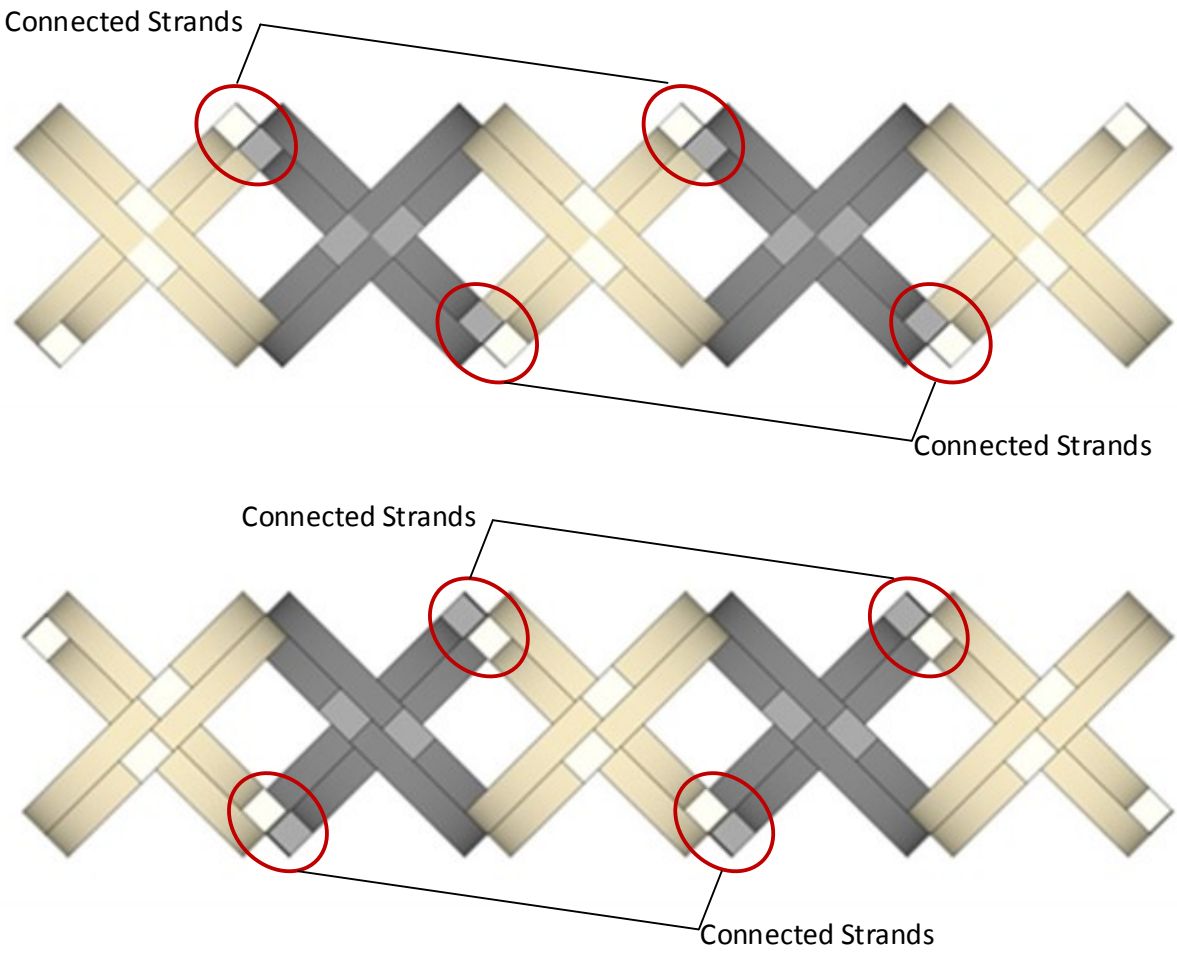

Figure 31: Type III mat assembly diagram

3.3.5 Stirrup Fabrication

For the stirrup fabrication, a multi-phase process was employed. This process involves the fabrication of silicone forms which were used in the assembly of a lay-up jig that has the capacity of casting five stirrups at a time. After the casting and curing process, the GFRP stirrups were sand-coated to promote adequate bond strength. The entire fabrication process is outlined in the diagram in Figure 32.

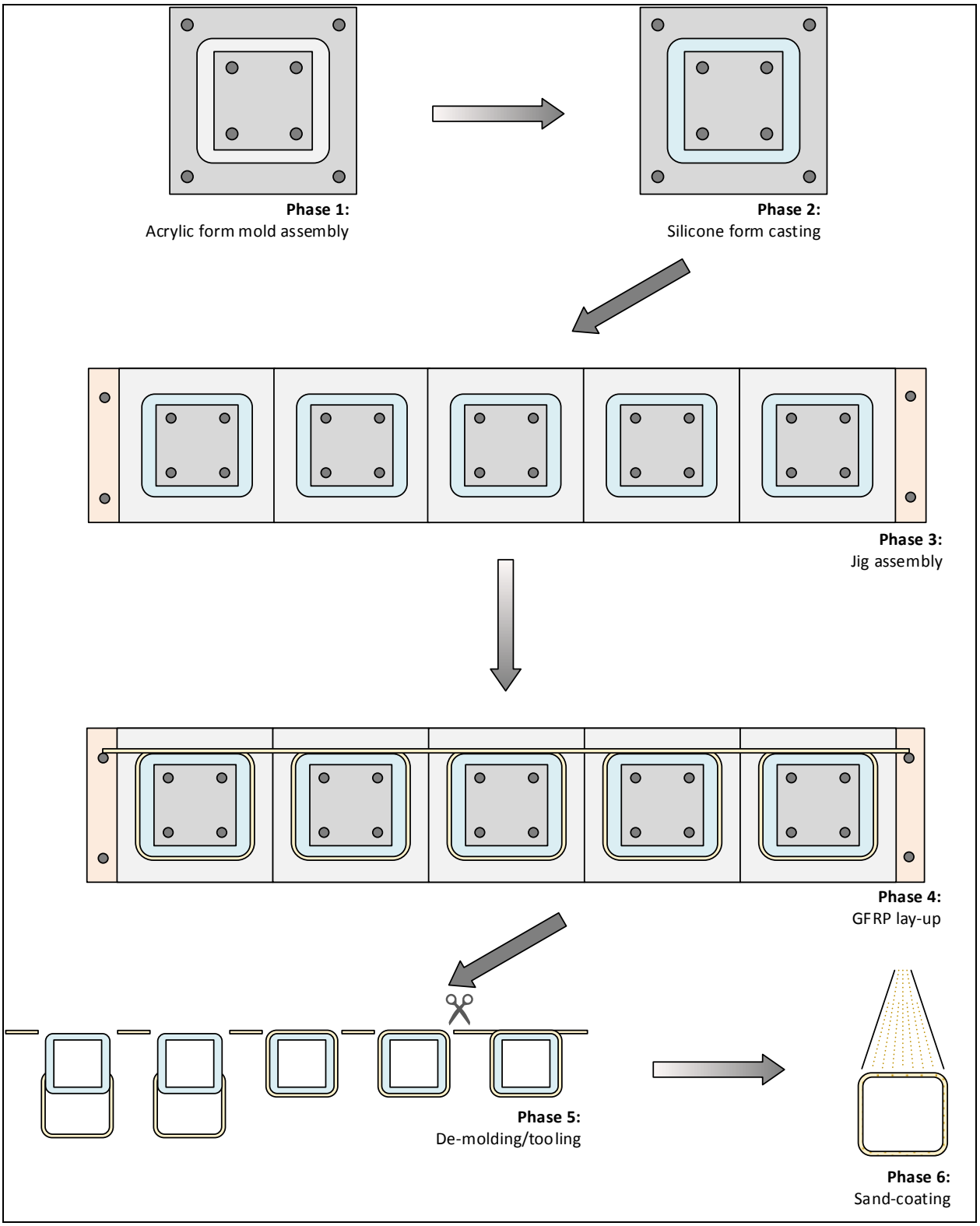

Figure 32: Stirrup fabrication procedures

3.3.5.1 Form mold

The stirrup form molds consist of four layers of 4.50 mm (0.117 in) thick acrylic plates that were bolted together. These plates include base, support, and mold ring components that are labeled in Figure 33.

The base plate provides a flat surface for the other plate components to be fastened to. The interior support plates act as a rigid structure for the silicone form to rest on and are not removed after the molding process. The outer mold ring plates give shape to the lay-up channel and are removed after the silicone is cast and cured. The shape of these acrylic plates were achieved by laser CNC cutting to create a cavity of the required geometry of the silicone form. Figure 34 shows the complete stacked configuration of the form mold.

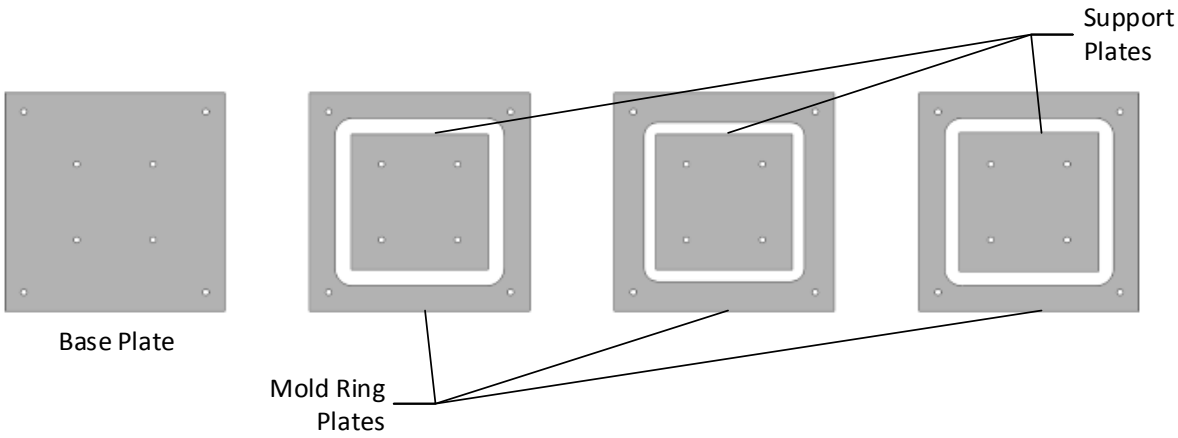

Figure 33: Separated layers of the stirrup form mold

Figure 34: Stirrup form mold

3.3.5.2 Silicone Form

The activated silicone was cast into the cavity of the form mold. It was then struck-off along the face of the mold and support plates and allowed to cure. After curing the mold ring plates were removed, leaving the silicone form around the inner support plates. Figure 35 shows the form mold before and during casting.

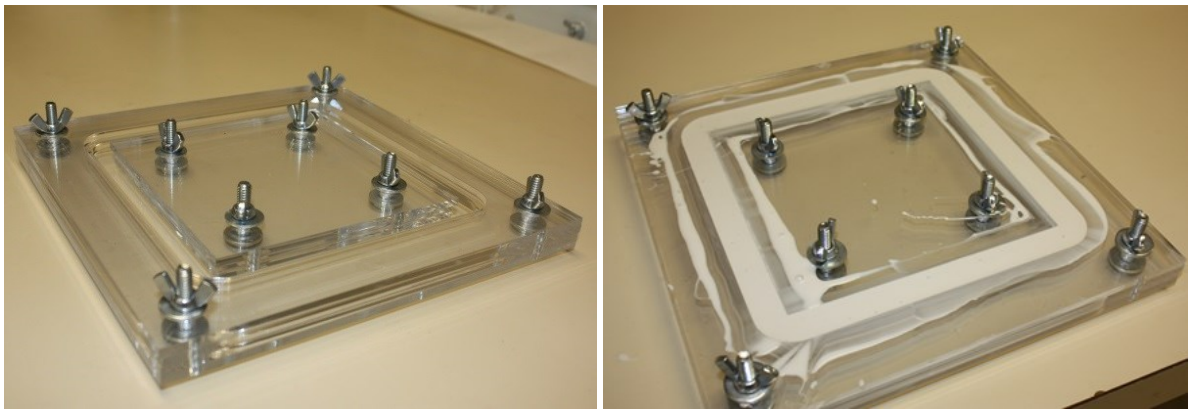

Figure 35: Stirrup form mold before (left) and during (right) silicone casting

3.3.5.3 Jig Assembly

The silicone forms are mounted onto a flat panel surface in series. They were aligned to facilitate multiple simultaneous castings. Anchor and diversion posts were also mounted on the panel to provide support for the necessary sections of fiber yarns that do not pass through the forms.

3.3.5.4 GFRP lay-up

The silicone form molds were coated with a thin layer of the activated epoxy. Fiberglass yarns were then fixed to the anchor point on the panel and extended to align the glass fibers. The yarn was then coated with the activated epoxy along the estimated length that will pass along the silicone form. The coated yarn was then placed into the form channel and another section of yarn was prepared and placed until the yarn had been placed in all of the five casting forms. At the end of the last form, small weights were fixed to the free end of the yarn to act as tensioning devices.

Figure 36: GFRP lay-up of stirrups

3.3.5.5 De-molding/tooling

The GFRP was trimmed of all excess fibers and the stirrups were removed from the jig along with the silicone form. The silicone was removed from the stirrup and returned to the jig. Significant burs and unnecessary epoxy was ground off.

3.3.6 Sand-coating

The standard sand-coating procedure was used to coat all of the GFRP components created. In this procedure, a thin layer of the epoxy resin was applied to its surface. Sand was then poured onto the GFRP and it bonds to the uncured epoxy. The component was then placed on a rack until the epoxy is fully cured.

For the select components of the flexural reinforcement, allowances had to be made for the instrumentation of the reinforcement with strain gauges. Bare GFRP is needed for proper adhesion, so sections of the GFRP cords (two per specimen) were masked at the mid-span before sand coating.

3.3.7 Reinforcement Strain Instrumentation

The tensile stress experienced by the reinforcement used in the specimens was monitored through a network of foil strain gauges. The KFH-10-120-C1-11L3M3R series gauges from Omega Engineering Inc. were fixed to the exposed GFRP near the mid-span of the flexural reinforcement where

reinforcement strain was expected to be the greatest as caused by the maximum moment of the beam. Using this beam geometry, the equations [3.2] and [3.3] are given to provide the maximum moment and shear forces given a load provided and measured by the hydraulic actuator.

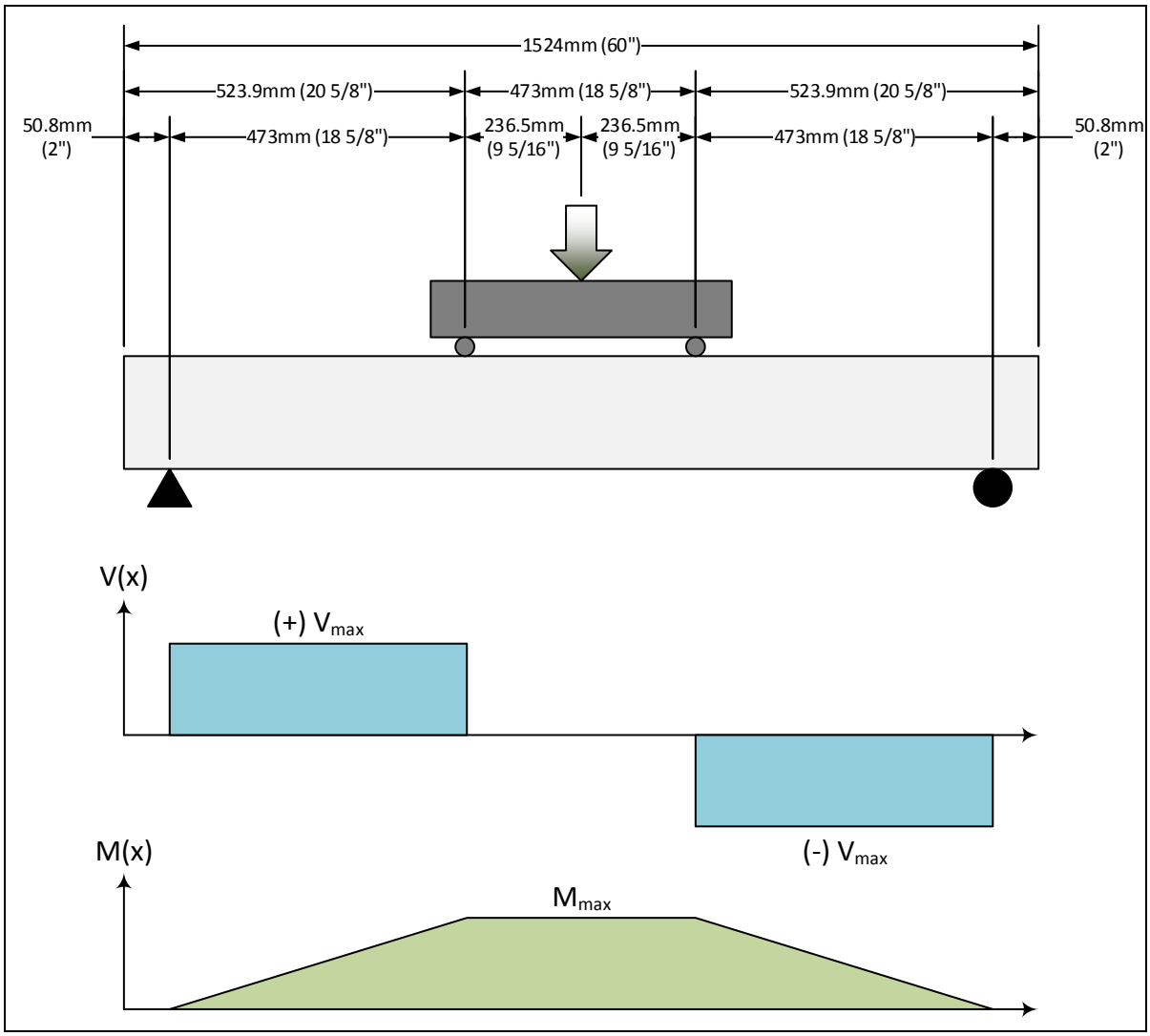

Figure 37: Force location analysis

$$M_{max} = P\left(\frac{l}{6}\right) = 0.2371m \cdot P \qquad [0.9444\, ft \cdot P] \qquad [3.2]$$

$$V = \frac{P}{2} \qquad [3.3]$$

Two strain gauges were located at the upper and lower extremities in order to monitor the strain gradient that varies as a function of beam depth. A cyanoacrylate adhesive was used to bond the gauge to the GFRP surface. A thick coating of epoxy was then applied to the gauge and exposed wires to protect the gauges during the concrete casting.

3.3.7.1 Type I Strain Gauge Configuration

In order to locate strain gauges at the top and bottom extremities of the reinforcement groups, two rods from the type I group were instrumented. The instrumented rods were then configured with one located in the upper row of reinforcement, and one located in the bottom row of reinforcement. This configuration is shown in a diagram in Figure 38.

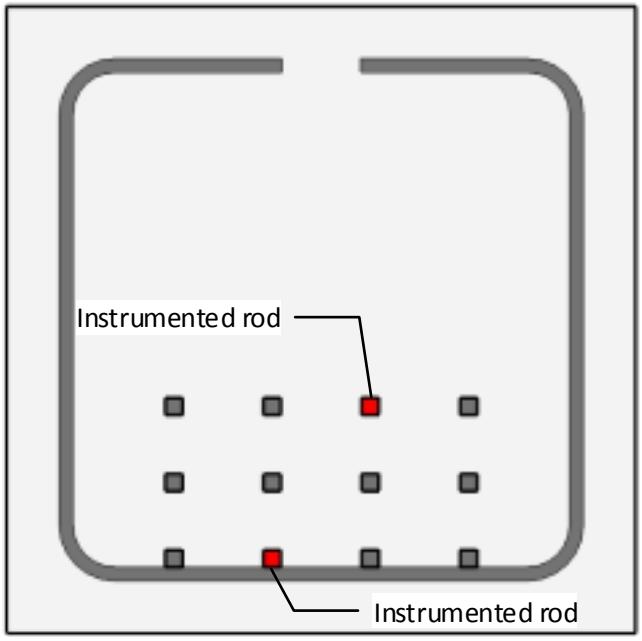

Figure 38: Type I strain gauge location

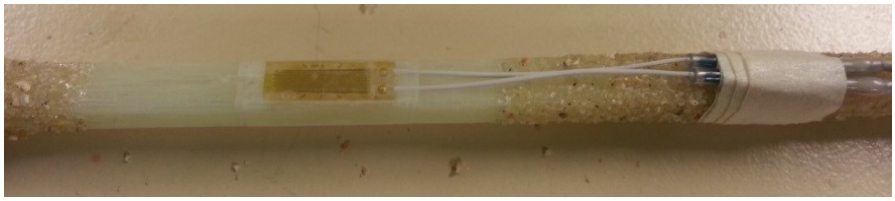

Figure 39: Type I strain gauge

3.3.7.2 Type II Strain Gauge Configuration

To align the strain gauges with the loading axis of the type II reinforced beam, they were attached at cord intersections located near the mid-span of each reinforcing unit as shown in Figure 41. The reinforcement units are oriented so that the gauges are located in the upper and lower extremities of the reinforcing system. A diagram of this configuration is shown in Figure 40.

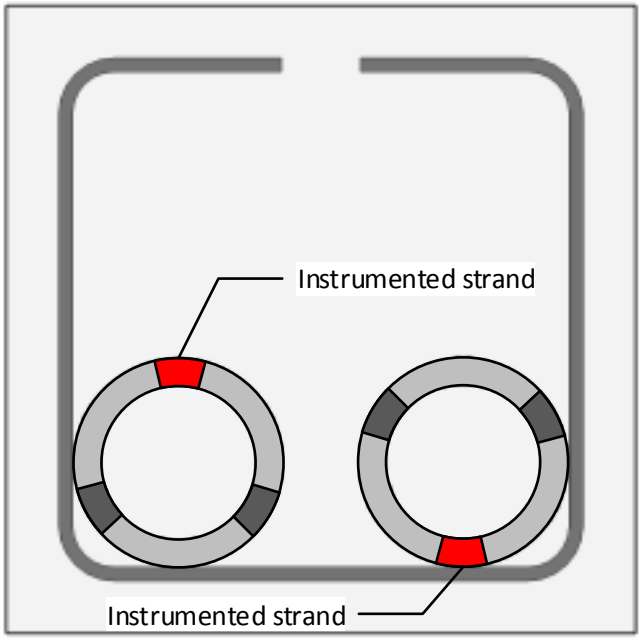

Figure 40: Type II strain gauge location

Figure 41: Type II strain gauge

3.3.7.3 Type III Strain Gauge Configuration

Two cords in each of the type III assemblies are instrumented at a wave peak near the mid-span of the reinforcement. During the assembly of the type III mats, the instrumented cords are oriented to locate the strain gauges at the top and bottom of the mat as shown in Figure 42.

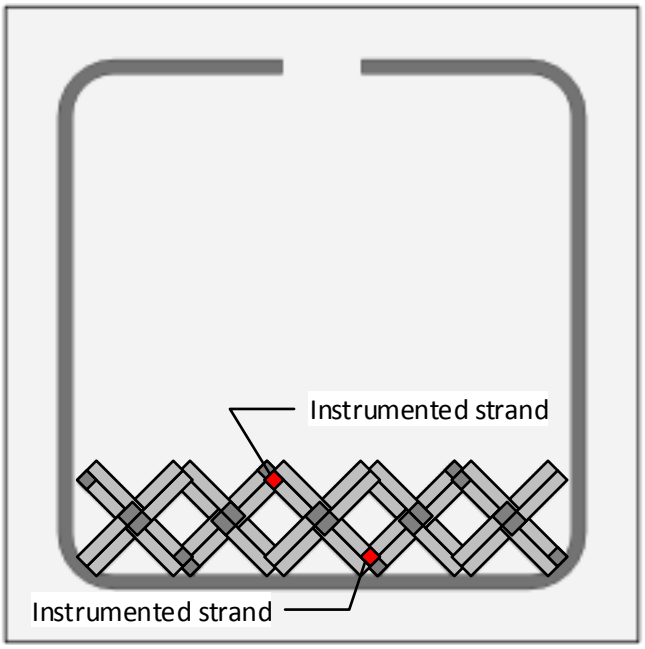

Figure 42: Type III strain gauge location

3.3.8 Reinforcement System Assembly

After strain instrumentation was installed on the GFRP reinforcement, two sets of the six different assemblies described in section 3.2.2 are assembled. 18 gauge tie wire was used to fasten all connections. All of the beams are configured according to the design specifications and drawings shown in Appendix A and Appendix B respectively.

Figure 43: Type Ia reinforcement assembly

3.4 Casting/Curing of Concrete

The concrete for the specimens was cast in four separate pours with three concrete cylinder samples taken from each pour. The cylinders were tested following the ASTM C39/C39M-12a. Table 11 shows the ultimate compressive stress (f'_c) results of these tests.

Table 11: Specimen casting concrete cylinder compression test results

Pour ID	**Specimen ID**	**Ultimate Compressive Stress** (f'_c)
A	Ia-1, Ia-2, Ib-2	27.189 MPa (3943.5 psi)
B	IIa-1, IIa-2, IIb-2	23.242 MPa (3370.9 psi)
C	Ib-1, IIb-1, IIIb-2	29.836 MPa (4327.3 psi)
D	IIIa-1, IIIa-2, IIIb-1	22.183 MPa (3217.3 psi)

Reusable wooden forms were developed for the concrete casting of each specimen. All surfaces of the form to be in contact with concrete were treated to reduce water absorption during the initial curing.

The pour procedures were identical for all four of the specimen beams. 0.27 yd^3 of the Quikrete mix #1101 is mixed for each pour. A w/cm ratio of 0.11 is used in order to achieve an ultimate compressive strength of approximately 27.6 MPa (4 ksi). The concrete was poured into the forms to a depth of 203 mm (8 in) and a mechanical vibrator was used to consolidate concrete to all parts of the form. After a 24 hour initial cure, the specimens were removed from the form where they were cured in the lab. Plastic covering was used to cover the specimens during the 28-day cure time to retain moisture.

Figure 44: Specimen forms assembled with reinforcement in place for pour B

3.5 Instrumentation

3.5.1 Deflection Monitoring

The mid-span deflection behavior of each beam specimen was monitored with the use of a string potentiometer transducer. A sacrificial string was run from an anchor point at the mid-span on the bottom of the specimen. The string was diverted to the string potentiometer located in a protective housing to avoid possible damage from the failing beam shown in Figure 45. The string potentiometer produces a resistance that was read and recorded by the CR 1000.

Figure 45: String potentiometer arrangement

3.5.2 Force Monitoring

The force applied to the beam were determined by monitoring the load forces applied by the actuator and resulting load effects, i.e. moment and shear, were computed. The p-delta transducer within the actuator was used to apply the desired force. Specifically, it is an internal force sensor housed in the MTS 244.23 hydraulic actuator. The signal this sensor provides was first read by the MTS Flextest GT. The Flextest GT applied calibration adjustment and relayed the signal to a Cambel Scientific CR1000 data logger.

From the force data that was recorded in the CR1000, the corresponding shear and maximum moment values found in the specimens was calculated using the beam geometry presented in Figure 37.

3.6 Testing Procedures

The twelve specimens were all tested using the same self-reacting loading frame. A rendering of this loading frame is shown in Figure 46. The Ia-2 and Ib-2 specimens were tested under load control conditions with a constant loading rate of 453.6 kg/sec (1,000 lb/sec). Due to unstable control errors produced by the hydraulic actuator system, the remaining specimens were tested in deflection control with a displacement rate of 0.01577 mm/sec (0.0006209 in/sec). For both of these loading methods, force was applied to the specimen until complete collapse occurs or deflections well above serviceability thresholds are reached.

Figure 46: Testing frame rendering

Chapter 4

Experimental Results

The twelve beam specimens were tested to determine their behavior in multiple facets of structural performance. During the experimental testing, three types of data were collected for the duration of loading until significant failure was achieved where ultimate strength and serviceability states were exceeded. Table 12 describes the various sources of data recorded from the tests and the structural traits that are derived from these sources.

Table 12: Specimen data outline

Data Source	**Structural Traits**
Applied loading	Flexural Strength Shear Strength
Beam deflection	Deflection Behavior Beam Stiffness
Reinforcement strains	Average reinforcement stress Maximum reinforcement stress Strain gradient

Each test was videoed and photographed in order to create a record of the visible damage that resulted from the loading. This visual evidence was used to sync and categorize visible damage events with internal events that were monitored with the specimen instrumentation. The categories used to define the damage events are as follows:

- **Flexure-tension cracking (F-T)**

  Cracking caused by flexural forces in the tension zone typically located at the bottom portion of the beam between the loading points, and propagating upward.

- **Flexure-compression cracking (F-C)**

  Cracking caused by flexural forces in the compression zone typically originating along the top portion of the beam spanning horizontally, and propagating outward towards the loading points.

- **Flexural compression swelling (F-Cs)**

  Visible upheaval caused by flexural micro-cracking in the compression zone at the top of the beam between loading points and expanding upwards.

- **Shear (Sh)**

  Diagonal cracking caused by shear forces at the regions between the loading points and the supports.

- **Interface slipping (IS)**

  The sudden shifting of fractured concrete along the fracture interfaces.

- **Internal compression (IC)**

  Cracking caused by internal constriction forces originating near the mid-span at the level of the flexural reinforcement and propagating outward.

The following sections provide a description of the given key structural behaviors for each specimen. Behaviors unique to each type of specimen will also be described in detail, followed by a discussion, interpreting of the sources of the unique behaviors.

4.1 Flexural Strength Behavior

4.1.1 Type Ia - Conventional Beam with Stirrups

4.1.1.1 Ia-1 Results

After previous testing attempts[2], the beam was successfully loaded to failure. During the loading, three types of failure modes (F-T, F-C, and Sh) were indicated by crack initiation and propagation before a sudden complete collapse occurred. Figure 47 shows a chronological record of events with maximum resisting moment and reinforcement strain values throughout the procedure.

[2] Testing was first attempted under load-controlled conditions 453.6 kg/min (1 kip/min). Loading reached 11.71 kip and the actuator used began experiencing an unstable feedback loop. The loading procedure was then aborted.

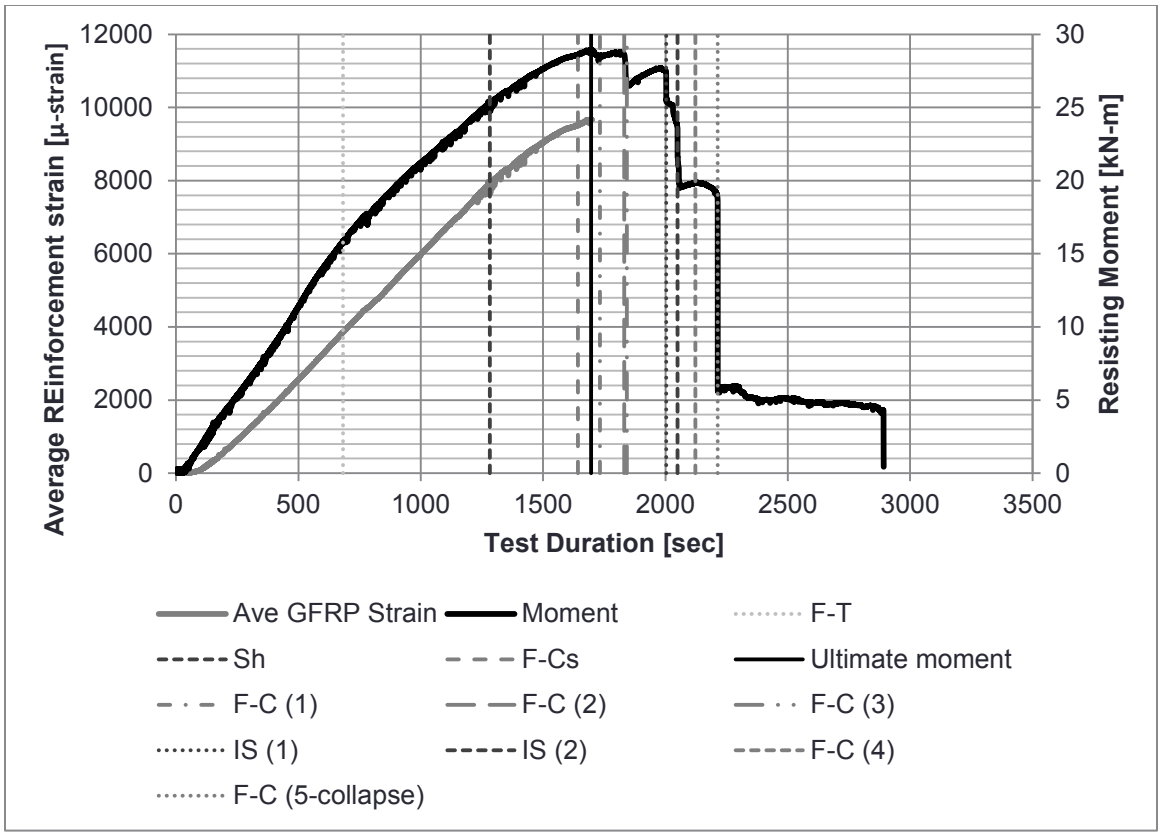

Figure 47: Ia-1 testing events

This specimen exhibited unique behaviors with the presence of flexural-compression damage. Flexural-compression swelling began to manifest when the resisting moment reached 28.6 kN-m (21.1 kip-ft). This was just before the ultimate moment was reached at 28.9 kN-m (21.3 kip-ft).

In the testing of this specimen, visible compression cracking occurred in four phases. These flexural-compression cracks began forming at the mid-span near the top of the beam. New cracks formed, progressing downward through the beam as shown in the series of images in Figure 48.

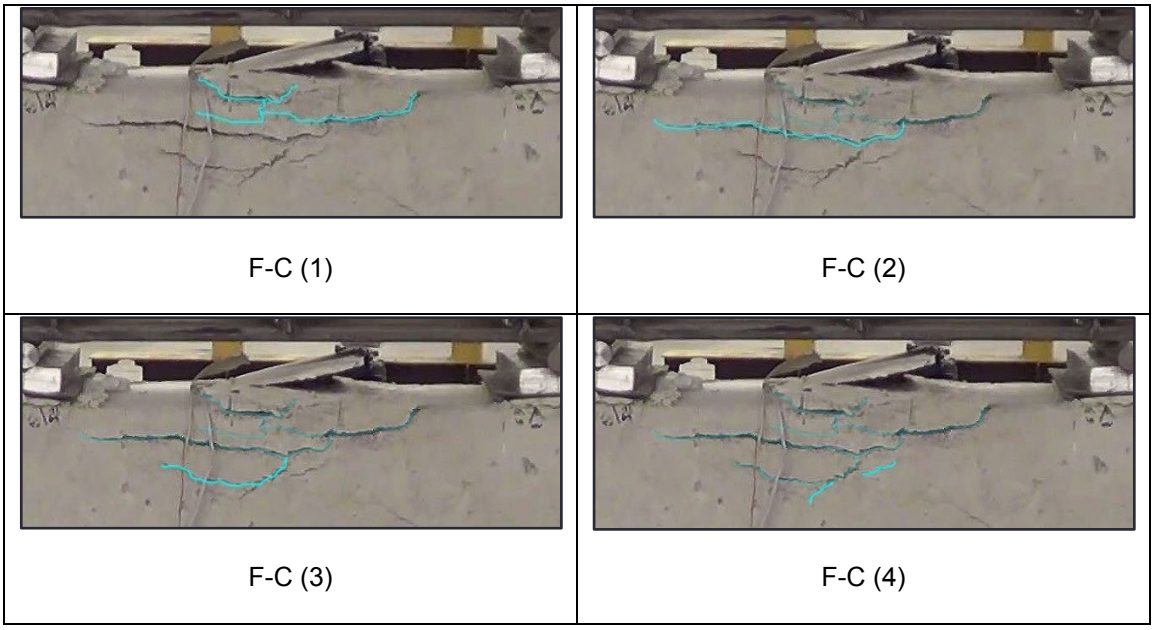

Figure 48: Compression cracking

The next significant events in the testing procedure involved two occurrences of crack interface slipping in the compression damaged zone. These slips occurred at 26.3 kN-m (19.4 kip-ft) and 23.6 kN-m (17.4 kip-ft). Both slipping events produced significant drops in resisting moment.

A sudden flexural-tension crack completely fracturing the full cross-section of the beam occurred at a maximum moment of 18.4 kN-m (13.6 kip-ft). This weakened the total beam resisting moment by about 12 kN-m (8.85 kip-in). It is after this failure that the beam was considered completely failed, and the test stopped.

4.1.1.2 Ia-2 Results

Loading of the Ia-2 specimen was advanced until it exhibited damage characteristics from flexural-compression immediately before the complete tensile failure of the reinforcement at the time of failure. Figure 49 shows a chronological record of the damage events compared with maximum moment and reinforcement strain values throughout the procedure.

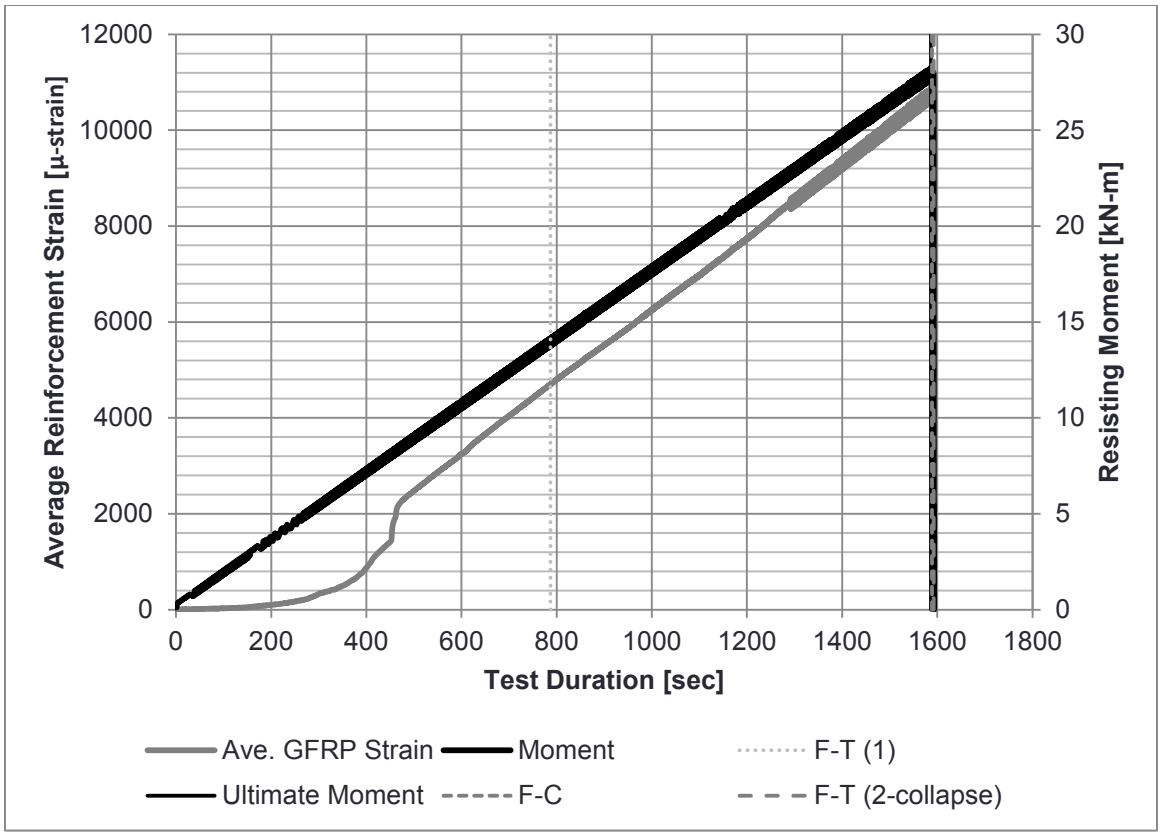

Figure 49: Ia-2 testing events

At a resisting moment value of 14.1 kN-m (10.4 kp-ft), the specimen began exhibiting signs of visible flexural-tension crack initiation at the bottom of the beam. These cracks continued to propagate vertically upwards throughout the loading period.

Visible compression damage begins to show at an ultimate moment of 28.3 kN-m (20.9 kip-ft). This damage is characterized by horizontal cracks ranging from 25 – 50 mm (1 - 2 in) below the top surface of the beam, and extending approximately 130 mm (5.12 in) from the mid-span in each direction until they terminate. Just after the ultimate load was achieved, complete collapse of the beam occurred as a result of flexural-tensile failure.

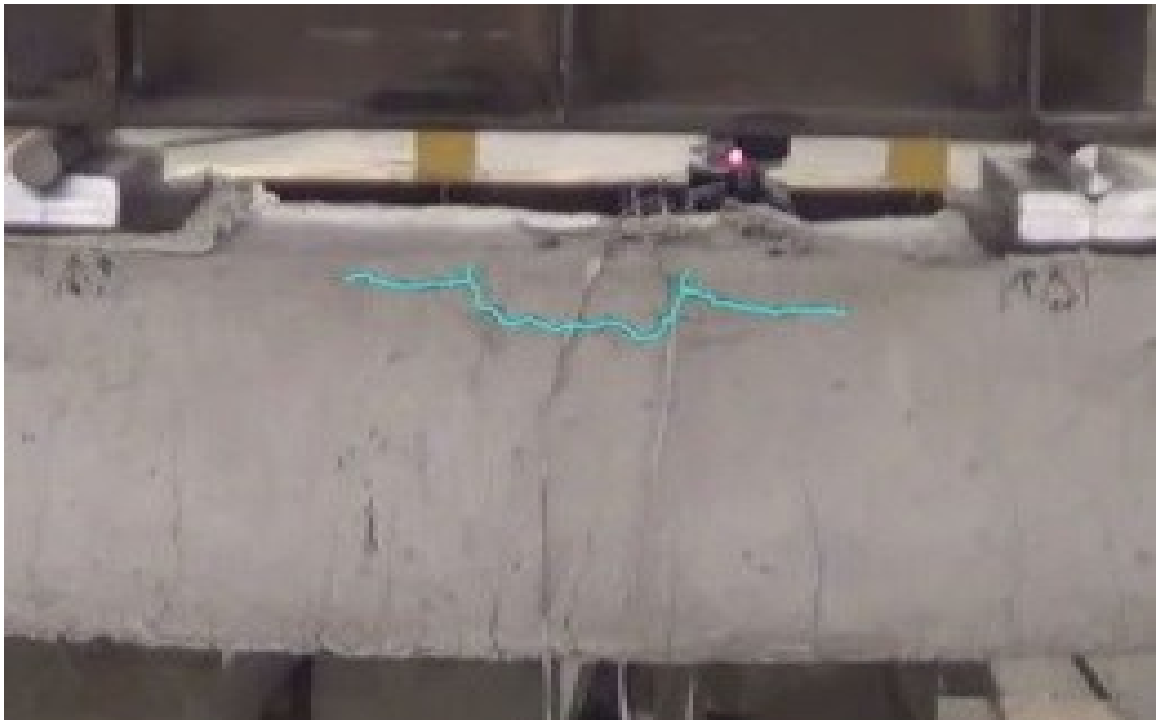

Figure 50: Ia-2 compression damage

4.1.1.3 Discussion

The flexural-compression damage behavior exhibited in the Ia-1 specimen is typically desired for GFRP reinforced concrete beams according to current standards (ACI 440.1R-06). This compressive damage behavior is designed into the beam in order to promote progressive failure in lieu of beam ductility achieved by using steel reinforcement. This was not the intention of the specimen design though, and it is thought that this compressive failure has occurred due to the quality of the concrete. In this experiment, the isolated behavior of the GFRP reinforcement without the influence of concrete failure is desired. Therefore, the data from the Ia-1 specimen was discarded from further analysis.

The specimen Ia-2 exhibited typical tension controlled flexural behavior with the complete tensile fracture of the GFRP reinforcing bars. This specimen will be regarded as the typical expected behavior for conventional GFRP reinforcement under tensile control conditions.

4.1.2 Type IIa – Helical Reinforcement with Stirrups

4.1.1.1 IIa-1 Results

By observing the progressive damage patterns of the shear reinforced helical GRFP specimen IIa-1, it can be noted that flexural cracking forms at regular intervals along the bottom of the beam (represented by the red annotations in Figure 51). However, this cracking terminates at the approximate level of flexural reinforcement, and no further flexural-tension crack propagation appears. The termination points of these cracks are ultimately joined by horizontal cracking running parallel to the flexural reinforcement.

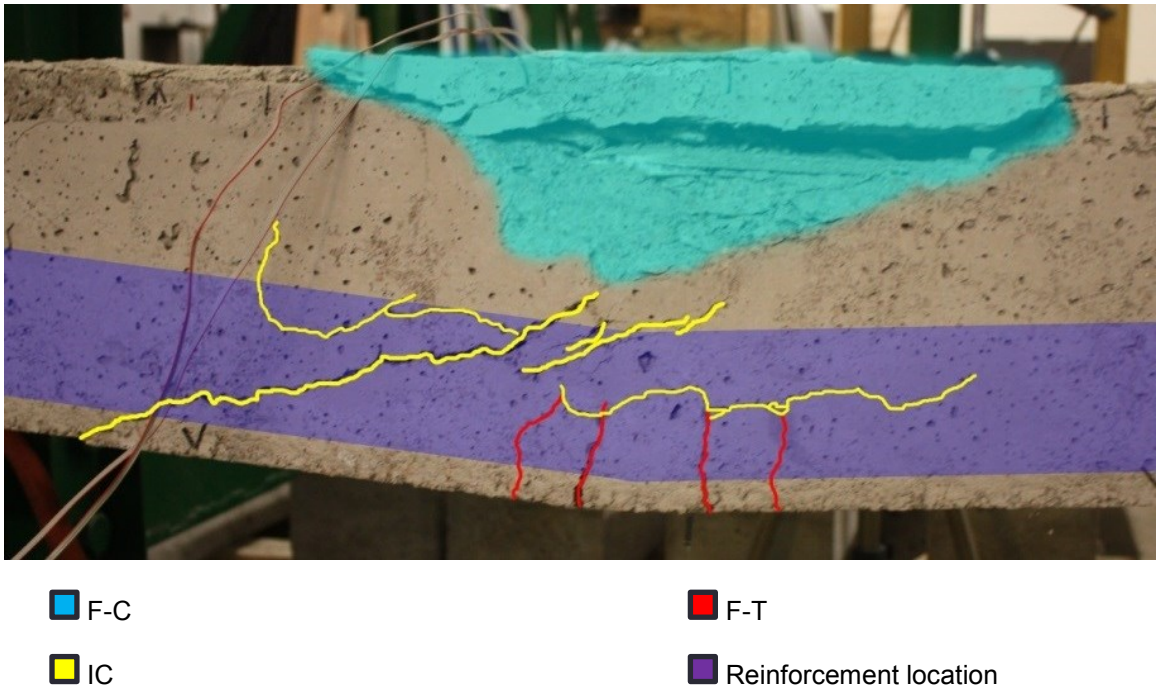

Figure 51: Specimen IIa-1 annotated failures

The beam reaches its ultimate loading with a resisting moment of 26.7 kN-m (19.7 kip-ft). After this point, flexural-compression damage begins to manifest in several stages as shown in Figure 52. The first of two sudden compression failures initiates and a 38.1 mm (1.50 in) section of concrete spalls off the top face of the beam between the loading points (see Figure 51). The loading was continued until the flexural-compression damaged completely depleted the beam resistance.

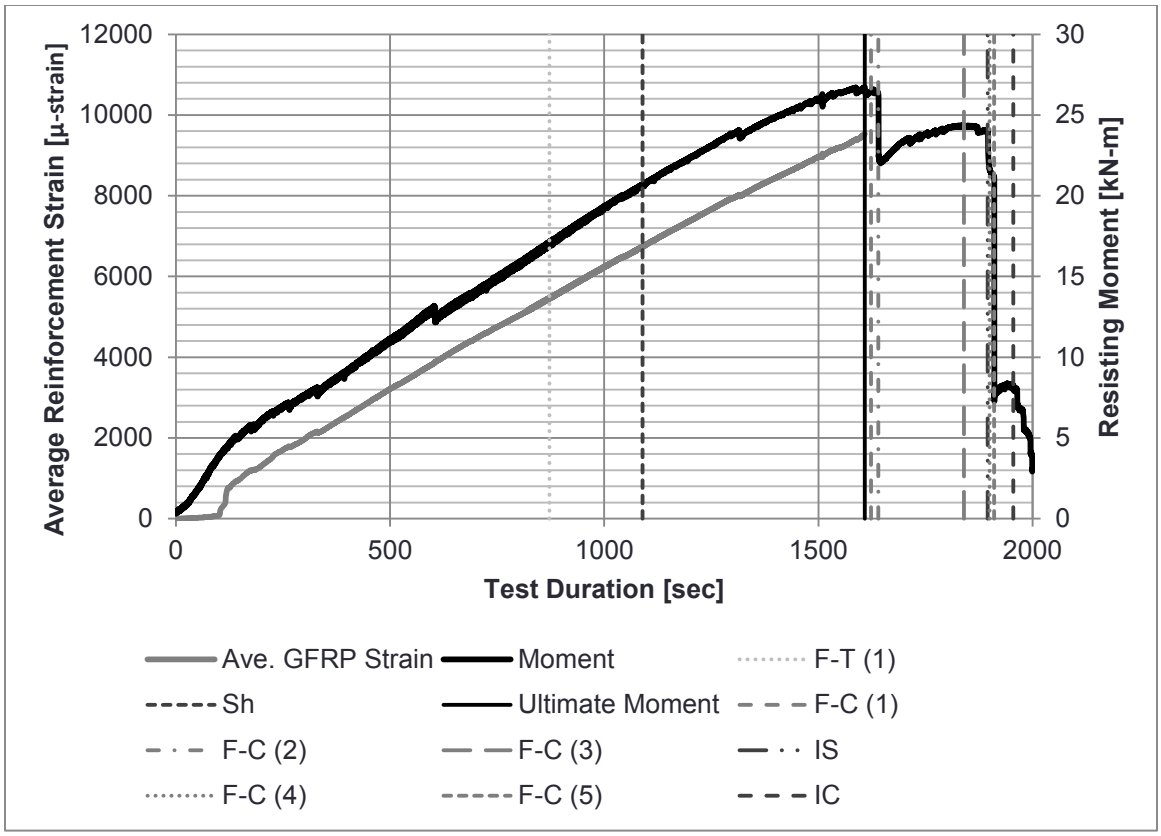

Figure 52: IIa-1 testing events

4.1.1.2 IIa-2 Results

The primary failure location of the IIa-2 specimen was located outside of the maximum flexural moment zone. Signs of shear and flexural-tension damage were evident in the failure of this specimen. The testing events shown in the chart in Figure 53, indicate that early signs of shear damage in the form of diagonal cracking that widened as loading progressed.

Flexural-tension cracking then appeared when the moment reached approximately 12.8 kN-m (9.44 kip-ft). The resisting moment to continue to climb to a peak value of 25.6 kN-m (18.9 kip-ft) before it began to shed load. A sudden flexural-compression failure event then occurred shortly after the beam's force resistance began to drop. This flexural-compression cracking appeared to influence the widening and internal slipping of the initial shear crack formation until virtually no loading was being resisted by the beam. The image in Figure 54 indicates the varieties of damage visible and relative locations after the testing procedures.

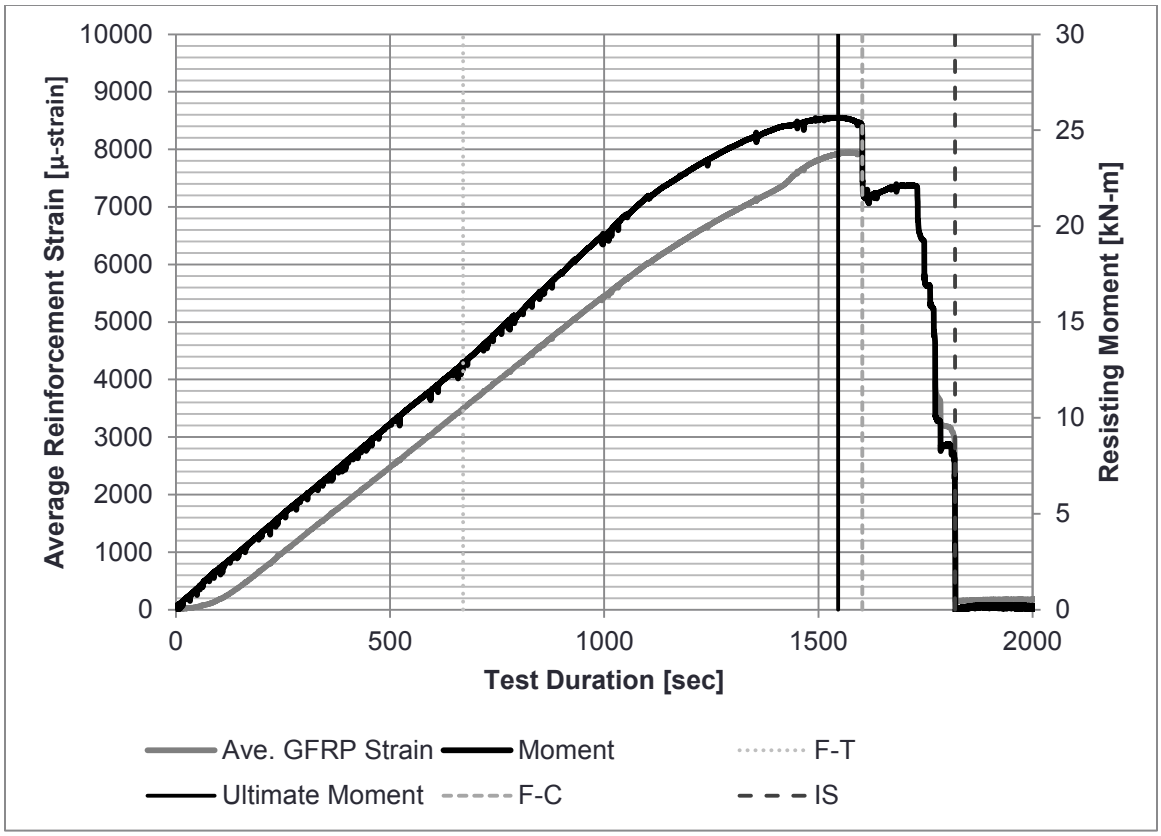

Figure 53: IIa-2 testing events

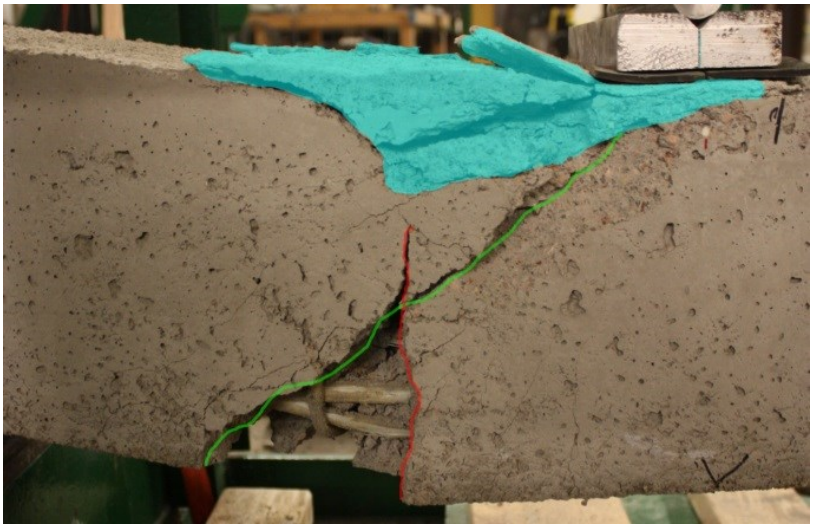

Compression failure
Shear failure
Flexural failure

Figure 54: IIa-2 annotated failure

4.1.1.3 Discussion

Flexural-tension failure mode was partially achieved during testing of these specimens; however the ultimate failure appeared to be primarily controlled by a concrete compression failure mode. While unwanted flexural-compression damage was experienced, the damage behavior of the IIa-1 specimen provided strong indications of the intended constriction effect of the flexural reinforcement. These indications are shown by the presence of the horizontal internal cracking.

The failure behavior of specimen IIa-2 did not comply with the intended design of the specimen. Loss of beam depth from concrete compression failure is thought to be the source of the inconsistent behavior. Since significant flexural-compression damage did not occur until the time that ultimate strength was reached data during the load gaining stage of the test will be used for analysis.

The effectiveness of the reinforcement configuration used in both of these specimens is supported by the flexural-compression failure mode that the specimen exhibited. This indicates that the beam may be over-reinforced for tension controlled conditions to occur. An over-reinforced condition was not present in the Ia-2 control specimen, meaning that flexural gains could have been achieved by the concept reinforcement geometries.

4.1.2 Type IIIa – Wave Reinforcement with Stirrups

This series of reinforcement combines the sine wave mat with shear stirrups to induce flexural forces to act as the primary mode of failure. Despite the maximum moment being located between the loading points, both beam failures occurred outside of the two loading areas. After the initial concrete fractures a region of progressive load “stepping” was observed with load linearly increasing and then suddenly shedding load. The stepping continued with a downward trend until no loading was being resisted.

4.1.2.1 IIIa-1 Results

The key unique behaviors exhibited by the IIIa-1 specimen can be isolated into three different stages of loading. The first of which is identified as the initial “load-gaining” stage, at approximately 0-375 sec of the testing duration, where the beam generally resists the advancement of the loading actuator from. During this stage the cracking moment is achieved at approximately 5.74 kN-m (4.23 kip-ft) where a

dramatically loss in stiffness occurs and then is quickly recovered. The initiation of flexural-tension cracking is then observed as loading continues.

Figure 55: IIIa-1 after testing

The second stage of loading occurring at approximately 375 - 925 sec of testing duration indicates a “stable load-shedding” behavior where shedding initially begins after a moment of 5.74 kN-m (4.23 kip-ft) is achieved 377.2 sec into the loading procedures. The load building and shedding occurs at a range of 4.82 – 5.54 kn-m (3.56 – 4.09 kip-ft) without a significant trend towards net load gain or shedding. The ultimate load for the specimen was reached at 5.91 kN-m (4.36 kip-ft) where the third stage of loading begins.

The third stage occurs between approximately 925 sec into the testing duration and continues until the testing procedures are terminated. During this stage of loading an “unstable load-shedding” behavior is observed where a load stepping condition is observed with a downward trend on beam net resistance. This downward trend continues until the beam no longer provides load resistance.

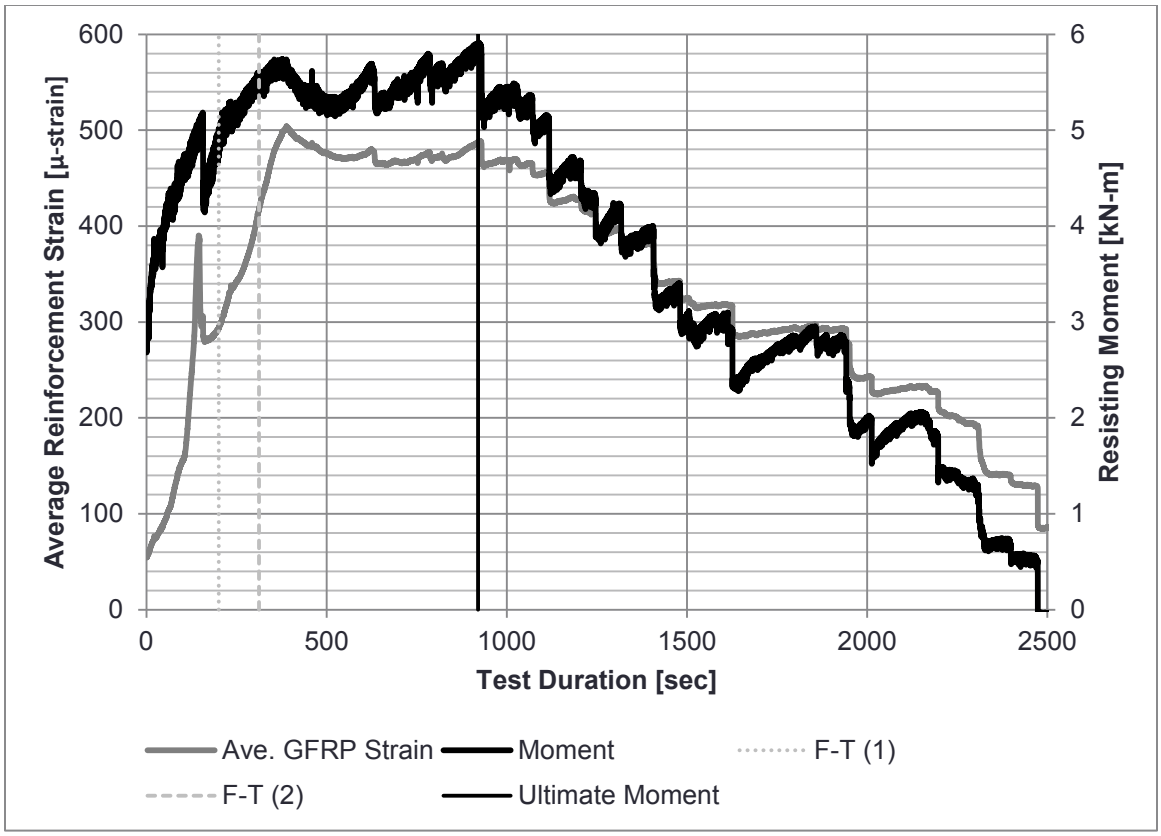

Figure 56: IIIa-1 testing events

4.1.2.2 IIIa-2 Results

The type IIIa-2 specimen initially exhibited similar behaviors as seen in the IIIa-1 specimen. The main difference being that the IIIa-2 specimen did not exhibit a significant “stable load-shedding” stage that was seen in the IIIa-1 test.

Several flexural-tension cracking events occurred during the building portion of the load applications. As the resisting moment increases the flexural-tension crack beneath the left loading point shown in progressively opens, as shown in Figure 57. Flexural resistance in the beam continued building until an ultimate moment of 11.4 kN-m (8.41 kip-ft) was reached.

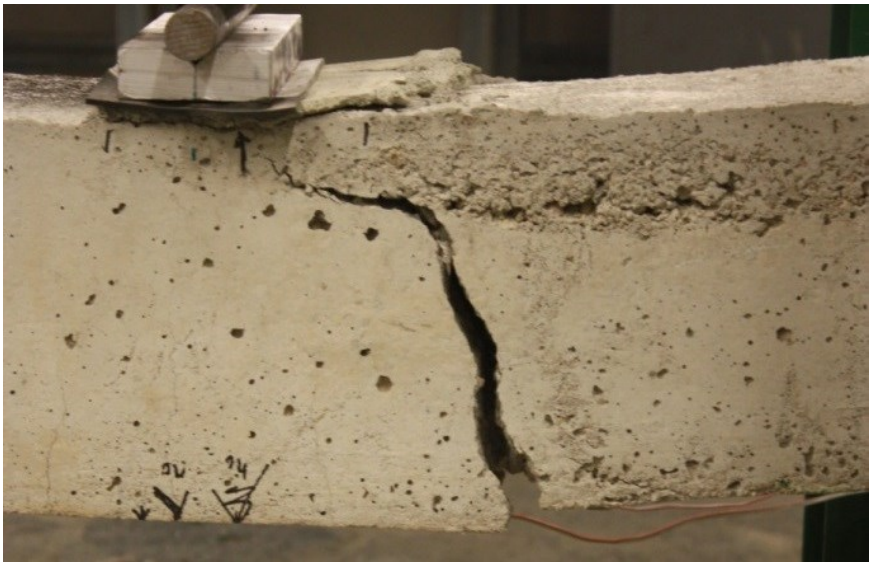

Figure 57: Primary flexural crack in IIIa-2

After the ultimate moment is achieved a large drop in resistance occurs, followed by a progressive load shedding of the resisting forces. The load shedding behavior continues until no load is being resisted by the beam and the loading procedures are terminated.

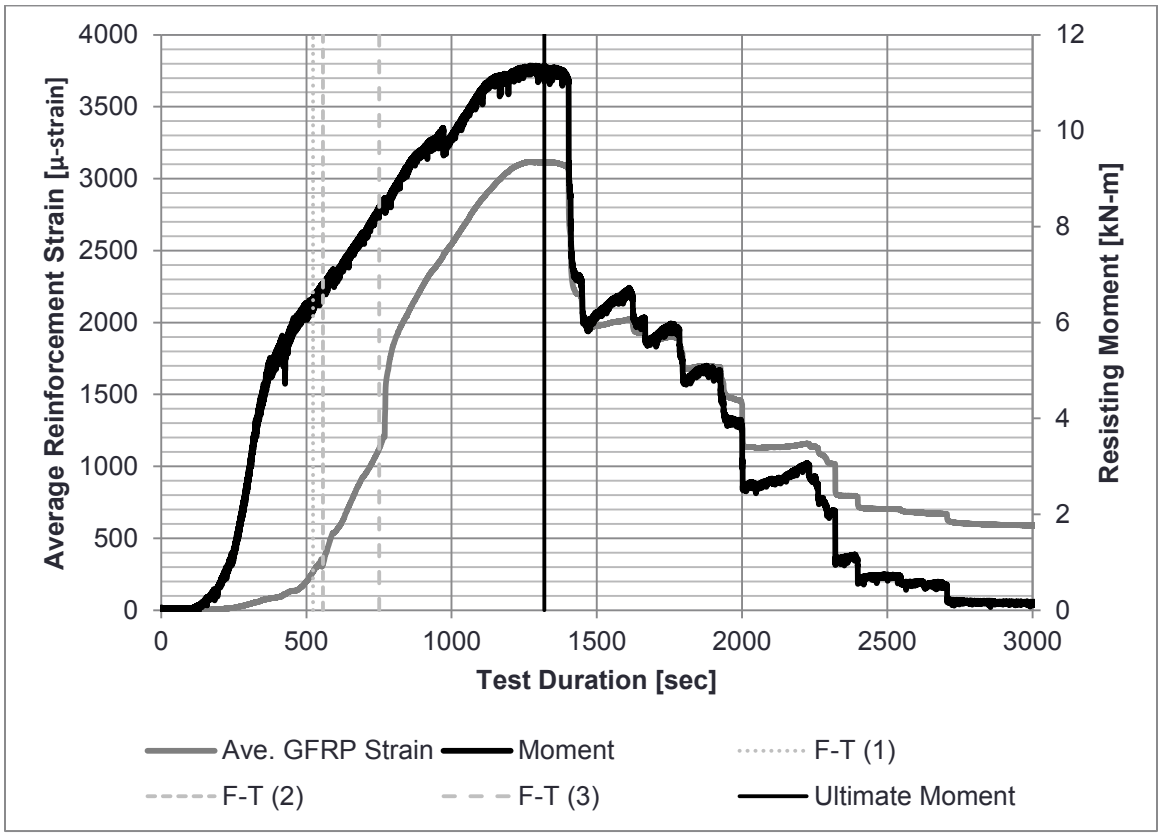

Figure 58: IIIa-2 testing events

4.1.2.3 Discussion

The unique behavior exhibited by the type IIIa specimens includes the presence of the stepping behavior observed in the load shedding phase of the testing. This action was likely caused by the entanglement of the flexural reinforcement as it was pulled by the flexural-tension forces from the cracked faces of the beam. This behavior could likely be reduced or eliminated with changes in the design geometry.

Low flexural resistance is postulated to result from poor tensile stiffness characteristics of the short wavelength wave configuration used in these specimens. The function of this design allows for excessive deformation of the concrete matrix leading to premature brittle failure and spalling of concrete essential for the constrictive behavior of the reinforcement to be effective.

4.2 Shear Strength

4.2.1 Type Ib – Conventional Beam without Stirrups

4.2.1.1 Ib-1 Results

Typical shear failure behavior showing diagonal cracking extending from the loading point to the beam support was exhibited. All visible damage is categorized as shear failures. Figure 59 exhibits significant observable events that occurred during the test, and the corresponding maximum moment and average reinforcement strain over the duration of the testing procedure.

The maximum shear force experienced by the beam reaches 70.1 kN (15.8 kip), where it began to exhibit a sudden shear crack formation. This crack spans a diagonal distance from the left loading point to the left support roller.

As loading continued the shear crack widened significantly followed by a series of interface-slipping events. The first of these slipping events resulted in a significant drop in load resistance from the beam. The photo in Figure 60 shows the shear crack after the slipping action has taken place. After a period of continued loading, a second interface-slip occurs just before the complete collapse of the beam. The collapse is a result of a complete failure in the GFRP reinforcement.

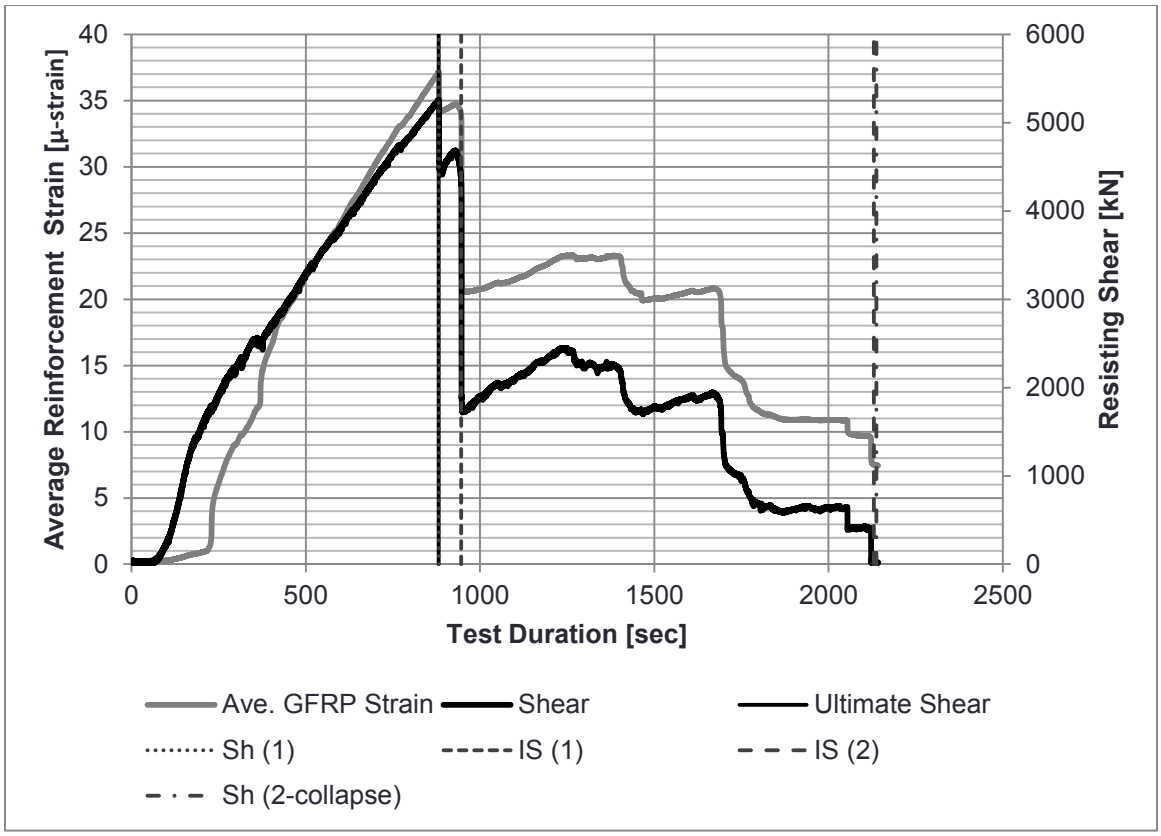

Figure 59: Ib-1 testing events

Figure 60: Ib-1 shear crack (rear view)

4.2.1.2 Ib-2 Results

Several aborted tests were attempted on Ib-2 before a successful and completed test was achieved[3]. The damage behaviors observed in this test can all be categorized as shear controlled events. Figure 61 illustrates the observable damage and failure events taking place during this test in relation to the measured shear forces and average reinforcement strain.

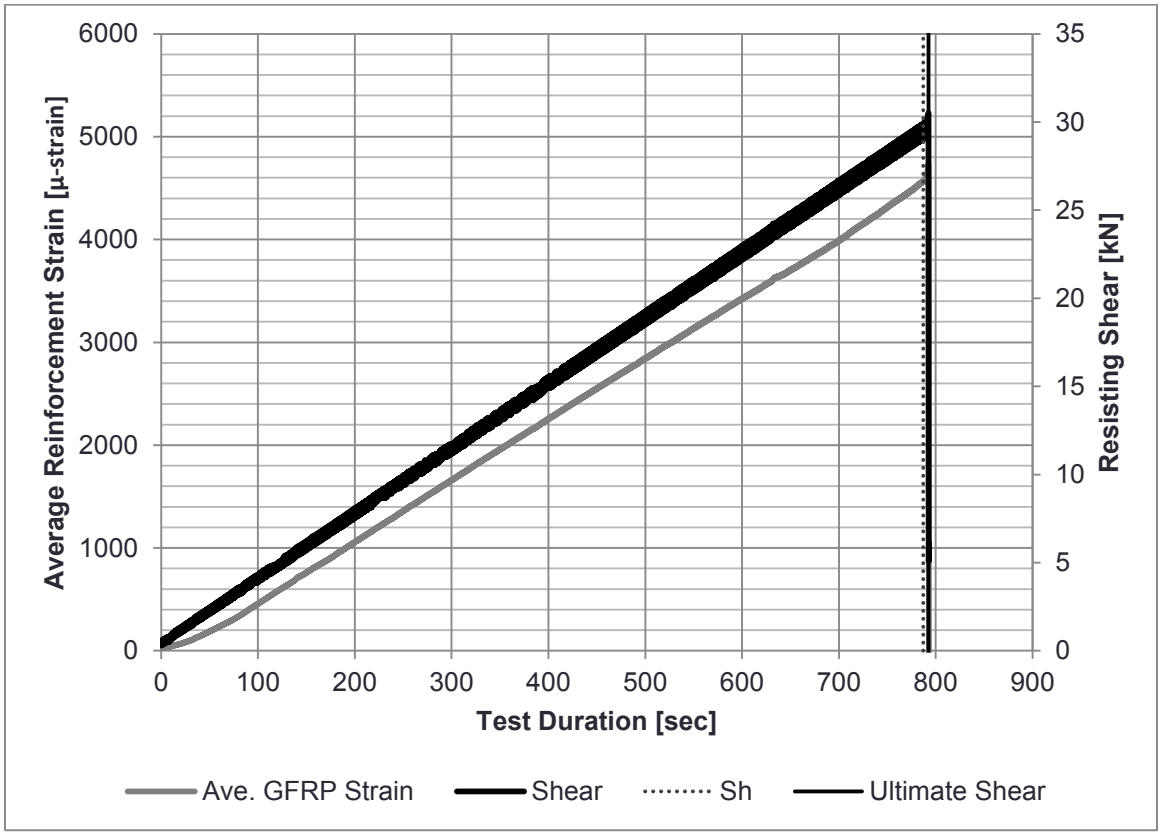

Figure 61: Ib-2 testing events

[3] Previously aborted test of Ib-2 include:

- (1st) Midpoint loading was aborted after 23.5 kN was reached due to indications of structural instability in the loading frame
- (2nd) Midpoint loading was aborted after 14.8 kN was reached due to indications of structural instability in the loading frame
- (3rd) Midpoint loading was aborted after 36.2 kN was reached due to indications of structural instability in the loading frame
- (4th) Midpoint loading was aborted after 57.9 kN was reached due to the occurrence of a feedback loop error in the hydraulic actuator system

As loading is applied, little to no apparent indications of damage were observed until the beam reached 29.9 kN (6.73 kip) of maximum shear force. At this point a small shear crack quickly formed to the left of the left loading point and extended diagonally to the left roller bearing. This crack branches into two different cracks before it terminates at both the top and bottom of the beam. Figure 62 illustrates the observed cracking pattern.

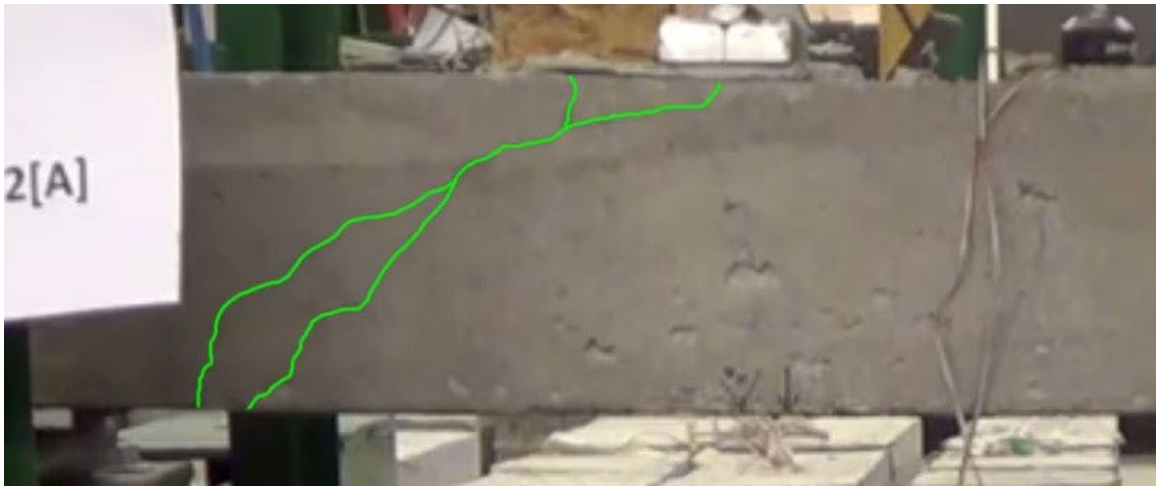

Figure 62: Ib-2 initial shear cracking

The shear force reaches 30.5kN (6.86 kip) when the ultimate failure of the beam occurs. This was a sudden failure along the initial shear crack formation.

4.2.1.3 Discussion

Both of the Ib specimens exhibited similar failure behaviors, with the Ib-1 ending in a more sudden collapse immediately after the ultimate load is achieved. This immediate collapse can be attributed to the force-controlled loading procedures that were used.

It can be noted that after inspection of the collapsed Ib-2 specimen, evidence of debonding failure was found for the bottom row of reinforcing bars. Three of the bars shown in Figure 63 remained intact after the full collapse of the specimen indicating insufficient bond. Similar evidence to a lesser extent was observed in the remains of the Ib-1 specimen which left one bar in the bottom row of reinforcement partially intact after failure.

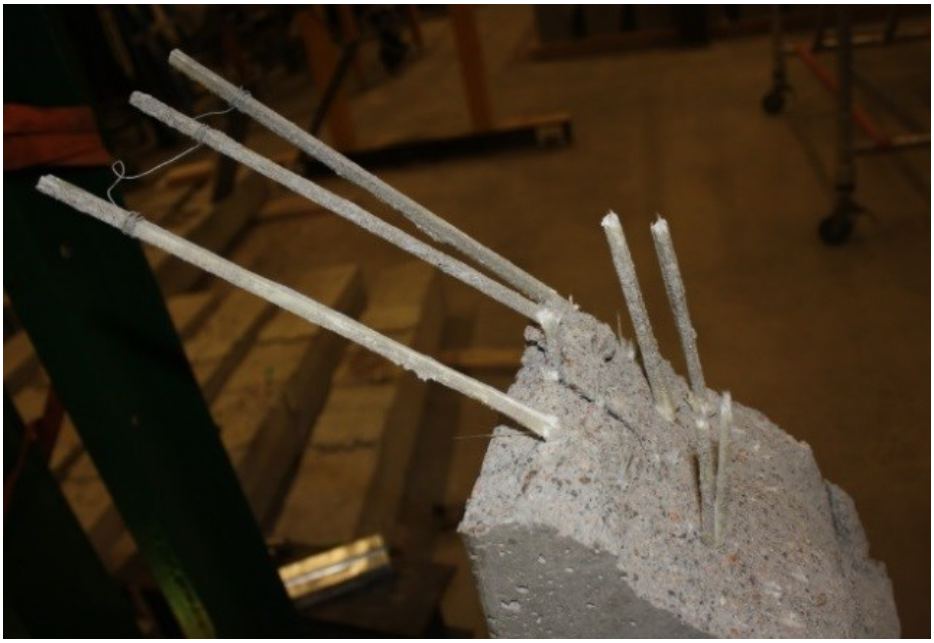

Figure 63: Debonding failure of Ib-2

4.2.2 Type IIb – Helical Reinforcement without Stirrups

4.2.2.1 IIb-1 Results

The IIb-1 specimen exhibited shear cracking on both ends of the beam during the loading, with the right end crack hosting the ultimate failure of the beam. The chart in Figure 66 indicates that the load resistance of the beam remained relatively stable and that these shear cracks did not begin to appear until approximately 14 – 15 kN (3.1 - 3.4 kip) of shear force had been applied. The cracks were located at the typical shear fracture locations, running diagonally from the loading points on each side to the support rollers, as shown in Figure 64. However, these cracks did not propagate past the point of the flexural reinforcement until the time of the collapse event that is shown in progress in Figure 65. This collapse occurred at the time that the ultimate shear forces of 44.2 kN (9.94 kip).

Figure 64: IIb-1 shear cracking before collapse event

Figure 65: IIb-1 at time of collapse

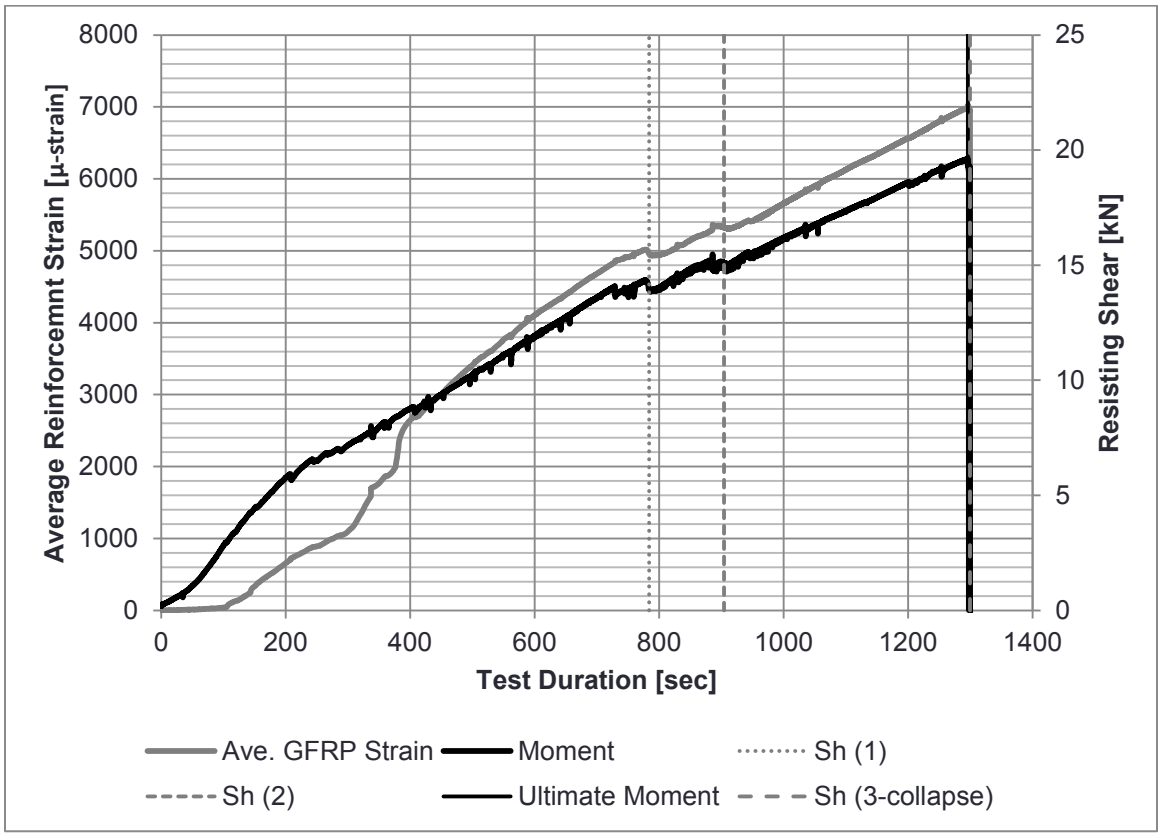

Figure 66: IIb-1 testing events

4.2.2.2 IIb-2 Results

The IIb-2 exhibited shear cracking formation on only the left side of the maximum shear region between the left loading point and left supports. The crack formed immediately after the ultimate applied shear force of 27.0 kN (6.07 kip). Rather than exhibiting typical shear failure behavior by exiting at the bottom of the beam, the cracking propagated to the end face of the beam as shown in Figure 67. A

progressive failure followed the ultimate shear force as illustrated in Figure 68. As loading continued flexural-tension cracking began to form in the concrete beneath the shear fracture. Complete collapse was achieved as the reinforcement in the damaged region failed at a negligible shear force. This failure path left a shallow section of concrete and reinforcement to support the loading, which quickly failed locally in flexure-tension.

Figure 67: IIb-2 failure patterns before collapse

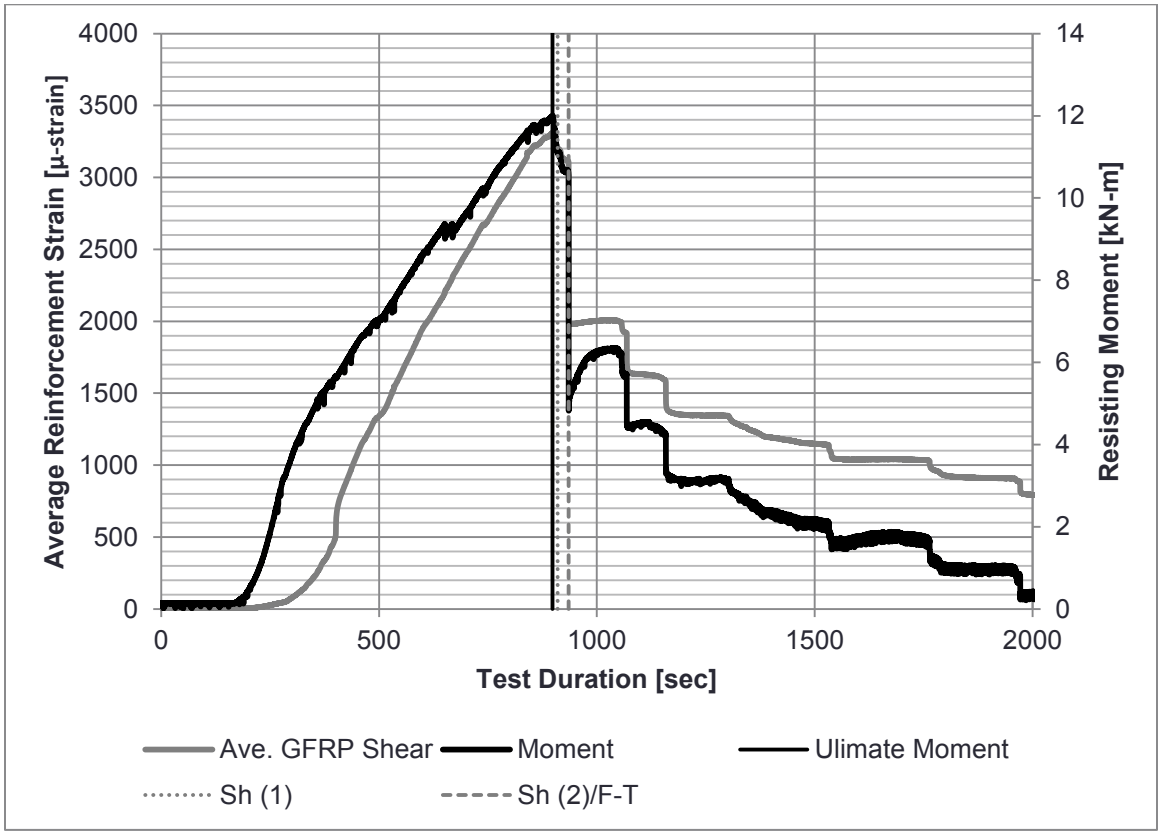

Figure 68: IIb-2 testing events

4.2.2.3 Discussion

The most notable common unique behavior exhibited by these specimens is the primary cracking path, which diverted around the flexural reinforcement. These cracks spanned from the loading point to the end face of the beam, which greatly reduced the effective depth of the remaining beam section below this shear fracture. This weakened portion of the beam collapsed from localized flexural failure.

In the IIb-1 sample the initial shear cracks were momentarily arrested at the level of the flexural reinforcement. This behavior serves as an indication that the reinforcement configuration is supplying shear force resistance. Further evaluation of the type II configuration, with modifications to the system parameters, would be necessary in order to quantify the shear strength contribution.

4.2.3 Type IIIb – Wave Reinforcement without Stirrups

4.2.3.1 IIIb-1 Results

The IIIb-1 specimen exhibited multiple flexural-tension cracks. As loading builds, a vertical flexural-tension crack forms directly beneath the left loading point and progressively widens. Shortly after the ultimate shear load of 18.6 kN (4.18 kip) is achieved, a second flexural crack opens beneath the loading head and progressively opens as the loading is advanced. These two cracks are then joined by horizontal cracking as seen in Figure 69. The concrete in the region between the main flexural cracks then began to spall off, exposing the reinforcement. At this point, a region of load shedding is observed where load is built up and released in a stepping progression. The spalling of concrete continues as the beam deflects further, leading to an ultimate collapse at a negligible applied shear force.

Figure 69: IIIb-1 during testing

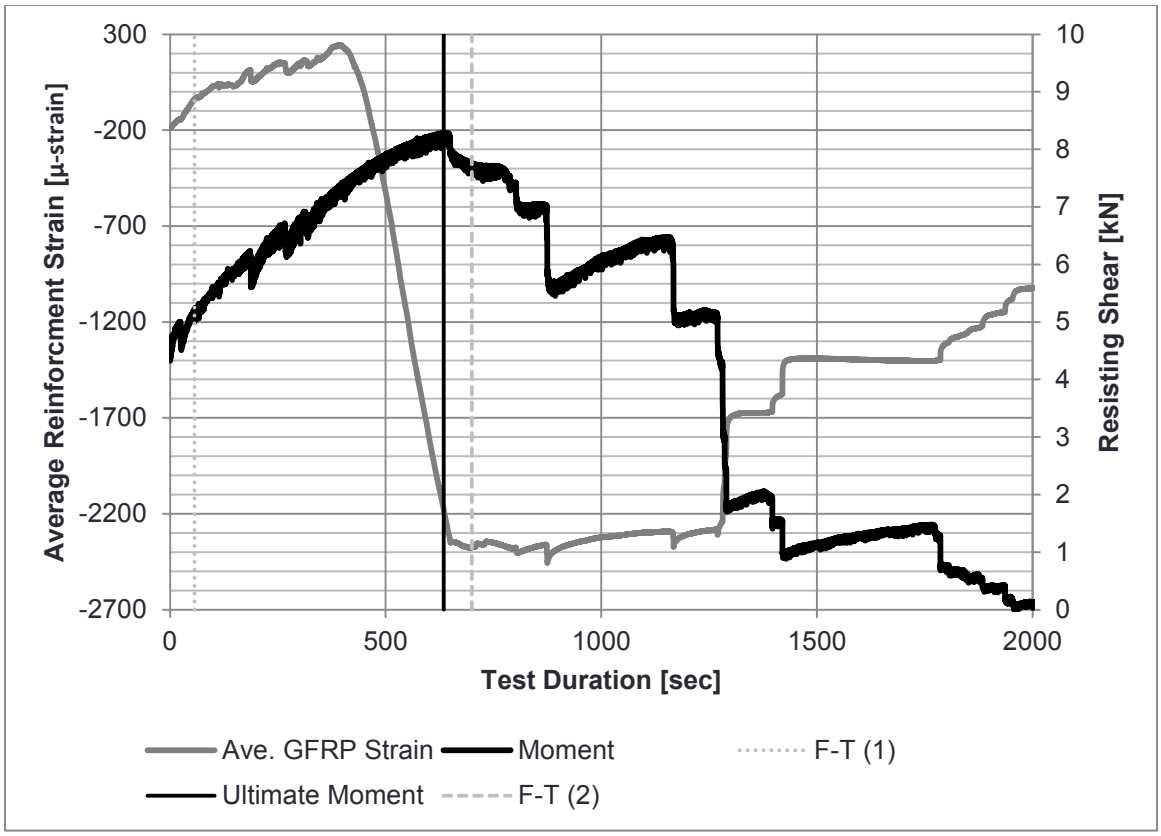

Figure 70: IIIb-1 testing events

4.2.3.2 IIIb-2 Results

During the load building phase of the IIIb-2 specimen, the beam first exhibits flexural-tension cracking beneath the left loading point. This crack widens as the loading reaches and ultimate shear force of 14.3 kN (3.21 kip). Immediately after the ultimate load is achieved, additional flexural cracking occurs, along with a sharp drop in the force resistance. The additional crack formations join with the initial cracking near the mid-height of the beam as shown in Figure 71. Figure 72 shows the stepping load-shedding period.

Figure 71: Type IIIb-2 specimen during loading

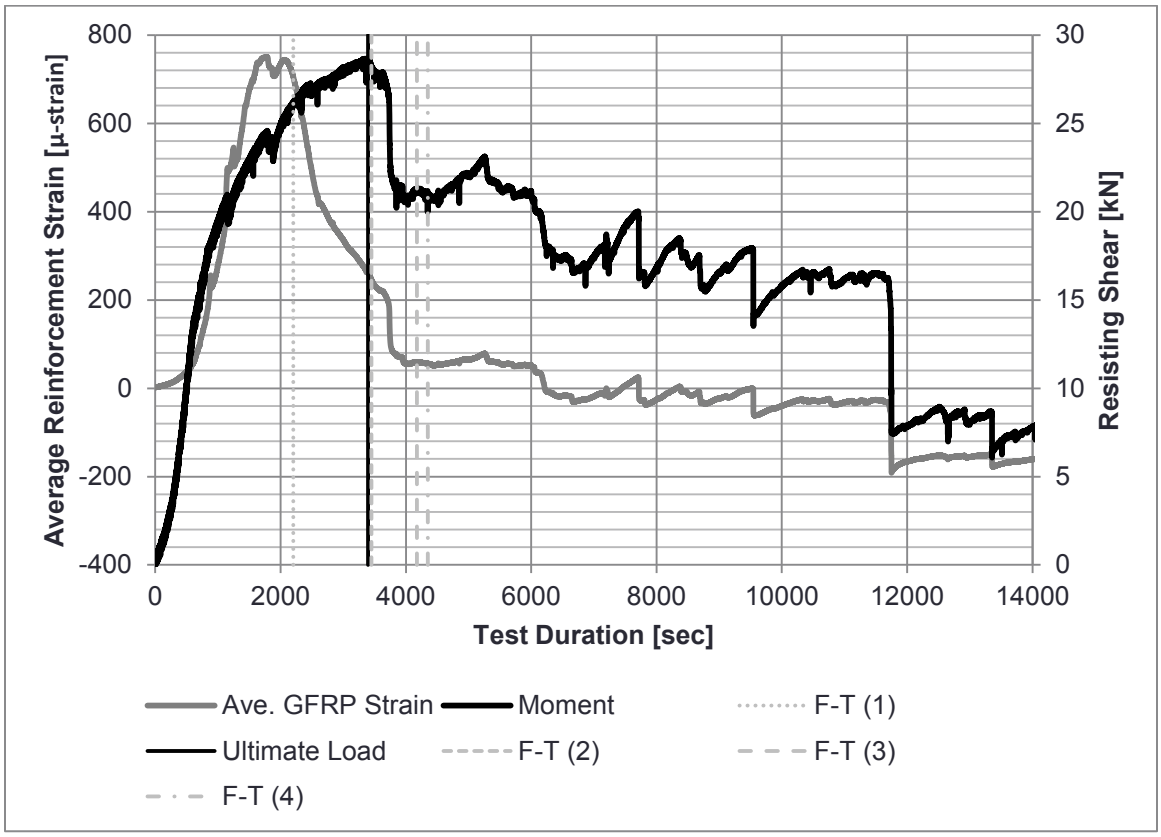

Figure 72: IIIb-2 testing events

4.2.3.3 Discussion

Despite being unreinforced for shear failure, the general failure mode of the beams appeared to be from flexural-tension forces. In both specimens the failures were located under the left loading point. This behavior is thought to be caused from the freedom of deflection allowed by the conceptual design of the flexural reinforcement.

The short waveform pattern allowed for early brittle failure in the concrete by being highly deformable in the axial direction, without applying large lateral constriction forces into the concrete. The resistance of the concrete matrix to this lateral constriction force is essential for adequate functionality of the concept. Changes in the design parameters of this concept – particularly the wavelength of the cords – would be necessary for an effective evaluation of this reinforcement for its shear force resistance properties.

4.3 Deflection Behavior

Data collected from the mid-span deflection is used to determine stiffness characteristics of the specimens. The stiffness of the specimens reflects the serviceability potential of the beam. A complete collection of the data durived from each specimen is shown in Appendix C. Data collected from the IIa series of specimens are observed to be the most relevant since the type IIb are not suited to represent flexural-tensile behavior, and the prototype design of the type III reinforcement proved to be insufficient for accurate concept representation.

Although tensile rupture was not achieved by the IIa series beams, general stiffness behaviors leading up to the ultimate strength of the beam before the flexural-compression failure is used to compare with the stiffness of the straight-rod Ia-2 control specimen. The chart in Figure 73 shows the deflection behavior of the IIa beam specimens with respect to the resisting moment. The behavior of the Ia-2 control specimen is also plotted in this chart for comparison. A linear trend line is matched to each of the specimens which represent the cumulative stiffness of each beam. The equations displayed in Figure 73 indicate that the two IIa specimens exhibited high stiffness than the control.

Another comparison of the specimen stiffness is shown in Figure 74 where the instantaneous stiffness taken at the ultimate moment of the IIa specimen and the Ia-2 control specimen. These values are calculated by dividing the mid-span deflection value at the ultimate moment, with the total applied load to the beam which supplied the ultimate moment. This comparison also exhibits higher stiffness values for both IIa specimens.

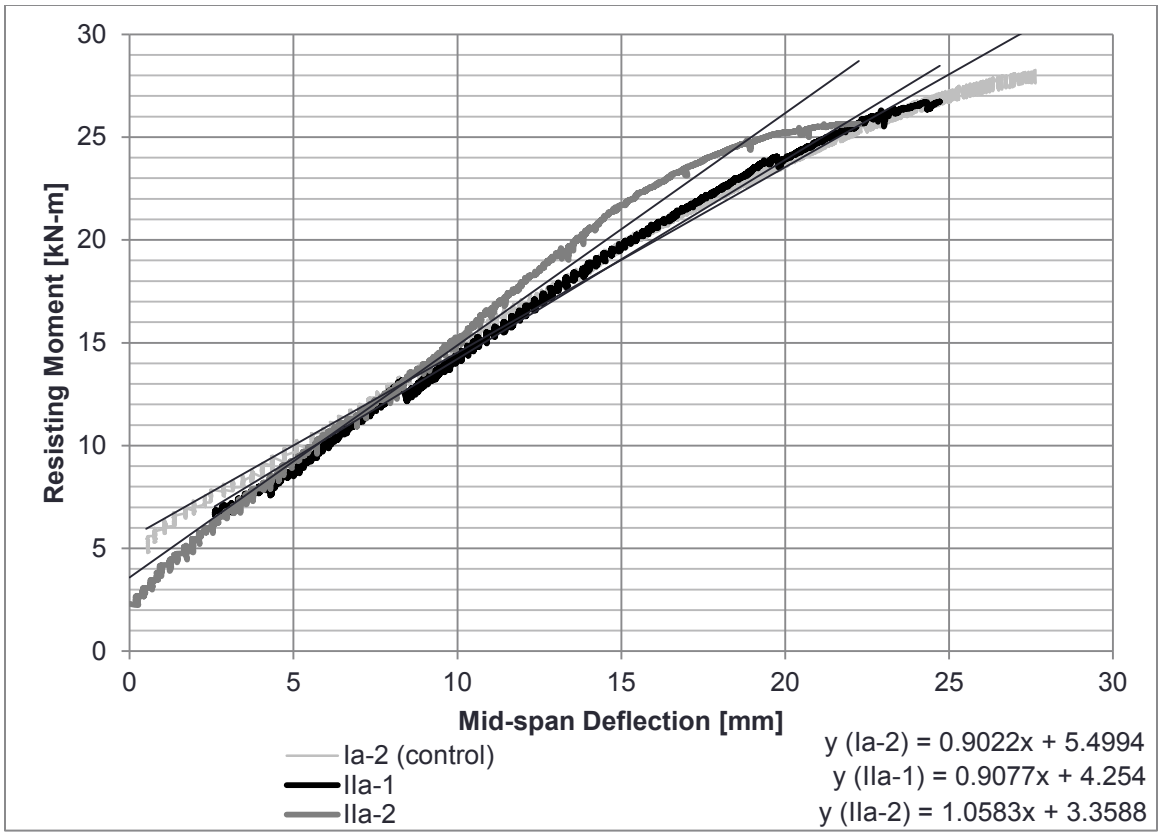

Figure 73: IIa beam deflections

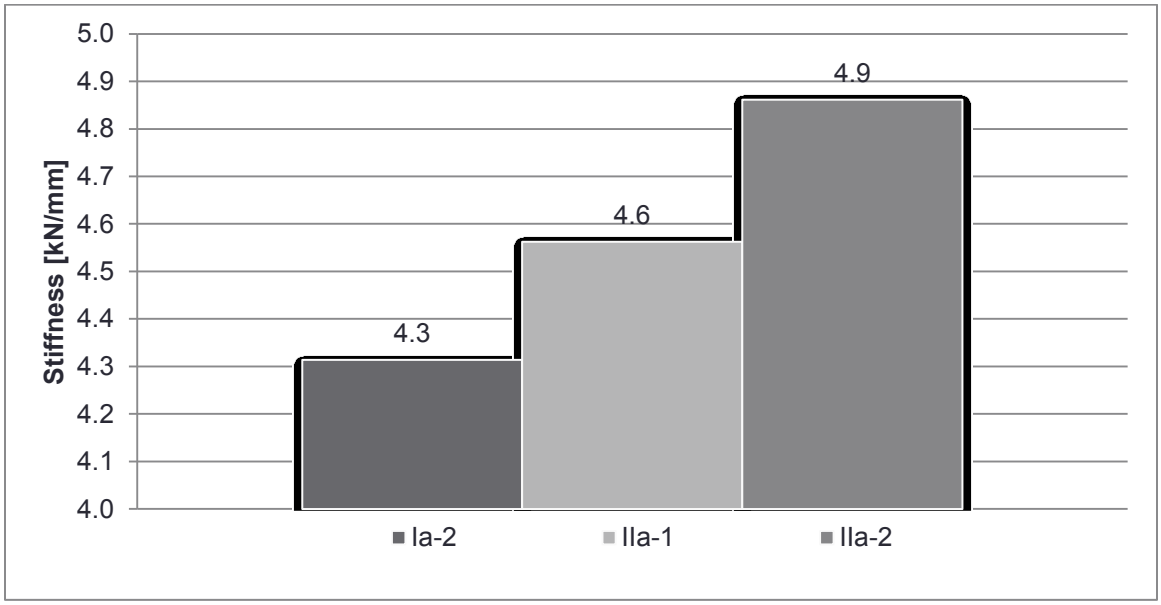

Figure 74: Comparison of beam stiffness at ultimate load

4.4 Section Analysis of Helical Reinforced Beam with Stirrups

Indications of the constrictive behavior proposed in the reinforcement system concept developed the form of atypical surface cracking parallel to the flexural reinforcement for the type IIa beam specimens as shown in Figure 75. It was thought that the constrictive action of the type II reinforcement created tensile regions in the concrete matrix outside of the constriction zones. This evidence warranted further internal investigation of the damaged beam in order to confirm the origins of the cracking.

Figure 75: Surface constrictive cracking in IIa-1 (left: side view, right: bottom view)

The specimen is cut in six different locations indicated by the diagram in Figure 76. The six cuts created ten internal cross-section faces.[4] The locations of the cuts were chosen to isolate the following areas of damage:

- Debonding of flexural reinforcement – [A.1, A.2, F.1, F.2]

  Debonding damage (such as what occurred with the type Ib beam specimens) would typically be located at the beam ends due to relatively smaller development length.

- Shear cracking – [B.1, B.2, E.1, E.2]

  Although reinforced hear cracking

- Constrictive action – [C, D]

The cross-section faces are ground flat in order to more clearly show deep cracking and eliminate insignificant surface flaws. The faces were individually photographed. A diagram showing the cut

[4] Concrete between the C and D cuts was discarded after being destroyed from testing damage in conjunction with the beam slicing process.

locations and face orientation with respect to the beam is shown in Figure 76. The entire collection of the cross-section images can be found in Appendix D.

No apparent cracking was observed from the sections cut at the ends of the beam (A.1, A.2, F.1, F.2). This result confirms that no debonding effects were present in this specimen at the beam ends. The intermediate sections cut in the shear damage regions of the beam (B.1, B.2, E.1, E.2) contained horizontal cracking across the face of the cross-section. These cracks were observed to be from shear failures and did not indicate any unique interaction with the flexural reinforcement.

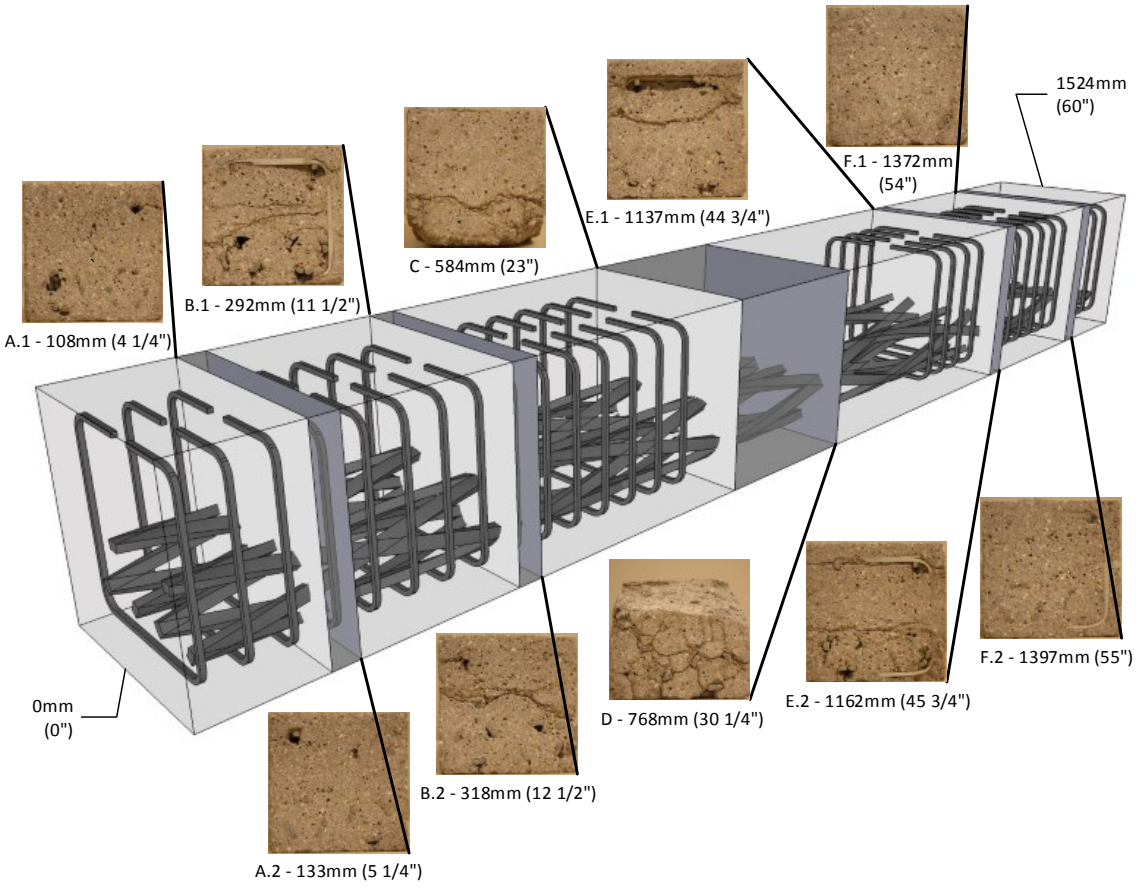

Figure 76: Specimen IIa-1 section cut diagram

The two cross-sectional faces near the mid-span of the beam (C, D) exhibited indications of damage around the constrictive zone of the reinforcement. The section C cut at approximately 584 mm (23 in) from the end of the beam is shown in Figure 77. The cracking pattern and reinforcement locations are highlighted for visibility. Cracking patterns at the right reinforcing unit are concentric with the reinforcement cross-section and extend to the side faces of the beam. The surface cracks on the side

faces of the beam are the previously mentioned atypical cracks. This indicates that the reinforcement's kinetic action created tensile stress, pulling the concrete in the constriction zone away from its surrounding matrix.

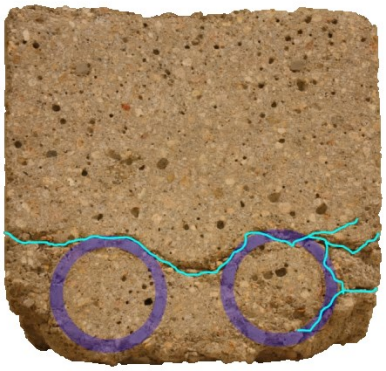

Figure 77: Section cut C

The section cut at the mid-span of the beam (D) also exhibited indications of constrictive reinforcement behavior. This section cut is shown in Figure 78. The highlighted cracking pattern shows concentric cracking around both reinforcement units, and exiting to the side and bottom faces of the beam.

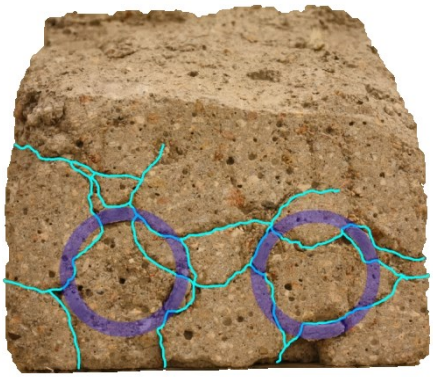

Figure 78: Section cut D (mid-span)

The results of the section analysis comply with the theoretical mechanics of the constrictive reinforcement design. Concentric cracking was only found near the mid-span of the beam where the highest internal moment forces (and subsequently the highest reinforcement tensile forces) are located in this loading configuration. Excellent bond strength, proposed by the reinforcement concept, is also indicated from this analysis due to the absence of cracking around the reinforcement at the beam ends.

4.5 Reinforcement Strain Analysis

The reinforcement strain data indicates the magnitude of loading being resisted by the GFRP reinforcement. The average of the upper and lower strain readings was taken to represent a total average strain experienced by the entire flexural reinforcement system at its mid-span cross-section. In order to determine if any of the concrete in the constrictive zone was contributing to tensile strength, the reinforcement strains in various specimens are compared to the loading resisted by the beam.

Since it was determined that the concept design of the type III specimens was not successful, the type II reinforcement specimens are used for this analysis. The tensile properties of the reinforcement are desired, so only the shear reinforced specimens are considered. Figure 79 plots the function of applied load with respect to average reinforcement load in order to demonstrate this property.

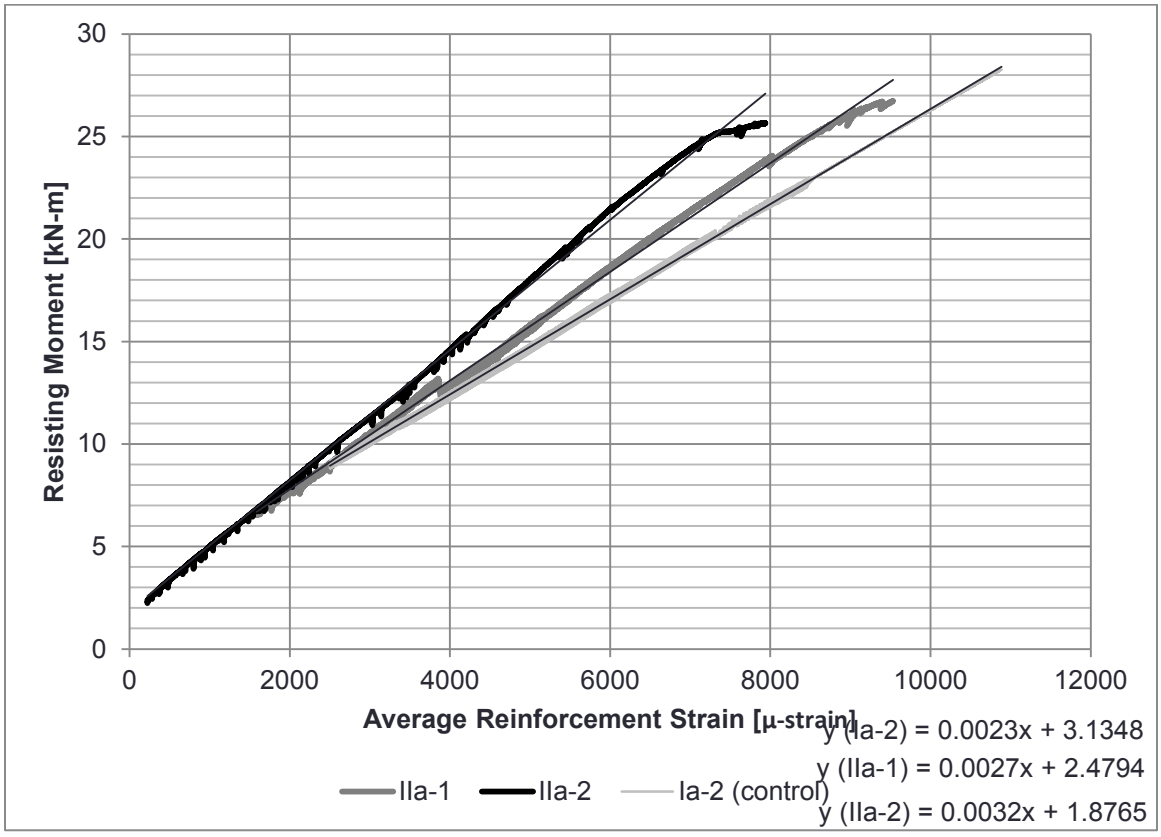

Figure 79: IIa reinforcement elastic modulus index

The linear trend of these load-strain curves provide and quantitative representation of the relationship between these specimens. It can be noted that the two type II specimens exhibit steeper

curves, meaning that less strain is experience by the GFRP, while more loading is being resisted by the entire beam system. This behavior supports the concept of the constrictive reinforcement properties.

4.6 Comparative Analysis

The data collected from the experimental testing was consolidated in order to perform a comparative analysis to determine the relative performance of each variation of the concept reinforcement. This section is intended to show any direct effect experienced by the specimens reinforced with the concept GFRP systems.

4.6.1 Ultimate Moment

Table 13 shows the ultimate resisting moment achieved by the specimens reinforced for shear. The ultimate resisting moment is the highest maximum moment calculated from the loading data before the specimen exhibited complete collapse or extreme deflection that would exceed serviceability requirements.

Table 13: Ultimate moment comparison of specimens reinforced with stirrups

Specimen ID	Failure Mode	f'c		Ultimate Applied Load		Ultimate Moment (M_u)	
		[Mpa]	[psi]	[kN]	[kip]	[kN-m]	[kip-ft]
Ia-1	F-C	27.19	3943	122.0	27.43	28.93	21.335
Ia-2	F-T	27.19	3943	119.2	26.80	28.26	20.848
IIa-1	F-C	23.24	3371	112.8	25.35	26.73	19.717
IIa-2	F-C	23.24	3371	108.2	24.32	25.65	18.916
IIIa-1	F-T	22.18	3217	24.94	5.606	5.912	4.360
IIIa-2	F-T	22.18	3217	47.95	10.78	11.37	8.385

Figure 80 shows the relative magnitude of the ultimate flexural strength values. From this comparison it can be noted that the Ia-1 control specimen achieved the highest ultimate moment. This however is not regarded as an accurate representation of the tensile behavior of the reinforcement since the specimen failed by concrete compression (F-C). Because the beam failed in this manner, accurate information on the behavior of this reinforcement can only be observed to the point that the concrete began to fail. Section 4.1.1.1 describes the concrete crushing behavior happening the ultimate strength is achieved.

Ia-2, the replicate of the control specimen Ia-1, demonstrated the second highest flexural strength. This value is valid for evaluating the flexural performance of the reinforcement since the observed failure mode was from tensile rupture of the reinforcement.

The specimens of the IIa variation showed good agreement in ultimate moment values. However, this result does not serve as a reliable comparison to the control specimens for evaluation of the type IIa reinforcement's capacity since the failure for both of these specimens were observed to be from concrete compression. Complete tensile rupture, as shown by specimen Ia-2, is needed in order to isolate adequate tensile reinforcement behavior. When considering the varying compressive strength of the concrete, it should be noted that the compressive strength of the type Ia specimens are 3.95 MPa stronger than the IIa specimens. Therefore, the relatively weaker concrete strength in the IIa specimens is likely responsible for the lower ultimate moment results of the specimens.

When applying the actual concrete compressive strength values to the design calculation to determine a projected flexural capacity the resulting flexural strengths are 9.15 kip-ft for the type Ia and 8.65 kip-ft for the type IIa. The type Ia specimen has a capacity of 5.83% greater than the type IIa. This value is relatively close to the percent change 9.19% determined in the experimental testing, supporting the proposed influence of the concrete compressive strength.

The ultimate load values of the type III reinforcements are clearly much lower that either the Ia or IIa series specimens. It is believed that this is a result of using low-wavelength geometry. After initial beam cracking, high axial deformation of the reinforcement has been observed to create heavy localized damage around the GFRP cords. This leads ineffective tensile action of this reinforcement variety.

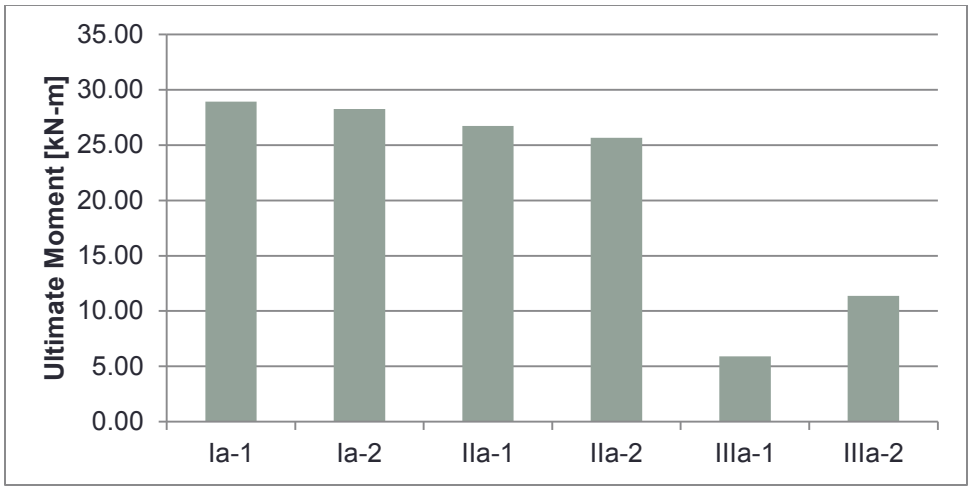

Figure 80: Ultimate moment force in specimens with shear stirrups

4.6.2 Ultimate Shear

Table 14 shows the ultimate shear resistance achieved by the specimens not reinforced for shear. The ultimate shear resistance is the highest maximum shear force calculated from the loading data before the specimen exhibited complete collapse or extreme deflection that would exceed serviceability requirements.

Table 14: Ultimate shear force comparison of specimens not reinforced with stirrups

Specimen ID	Failure Mode	f'c		Ultimate Applied Load		Ultimate Shear (Vu)	
		[Mpa]	[psi]	[kN]	[kip]	[kN]	[kip]
Ib-1	Sh	29.84	4327	70.10	15.76	35.05	7.880
Ib-2	Sh	27.19	3943	61.03	13.72	30.51	6.860
IIb-1	Sh/F-T	29.84	4327	88.34	19.86	44.17	9.930
IIb-2	Sh/F-T	23.24	3371	54.00	12.14	27.00	6.070
IIIb-1	F-T	22.18	3217	37.28	8.380	18.64	4.190
IIIb-2	F-T	29.84	4327	28.69	6.449	14.34	3.225

Figure 81 demonstrates the relative magnitude of the ultimate shear strength values. This data indicates that reasonable agreement in shear strength was achieved between the two control specimens (Ib-1 and Ib-2). The observed failures of these specimens demonstrated debonding of the flexural reinforcement, which according to the literature review is a realistic scenario for GFRP failure. This provides a good control value for which to compare the other specimen's shear performance with.

A close grouping of ultimate shear strength values was not achieved with the two type IIb specimens. This is possibly due to the difference of the concrete compressive strength being 6.6 MPa

between the two IIb specimens. This value partially affects the shear strength of the concrete, and therefore suggests that the effect of concrete contribution to shear strength may have played a large role in the different ultimate shear strengths between the two specimens. However one of the control specimens (Ib-1) and the IIb-1 specimens were cast with the same batch of concrete. When comparing the results of these two specimens, there is good indication of substantial shear strength gain in the IIb-2 specimen with an ultimate loading of 9.12 kN greater than the control specimen of the same concrete strength.

The specimens of the IIIb group exhibited a relatively closer agreement than the IIb group. Much like the IIIa specimens very low ultimate strength was exhibited. The observed failure modes of these specimens appeared very similar to the flexural failures of the shear reinforced specimens of group IIIa. Little if any shear type behavior is reflected in these ultimate strength values.

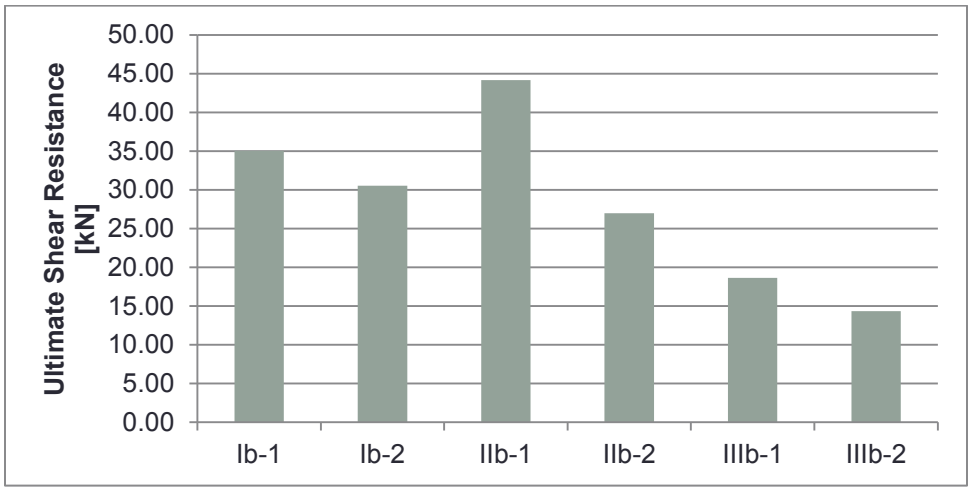

Figure 81: Ultimate shear force in specimens without shear stirrups

4.6.3 Strain at Ultimate Loading

Table 15 indicates the calculated average reinforcement stress at the time that the ultimate moment was reached in the specimens with shear stirrups. Data collected by the strain gauges attached to the reinforcement was used to determine these values. The strain values were applied to the known elastic modulus values from the GFRP sample coupon testing in order to determine an average reinforcement stress at ultimate loading.

At higher applied loads several strain gauges failed; likely due to the deformation of the concrete that their wires passed through. Using data approaching the failure, an equation was fitted to relate the

applied loading to the known corresponding shear. These equations were then used to extrapolate the data needed to develop an estimate of the reinforcement strain at the ultimate loading point. These extrapolated figures are noted in Table 15.

Table 15: Ultimate reinforcement stress

Specimen ID	Failure Mode	Ultimate Applied Load		Strain at Ultimate Load	Reinforcement Stress (fy)	
		[kN]	[kip]	[μ-strain]	[kPa]	[psi]
Ia-1	F-C	122.0	27.43	11229**	454.0	65.85
Ia-2	F-T	119.2	26.80	12667**	512.1	74.28
IIa-1	F-C	112.8	25.35	12658**	511.8	74.23
IIa-2	F-C	108.2	24.32	10456**	422.8	61.32
IIIa-1	F-T	24.94	5.606	594.69	24.04	3.487
IIIa-2	F-T	47.95	10.78	3420.2	138.3	20.06

***Strain values extrapolated*

The relative magnitude of the average reinforcement stress values from the specimens is shown in Figure 82. It can be noted from this figure that the stresses measured during the ultimate loading of the specimen Ia-1 is 58.1 kPa less than the specimen Ia-2. The greatest difference between these specimens is the failure mode in which the Ia-1 failed by concrete compression, and the Ia-2 failed by tensile rupture. This agrees with the lower stress value for the Ia-1 specimen since the concrete failed before rupture strains could develop in the reinforcement.

An significant difference in the reinforcement stress values was observed in the IIa specimen group as well. The varying data is thought to be due to variability in the quality of concrete since both beams failed in concrete crushing modes. While both of the specimens were cast in the same pour, the possibility of voids or flaws in the compressive zone of the beam exists. Since none of the IIb specimens achieved tensile rupture, significant comparison of reinforcement stress cannot be made.

Very low stresses were read at the ultimate strength of the IIIa series specimens. This is believed to be owed to the concrete of the beam primarily resisting the tensile forces developed from flexural bending. This behavior is insufficient for concrete reinforcement and cannot be usefully compared to the other reinforcement systems under its current design.

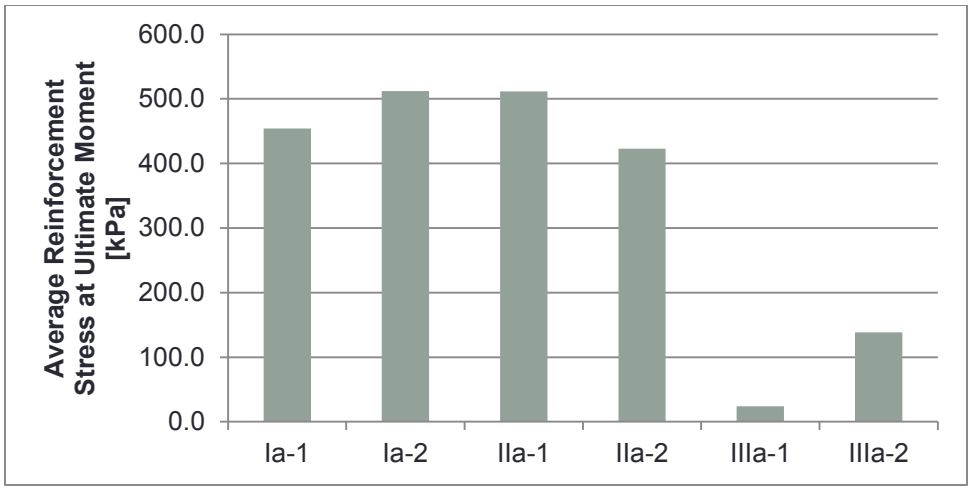

Figure 82: Average reinforcement of specimens with shear stirrups

4.6.4 Deflection at Ultimate Loading

Table 16 shows the calculated beam stiffness of each specimen at the time that the ultimate loading was reached. These values were developed from the ultimate load data and the corresponding beam deflection measure at the time of the ultimate load. This assessment is used to indicate the suitability of the reinforcement systems to address serviceability requirements.

Figure 83 shows the relative magnitudes of the specimens reinforced with shear stirrups. The control specimen Ia-1 indicates the highest of the beam stiffness with the Ia-2 specimen indicating 1.014 kN/mm below it. Such a wide spread could be attributed to the differing failure modes between these control specimens.

The IIa specimen group is in good agreement with one another and indicates only a marginal gain in stiffness when compared to the Ia-2 control specimen alone. However, due to the close grouping of the IIa values with the Ia-2 control, no significant trend can be shown from the beam stiffness with the use of the IIa specimen configuration.

Table 16: Beam stiffness at ultimate load

Specimen ID	Ultimate Applied Load		Deflection at Ultimate Load		Stiffness at Ultimate Load	
	[kN]	[kip]	[mm]	[in]	[kN/mm]	[kip/in]
Ia-1	122.0	27.43	22.78	0.8970	5.355	30.58
Ia-2	119.2	26.80	27.64	1.088	4.314	24.64
IIa-1	112.8	25.35	24.71	0.9730	4.563	26.05
IIa-2	108.2	24.32	22.25	0.8760	4.862	27.76
IIIa-1	24.94	5.606	13.59	0.5350	1.835	10.48
IIIa-2	47.95	10.78	15.90	0.6260	3.016	17.22
Ib-1	70.10	15.76	11.91	0.4690	5.885	33.60
Ib-2	61.03	13.72	10.34	0.4070	5.904	33.71
IIb-1	88.34	19.86	18.87	0.7430	4.681	26.73
IIb-2	54.00	12.14	8.763	0.3450	6.162	35.19
IIIb-1	37.28	8.380	13.44	0.5290	2.774	15.84
IIIb-2	28.69	6.449	6.909	0.2720	4.152	23.71

Large deflections are likely accountable for the low beam stiffness exhibited by the IIIa group of beam specimens. This reinforcement type allowed for large crack openings and localized concrete damage around the reinforcement cords before significant tensile load was taken by the GFRP. This specimen group did not provide sufficient stiffness to be compared to the others for its reinforcement contribution. The beam stiffness data produced by the control specimens for the Ib control specimens are in very good agreement, and provide a sufficient baseline value for shear failure of the specimen beams.

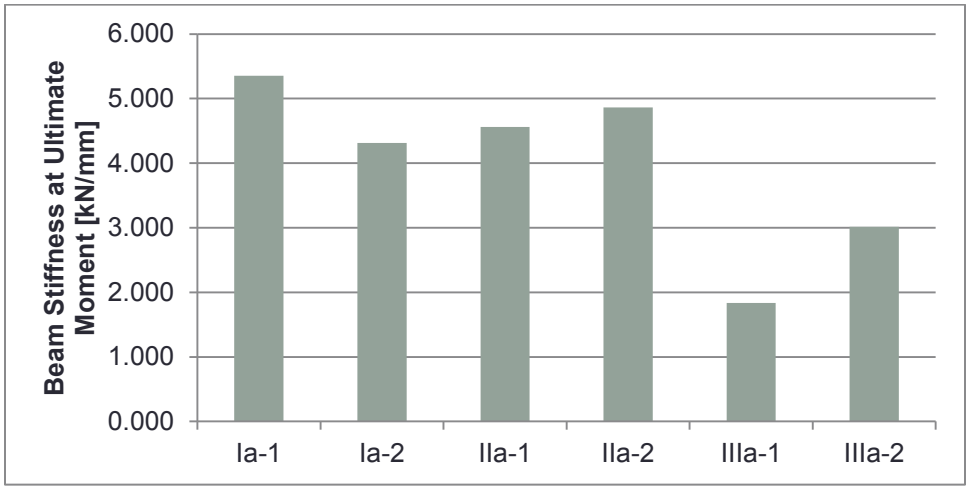

Figure 83: Beam stiffness of specimens with shear stirrups

The remaining specimens of both group IIb and IIIb do not show such a close agreement with their respective kind. While the specimen IIb-2 does indicate a slight increase in stiffness, it does not provide sufficient evidence of repeated behavior, and is not significant enough to determine if this increase is from the reinforcement alone.

As with the shear reinforced specimens, the IIIb specimen group exhibits significantly lower stiffness than the other specimen groups in its shear reinforcement category. This is believed to occur for the same reasons given for the shear reinforced specimens previously described, and cannot be reliably compared to the other specimen groups.

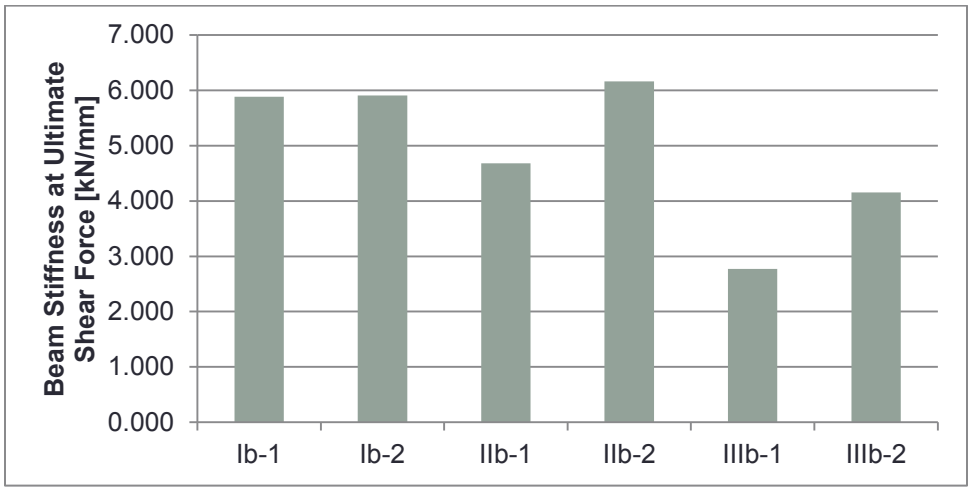

Figure 84: Beam stiffness of specimens without shear stirrups

Chapter 5

Conclusion and Recommendations

The exploration of innovative reinforced concrete concepts is important for the future development of affordable, safe, and durable structures for the future of the US transportation system. Technological advances in materials science, design principals, and construction methods must be continually implemented and adapted into common design procedures in order to avoid the high levels of deficiencies and required rehabilitation cost that are currently plaguing the transportation infrastructure with increasing urgency. This thesis has explored the use of FRP concrete reinforcements in novel configurations with the primary objective of enhancing structural traits and characteristics of the reinforcing material.

5.1 Conclusion

From the results of the experimental program presented herein, it is concluded that the concept reinforcement provided some indications of advantages over conventional GFRP reinforcing bars. Faults were also identified in the concept design which helped identify controlling parameters of the reinforcement system. Key findings are summarized as follows:

- Effects of the proposed mechanical constrictive properties of the type II (helical) reinforcements were observed in the specimens reinforced for shear by the presence of horizontal surface cracks propagating from outward from the mid-span of the group IIa beams. These effects were further investigated and observed through a section-analysis process which identified concentrically formed cracking patterns around the reinforcement as described in section 4.4.
- Qualitative evidence of shear resistance contribution was observed in the group IIb beams from the diversion of shear cracking away from the flexural reinforcement, to the end faces of the beams. It is unclear if the shear force resistance was contributed from

the constrictive action creating improved interaction mechanics or variable fiber orientation of the proposed reinforcing system.

- Evidence of increased pull-out strength of the type II (helical) reinforcement has been observed by the comparison of the failure mode of the Ib control group which both exhibited debonding failures and the IIb specimen group which exhibited good bond under similar conditions.
- While indications of an effective reinforcement system were found, further investigation would be required in order to establish quantitative evidence of advantage gained by the reinforcement system. Without more consistent data supporting the proof of concept, the structural improvements of the presented specimen test could be incongruous with typical behavior.

5.2 Contributions

The primary goals of this research were to provide an evaluation of the structural adequacy of the presented concept reinforcement system and to form a groundwork for which further development of alternative reinforcements can be built. This objective was achieved by showing close correlation of structural traits between the concept reinforcement specimens and the controls that represent conventional reinforcement. The later was achieved with the following key developments that were discovered through this research:

- Good indications of shear contribution of the helical (II) reinforcement provide the potential for significant reduction or possible omission of shear reinforcement components with further study and optimization of the concept design.
- Effects of geometric parameters were determined from the experimental testing. Primarily the variation of wavelength configurations indicated that relatively longer wavelengths provide constrictive action while still maintaining adequate tensile strength. This was indicated by the relatively poor performance of the type III (wave) reinforcements which exhibited low flexural and shear strength with high deflection and observed damage.

- The helical configuration provides adequate performance with less complex fabrication needs. As indicated in the methods section of this thesis, the wave type (III) reinforcement involved a more complex fabrication process than the helical type (II). Unless design improvements or fabrications techniques can simplify this, it is not likely to develop into a feasible alternative reinforcement.

5.3 Recommendations for Future Research

This thesis establishes a background for the exploration of alternative reinforcement geometries. Future contributions can refine and advance the development of the concept reinforcement into a reliably functioning alternative reinforcement. Suggested future contributions include:

- Continued experimental testing addressing the controlling design parameters established in this research and exploring various other loading configurations can be further investigated in order to identify common behaviors of the concept reinforcement system. More conclusive evidence than what was presented in this research is needed for constrictive reinforcements.
- Analytical modeling of the concept reinforcement systems could be performed in order to analyze the concrete-reinforcement interaction behaviors and determine the effect of geometric and material property parameters. Geometric parameter variations in dimensions such as constrictive zone volume, strand count, or wavelength could be manipulated in order to observe the stress distribution that occurs from the reacting concrete matrix. Manipulation of the material properties of both the reinforcement (carbon or aramid) and concrete matrix (ultra-high strength or fiber reinforced) could also observed in order to determine their effect on interaction properties.
- Design optimization could be performed using additional experimental testing and analytical modeling in order to refine the performance of the concept reinforcement.
- This study is intended to evaluate the concept reinforcement for transportation structure applications. However, further exploration of other structural applications can be performed in order to identify suitable uses for the concept reinforcement which

capitalizes on the system's characteristics. Additional applications to explore include, but are not limited to: buildings, seismic resistance, blast protection, or nuclear containment facilities.

- Further investigation of the mechanical interactions on the mezzo-scale of the concrete in the constriction zones of the reinforcement should be investigated in order to effectively manipulate this property of the concept reinforcement.
- Cost estimate studies must be conducted to determine the feasibility and potential savings of the concept reinforcement. While studies have shown the long-term benefits of using GFRP reinforcement, the controlling parameters (e.g. manufacturing cost and transportation) may cause a shift in feasibility relative to conventional GFRP bars.

Bibliography

1. ACI Committee 318. (2011). *ACI 318-11 Building Code Requirements for Structural Concrete*.
2. ACI Committee 440. (2006). *ACI 440.1R-06 Guide for the Design and Construction of Structural Concrete Reinforced with FRP Bars Reported by ACI Committee*.
3. Ahmed, E. A., El-Salakawy, E. F., & Benmokrane, B. (2010). Shear Performance of RC Bridge Girders Reinforced with Carbon FRP Stirrups. *Journal of Bridge Engineering*, *15*(1), 44–54. doi:10.1061/(ASCE)BE.1943-5592.0000035
4. American Association of State Highway and Transportation Officials. (2006). *AASHTO LRFD Bridge Design Specifications* (4th ed.). Washington DC.
5. American Society for Testing and Materials. (2012). *Standard Test Method for Tensile Properties of Fiber Reinforced Polymer Matrix Composite Bars* (Vol. i, pp. 1–13). doi:10.1520/D7205
6. Ayranci, C., & Carey, J. P. (2010). Effect of Diameter in Predicting the Elastic Properties of 2D Braided Tubular Composites. *Journal of Composite Materials*, *44*(16), 2031–2044. doi:10.1177/0021998310369599
7. Bischoff, P. H., & Gross, S. P. (2011). Design Approach for Calculating Deflection of FRP-Reinforced Concrete. *Journal of Composites for Construction*, *318*(August), 490–499. doi:10.1061/(ASCE)CC.1943-5614.0000195.
8. El-Salakawy, E., Benmokrane, B., El-Ragaby, A., & Nadeau, D. (2005). Field Investigation on the First Bridge Deck Slab Reinforced with Glass FRP Bars Constructed in Canada. *Journal of Composites for Construction*, *9*(6), 470–479. doi:10.1061/(ASCE)1090-0268(2005)9:6(470)
9. Etman, E. E. (2011). Innovative Hybrid Reinforcement for Flexural Members. *Journal of Composites for Construction*, *15*(1), 2–8. doi:10.1061/(ASCE)CC.1943-5614.0000145
10. Harajli, M., & Abouniaj, M. (2010). Bond Performance of GFRP Bars in Tension: Experimental Evaluation and Assessment of ACI 440 Guidelines. *Journal of Composites for Construction*, *14*(6), 659–668. doi:10.1061/(ASCE)CC.1943-5614.0000139

11. Harris, H. G., Somboonsong, W., & Ko, F. K. (1998). New Ductile Hybrid FRP Reinforcing Bar for Concrete Structures. *Journal of Composites for Construction*, (February), 28–37.
12. Harte, A.-M., & Fleck, N. A. (2000). On the Mechanics of Braided Composites in Tension. *European Journal of Mechanics A/Solids*, *19*(2), 259–275. Retrieved from http://linkinghub.elsevier.com/retrieve/pii/S0997753899001643
13. Kassem, C., Farghaly, A. S., & Benmokrane, B. (2011). Evaluation of Flexural Behavior and Serviceability Performance of Concrete Beams Reinforced with FRP Bars. *Journal of Composites for Construction*, *15*(5), 682–695. doi:10.1061/(ASCE)CC.1943-5614.0000216
14. Katz, A. (2004). Environmental Impact of Steel and Fiber-Reinforced Polymer Reinforced Pavements. *Journal of Composites for Construction*, (December), 481–488. doi:10.1061/(ASCE)1090-0268(2004)8:6(481)
15. Kleinstreuer, C., Li, Z., Basciano, C. A., Seelecke, S., & Farber, M. A. (2008). Computational Mechanics of Nitinol Stent Grafts. *Journal of Biomechanics*, *41*(11), 2370–8. doi:10.1016/j.jbiomech.2008.05.032
16. Koch, G. H., Brongers, M. P. H., Thompson, N. G., Virmani, Y. P., & Payer, J. H. (2001). *Corrosion costs and preventive strategies in the United States*. Retrieved from https://www.corrdefense.com/Academia Government and Industry/05-Koch.pdf
17. Maitra, S. R., Reddy, K. S., & Ramachandra, L. S. (2010). Load Transfer Characteristics of Aggregate Interlocking in Concrete Pavement. *Journal of Transportation Engineering*, (March), 190–195. doi:10.1061/(ASCE)TE.1943-5436.114
18. Mazumdar, S. K. (2002). *Composites Manufacturing*. CRC Press.
19. Okelo, R., & Yuan, R. L. (2005). Bond Strength of Fiber Reinforced Polymer Rebars in Normal Strength Concrete. *Journal of Composites for Construction*, *9*(3), 203–213. doi:10.1061/(ASCE)1090-0268(2005)9:3(203)
20. Porter, M., & Harries, K. (2007). Prioritized FRP Research Needs in Civil Infrastructure. *Structural Engineering Research Frontiers*. Retrieved from http://ascelibrary.org/doi/abs/10.1061/40944(249)54

Appendix A – Specimen Design Calculations

Type I

FRP Rod Reinforced Concrete Beam

Input values & definitions

Beam Dimensions

$L := 178in$ — span length

$h := 24in$ — beam height

$b := 24in$ — beam width

Scaling

$N := \frac{1}{3}$ — model scale factor

Reinforcement

$dc := 2in$ — clear cover distance (AASHTO 5.12.3)

Flexure

$n := 4$ — number of flexure bars per row

$nr := 3$ — number of rows

$sv := 1in$ — veritcal clear spacing

$bt := 3 \cdot 0.22in = 0.66 \cdot in$ — bar thickness

Shear

$vt := 3 \cdot 0.177in = 0.531 \cdot in$ — stirrup strand height

FRP Specifications

$CE := 0.8$ — environmental reduction factor - glass/not exposed [ACI-440.1a Table 7.1]

$FFU := 72 \cdot ksi$ — FRP tensile strength

$Ef := 5864 \cdot ksi$ — FRP modulus of elasticity

Concrete Specifications

$FC := 4000psi$ — concrete compressive strength

$\varepsilon cu := 0.003$ — concrete ultimate strain

$Dconc := 150 \cdot \frac{lbf}{ft^3}$ — density of concrete

$ca := 1.5in$ — maximum coarse aggregate

Flexure Design

$Am := bt^2 = 0.4356 \cdot in^2$ single flexure reinforcement bar area

$ffu := CE \cdot FFU = 57.6 \cdot ksi$ design tensile strength of FRP, considering reductions for service environment

$\beta 1 := if\left(FC \le 4 \cdot ksi, 0.85, if\left(FC < 8 \cdot ksi, -.05 \cdot \frac{FC}{ksi} + 0.95, 0.65\right)\right) = 0.85$

$\rho fb := 0.85 \cdot \frac{FC}{ffu} \cdot \beta 1 \cdot \frac{Ef \cdot \varepsilon cu}{Ef \cdot \varepsilon cu + ffu} = 0.0117$ balanced reinforcement ratio

$d := h - dc - vt - 1.5bt - sv = 19.479 \cdot in$ distance from extreme compression fiber to centroid of tension reinforcement

$At := Am \cdot n \cdot nr = 5.2272 \cdot in^2$ total reinforcement area

$\rho f := \frac{At}{b \cdot d} = 0.0112$ FRP reinforcement ratio

$Fmode := if(\rho f < \rho fb, "FRP\ rupture", "Concrete\ crushing")$

Failure Mode

$Fmode = "FRP\ rupture"$

$ff := \sqrt{\left(\frac{Ef \cdot \varepsilon cu}{4}\right)^2 + \frac{0.85 \cdot \beta 1 \cdot FC}{\rho f} \cdot Ef \cdot \varepsilon cu} - 0.5 \cdot Ef \cdot \varepsilon cu = 59.2065 \cdot ksi$ stress in FRP reinforcement in tension at concrete failure

$Mn := \rho f \cdot ff \cdot \left(1 - 0.59 \cdot \frac{\rho f \cdot ff}{FC}\right) \cdot b \cdot d^2 = 453.3159 \cdot kip \cdot ft$ nominal moment capacity

$\Phi f := if\left(\rho f \le \rho fb, 0.55, if\left(\rho f < 1.4\rho fb, 0.3 + 0.25\frac{\rho f}{\rho fb}, 0.65\right)\right) = 0.55$ flexural strength reduction factor

$\Phi f \cdot Mn = 249.3237 \cdot kip \cdot ft$ factored ultimate moment capacity

$P := \frac{3 \cdot \Phi f \cdot Mn}{L} = 50.425 \cdot kip$ factored ultimate load capacity

Shear Design

$Vu := P = 50.425 \cdot kip$ factored shear force at section

$\Phi v := 0.75$ strength reduction factor

$Ec := 57000psi \cdot \sqrt{\frac{FC}{psi}} = 3604.9965 \cdot ksi$ modulus of elasticity of concrete

$nf := \frac{Ef}{Ec} = 1.6266$ ratio of modulus of elasticity of FRP bars to modulus of elasticity of concrete

$k := \sqrt{2 \cdot \rho f \cdot nf + (\rho f \cdot nf)^2} - \rho f \cdot nf = 0.1734$ ratio of depth of neutral axis to reinforcement depth

$c := k \cdot d = 3.3777 \cdot in$ distance from extreme compression fiber to the neutral axis

$Vc := 5 \cdot \sqrt{\frac{FC}{psi}} psi \cdot b \cdot c = 25.6348 \cdot kip$ nominal shear strength provided by concrete

$Ts := if\left(Vu \le \Phi v \cdot \frac{Vc}{2}, "No\ Stirrups\ Reqd", "Stirrups\ Needed"\right)$

Stirrup Check

Ts = "Stirrups Needed"

$Av := vt^2 = 0.282 \cdot in^2$ cross-sectional area of single stirrup bar

$rb := 3 \cdot vt = 1.593 \cdot in$ internal radius of bend in FRP reinforcement

$ffb := \left(0.3 + 0.05 \cdot \frac{rb}{vt}\right) \cdot ffu = 25.92 \cdot ksi$ strength of bent portion of stirrup

$ffv := \min(ffb, 0.004 \cdot Ef) = 23.456 \cdot ksi$ tensile strength of stirrup

$smax := \min\left[\frac{2Av \cdot ffv}{50psi \cdot b}, \frac{\Phi v \cdot 2Av \cdot ffv \cdot d}{(Vu - \Phi v \cdot Vc)}, 24in, \frac{d}{2}\right] = 6.1939 \cdot in$ maximun stirrup spacing

$s := floor\left(\frac{1.5^{-1} smax}{in}\right) in = 4 \cdot in$ stirrup centroid spacing (modified for x1.5 reqd)

$x := Ceil\left(\frac{L \cdot \Phi v \cdot Vc}{4 \cdot Vu}, 0.25in\right) = 17 \cdot in$ cut-off distance from midpoint

$ltmin := 12 \cdot vt = 6.372 \cdot in$ minimum stirrup tail length

$nv := ceil\left(\frac{\frac{L}{2} - dc - x}{s + vt}\right) \cdot 2 = 32$ number of stirrups

$Vs := \frac{2Av \cdot ffv \cdot d}{s} = 64.4139 \cdot kip$ shear strength from stirrups (approximation based on ACI 318)

$Vn := Vs + Vc = 90.0487 \cdot kip$ nominal shear strength

$\Phi v \cdot Vn = 67.5366 \cdot kip$ factored shear strength

Shear Reinforcement Check

$TV := if(Vu \le \Phi v \cdot Vn, "Pass", "Fail")$

TV = "Pass"

$\frac{\Phi v \cdot Vn}{Vu} = 1.3393$

Developement Length

$$C := \min\left[dc + \frac{bt}{2}, \frac{1}{2}\cdot\frac{b - 2\cdot dc - n\cdot bt}{(n-1)}\right] = 2.33\cdot in$$ minimum spacing

$$\alpha := 1$$ bar location modification factor (all bars <12in from bottom of beam)

$$le := \frac{L}{2} = 89\cdot in$$ embedded length of reinforcing bar

$$db := \sqrt{\frac{4\cdot bt^2}{\pi}} = 0.7447\cdot in$$ equivalent bar diameter

$$ffe := \min\left[\frac{\sqrt{\frac{FC}{psi}}\,psi}{\alpha}\cdot\left(13.6\cdot\frac{le}{db} + \frac{C}{db}\cdot\frac{le}{db} + 340\right), ffu\right] = 57.6\cdot ksi$$ bar stress that can be developed for embedment length

$$ffr := \min(ff, ffe) = 57.6\cdot ksi$$ required bar stress

$$ld := \min\left[\frac{\alpha\cdot\left(\frac{ffr}{\sqrt{\frac{FC}{psi}}\cdot psi}\right) - 340}{13.6 + \frac{C}{db}}\cdot db, 1.3\cdot\frac{\Phi f\cdot Mn}{Vu}\right] = 25.4082\cdot in$$ developement length

$$Lb := L + 2in = 180\cdot in$$ beam length

$$Tl := if\left(ld \le \frac{Lb - 2dc}{2}, "Pass", "FAIL"\right)$$

Developement Length Check

Tl = "Pass"

Spatial Check

$$sp := Floor\left[\frac{[b - 2\cdot(dc + vt + rb) - n\cdot bt]}{(n-1)}, 0.125in\right] = 4.25\cdot in$$ flexure bar horizontal clear spacing

$$spmin := \max(1.5\cdot bt, 1.5ca, 1.5in) = 2.25\cdot in$$ minimum assembly spacing

$$spmax := \min(1.5\cdot h, 18in) = 18\cdot in$$ maximum assembly spacing

$$Ts := if(sp \ge spmin \wedge sp \le spmax, "Pass", "FAIL")$$

Flexure Bar Spacing Check

Ts = "Pass"

$$dmin := c + 1in + bt + \frac{sv}{2} = 5.5377\cdot in$$ minimum tensile region

$$Td := if(d \ge dmin, "Pass", "FAIL")$$

Tensile Region Check

Td = "Pass"

Type I - Prototype Summary

Dimensions:

$Lb = 15\,ft$ — beam length

$L = 178 \cdot in$ — span length

$b = 24 \cdot in$ — beam width

$h = 24 \cdot in$ — beam height

Reinforcement:

$dc = 2 \cdot in$ — clear cover

Flexure

$n = 4$ — number of bars per row

$nr = 3$ — number of rows

$bt = 0.66 \cdot in$ — bar thickness

$Am = 0.4356 \cdot in^2$ — flexure reinforcement bar area

$sp = 4.25 \cdot in$ — horizontal bar clear spacing

$sv = 1 \cdot in$ — vertical bar clear spacing

$At = 5.2272 \cdot in^2$ — total bar area

$d = 19.479 \cdot in$ — effective depth

Shear

$nv = 32$ — number of required stirrups

$vt = 0.531 \cdot in$ — stirrup strand thickness

$Av = 0.282 \cdot in^2$ — area of stirrup bar

$rb = 1.593 \cdot in$ — radius of stirrup bend

$ltmin = 6.372 \cdot in$ — legnth of stirrup tail beyond hook

$s = 4 \cdot in$ — stirrup centroid spacing

$x = 17 \cdot in$ — cut-off distance from midpoint

Loading:

$P = 50.425 \cdot kip$ — prototype load capacity

$M := \frac{P \cdot L}{3} = 249.3237 \cdot kip \cdot ft$ — prototype moment capacity

Type I - Model Summary

$N = 0.3333$ scale factor

Dimensions:

$Lb \cdot N = 5\,ft$ beam length

$L \cdot N = 59.3333 \cdot in$ span lenth

$b \cdot N = 8 \cdot in$ beam width

$h \cdot N = 8 \cdot in$ beam height

Reinforcement:

$dc \cdot N = 0.6667 \cdot in$ clear cover

Flexure

$n = 4$ number of bars per row

$nr = 3$ number of rows

$bt \cdot N = 0.22 \cdot in$ bar thickness

$Am \cdot N^2 = 0.0484 \cdot in^2$ flexure reinforcement bar area

$sp \cdot N = 1.4167 \cdot in$ horizontal bar clear spacing

$sv \cdot N = 0.3333 \cdot in$ vertical bar clear spacing

$At \cdot N^2 = 0.5808 \cdot in^2$ total bar area

$d \cdot N = 6.493 \cdot in$ effective depth

Shear

$nv = 32$ number of required stmups

$vt \cdot N = 0.177 \cdot in$ stirrup strand thickness

$Av \cdot N = 0.094 \cdot in^2$ area of stirrup bar

$rb \cdot N = 0.531 \cdot in$ radius of stirrup bend

$ltmin \cdot N = 2.124 \cdot in$ legnth of stirrup tail beyond hook

$s \cdot N = 1.3333 \cdot in$ stirrup centroid spacing

$x \cdot N = 5.6667 \cdot in$ cut-off distance from midpoint

Loading:

$P \cdot N^2 = 5.6028 \cdot kip$ model load capacity

$M \cdot N^3 = 9.2342\,ft \cdot kip$ model moment capacity

Type II

Intersecting Triple Helix FRP Reinforced Beam

Input values & definitions

Beam Dimensions

$L := 178in = 14.8333\,ft$ span length

$h := 25.5in$ beam height

$b := 24in$ beam width

Scaling

$N := \frac{1}{3}$ model scale factor

Reinforcement

$d_{cc} := 2in$ clear cover distance (AASHTO 5.12.3)

Flexure

$n_a := 2$ number of reinforcement assemblies

$n_s := 3$ number of strands per direction

$ID := 6in$ inside diameter of unit

$t_s := 1in$ strand thickness

$w_{si} := 1.19in$ inner width of strand

$\alpha := 10deg$ helic angle

Shear

$t_v := N^{-1} \cdot 0.177in = 0.531 \cdot in$ stirrup strand thickness

FRP Specifications

$CE := 0.8$ environmental reduction factor - glass/not exposed [ACI-440.1a Table 7.1]

$f_{Ft} := 72 \cdot ksi$ FRP tensile strength

$E_F := 5864 \cdot ksi$ FRP modulus of elasticity

Concrete Specifications

$f_C := 4000psi$ concrete compressive strength

$\varepsilon_{Cu} := 0.003$ concrete ultimate strain

$P_C := 150 \cdot \frac{lbf}{ft^3}$ density of concrete

$D_a := 1.5in$ maximum diameter of coarse aggregate

Flexure Design

$\theta := \frac{2 \cdot w_{si}}{ID} = 22.7273 \cdot deg$ single strand sweep angle

$OD := ID + 2t_s = 8 \cdot in$ outer diameter of unit

$A_m := 2 \cdot n_s \cdot \left[\frac{\theta}{2\pi} \left[\left(\frac{OD}{2} \right)^2 - \left(\frac{ID}{2} \right)^2 \right] \right] = 2.6515 \cdot in^2$ single unit cross-sectional area

$f_{Fu} := CE \cdot f_{Ft} = 57.6 \cdot ksi$ design tensile strength of FRP, considering reductions for service environment

$\beta_1 := if\left(f_C \le 4 \cdot ksi, 0.85, if\left(f_C < 8 \cdot ksi, -.05 \cdot \frac{f_C}{ksi} + 0.95, 0.65 \right) \right) = 0.85$

$\rho_{Fb} := 0.85 \cdot \frac{f_C}{f_{Fu}} \cdot \beta_1 \cdot \frac{E_F \cdot \varepsilon_{Cu}}{E_F \cdot \varepsilon_{Cu} + f_{Fu}} = 0.0117$ balanced reinforcement ratio

$d := h - d_{cc} - t_v - t_s - \frac{ID}{2} = 18.969 \cdot in$ distance from extreme compression fiber to centroid of tension reinforcement

$A_t := n_a \cdot A_m = 5.303 \cdot in^2$ total reinforcement area

$\rho_F := \frac{A_t}{b \cdot d} = 0.0116$ FRP reinforcement ratio

$Fmode := if(\rho_F < \rho_{Fb}, "FRP\ rupture", "Concrete\ crushing")$

Failure Mode

$Fmode = "FRP\ rupture"$

$f_{Fc} := \sqrt{\left(\frac{E_F \cdot \varepsilon_{Cu}}{4} \right)^2 + \frac{0.85 \cdot \beta_1 \cdot f_C}{\rho_F} \cdot E_F \cdot \varepsilon_{Cu}} - 0.5 \cdot E_F \cdot \varepsilon_{Cu} = 57.852 \cdot ksi$ stress in FRP reinforcement in tension at concrete failure

$M_n := \rho_F \cdot f_{Fc} \cdot \left(1 - 0.59 \cdot \frac{\rho_F \cdot f_{Fc}}{f_c} \right) \cdot b \cdot d^2 = 436.7567 \cdot kip \cdot ft$ nominal moment capacity

$\Phi_f := if\left(\rho_F \le \rho_{Fb}, 0.55, if\left(\rho_F < 1.4\rho_{Fb}, 0.3 + 0.25 \frac{\rho_F}{\rho_{Fb}}, 0.65 \right) \right) = 0.55$ flexural strength reduction factor

$\Phi_f M_n = 240.2162 \cdot kip \cdot ft$ factored ultimate moment capacity

$P := \frac{3 \cdot \Phi_f \cdot M_n}{L} = 48.5831 \cdot kip$ factored ultimate load capacity

Shear Design

$V_u := P = 48.5831 \cdot kip$ factored shear force at section

$\Phi_v := 0.75$ strength reduction factor

$E_C := 57000psi \cdot \sqrt{\frac{f_C}{psi}} = 3604.9965 \cdot ksi$ modulus of elasticity of concrete

$n_f := \frac{E_F}{E_C} = 1.6266$ ratio of modulus of elasticity of FRP bars to modulus of elasticity of concrete

$k := \sqrt{2 \cdot \rho_F \cdot n_f + (\rho_F \cdot n_f)^2} - \rho_F \cdot n_f = 0.1766$ ratio of depth of neutral axis to reinforcement depth

$c := k \cdot d = 3.3507 \cdot in$ distance from extreme compression fiber to the neutral axis

$V_C := 5 \cdot \sqrt{\frac{f_C}{psi}} psi \cdot b \cdot c = 25.4299 \cdot kip$ nominal shear strength provided by concrete

$Ts := if\left(V_u \le \Phi_v \cdot \frac{V_C}{2}, "No\ Stirrups\ Reqd", "Stirrups\ Needed"\right)$

Stirrup Check

Ts = "Stirrups Needed"

$A_v := t_v^2 = 0.282 \cdot in^2$ cross-sectional area of single stirrup bar

$n_b := 3 \cdot t_v = 1.593 \cdot in$ internal radius of bend in FRP reinforcement

$f_{Fb} := \left(0.3 + 0.05 \cdot \frac{n_b}{t_v}\right) \cdot f_{Fu} = 25.92 \cdot ksi$ strength of bent portion of stirrup

$f_{Fv} := \min(f_{Fb}, 0.004 \cdot E_F) = 23.456 \cdot ksi$ tensile strength of stirrup

$s_{vmax} := \min\left[\frac{2A_v \cdot f_{Fv}}{50psi \cdot b}, \frac{\Phi_v \cdot 2A_v \cdot f_{Fv} \cdot d}{(V_u - \Phi_v \cdot V_C)}, 24in, \frac{d}{2}\right] = 6.3768 \cdot in$ maximun stirrup spacing

$s_v := Floor\left(\frac{1.5^{-1} s_{vmax}}{in}, 0.125\right) in = 4.25 \cdot in$ stirrup centroid spacing (modified for x1.5 reqd)

$x := Ceil\left(\frac{L \cdot \Phi_v \cdot V_C}{4 \cdot V_u}, 0.25in\right) = 17.5 \cdot in$ cut-off distance from midpoint

$l_{tmin} := 12 \cdot t_v = 6.372 \cdot in$ minimum stirrup tail length

$n_v := ceil\left(\frac{\frac{L}{2} - d_{cc} - x}{s_v + t_v}\right) \cdot 2 = 30$ number of stirrups

$V_v := \frac{2A_v \cdot f_{Fv} \cdot d}{s_v} = 59.0376 \cdot kip$ shear strength from stirrups (approximation based on ACI 318)

$V_n := V_v + V_C = 84.4675 \cdot kip$ nominal shear strength

$\Phi_v \cdot V_n = 63.3506 \cdot kip$ factored shear strength

$TV := if(V_u \le \Phi_v \cdot V_n, "Pass", "Fail")$

Shear Reinforcement Check

TV = "Pass"

$\frac{\Phi_v \cdot V_n}{V_u} = 1.304$

Spatial Check

$$s_m := \text{Floor}\left[\frac{\left[b - 2\cdot\left(d_{cc} + t_v\right) - n_a\cdot OD\right]}{\left(n_a - 1\right)}, 0.125in\right] = 2.875\cdot in$$

assembly horizontal clear spacing

$s_{mmin} := \max\left(1.5\cdot t_s, 1.5D_a, 1.5in\right) = 2.25\cdot in$ minimum assembly spacing

$s_{mmax} := \min(1.5\cdot h, 18in) = 18\cdot in$ maximum assembly spacing

$Ts := \text{if}\left(s_{mmax} \geq s_m \geq s_{mmin}, \text{"Pass"}, \text{"FAIL"}\right)$

Flexure Bar Spacing Check

Ts = "Pass"

$dmin := c + 1in + \frac{OD}{2} = 8.3507\cdot in$ minimum tensile region

$Td := \text{if}(d \geq dmin, \text{"Pass"}, \text{"FAIL"})$

Tensile Region Check

Td = "Pass"

$IC := \pi\cdot ID = 18.8496\cdot in$ inner circumference of assembly

$cl := \frac{ID}{2}\cdot\cos\left[0.5\cdot\left(\frac{360deg}{n_s} - \theta\right)\right] = 1.9825\cdot in$ strand clearance

$Tcl := \text{if}\left(s_{mmax} \geq cl \geq s_{mmin}, \text{"Pass"}, \text{"FAIL"}\right)$

Aggregate Clearance Check

Tcl = "FAIL"

$A_{cz} := n_a\cdot\frac{\pi\cdot ID^2}{4} = 56.5487\cdot in^2$ area of constriction zone

Type II - Prototype Summary

Dimensions:

$L_b := L + 2in = 15ft$ beam length

$L = 178 \cdot in$ span length

$b = 24 \cdot in$ beam width

$h = 25.5 \cdot in$ beam height

Reinforcement:

$d_{cc} = 2 \cdot in$ clear cover

Flexure

$n_a = 2$ number of assemblies

$s_m = 2.875 \cdot in$ assembly spacing

$t_s = 1 \cdot in$ strand thickness

$w_{si} = 1.19 \cdot in$ strand inner width

$w_{so} := \theta \cdot \frac{OD}{2} = 1.5867 \cdot in$ strand outter width

$ID = 6 \cdot in$ inner diameter

$OD = 8 \cdot in$ outter diameter

$A_m = 2.6515 \cdot in^2$ single unit area

$s_{m_h} = 2.875 \cdot in$ assembly horizontal clear spacing

$A_t = 5.303 \cdot in^2$ total reinforcement area

$d = 18.969 \cdot in$ effective depth

$cl = 1.9825 \cdot in$ strand clearance

$D_{a} = 1.5 \cdot in$ max coarse aggregate

$A_{cz} = 56.5487 \cdot in^2$ area of compression zone in beam cross-section

Shear

$n_v = 30$ number of required stirups

$t_{s_v} = 0.531 \cdot in$ stirup strand thickness

$A_v = 0.282 \cdot in^2$ area of stirup bar

$r_b = 1.593 \cdot in$ radius of stirup bend

$l_{tmin} = 6.372 \cdot in$ legnth of stirup tail beyond hook

$s_v = 4.25 \cdot in$ stirup centroid spacing

$x = 17.5 \cdot in$ cut-off distance from midpoint

Loading:

$P = 48.5831 \cdot kip$ prototype load capacity

$M := \frac{P \cdot L}{3} = 240.2162 \cdot kip \cdot ft$ prototype moment capacity

Type II - Model Summary

$N = 0.3333$ scale factor

Dimensions:

$L_b \cdot N = 5\,ft$ beam length

$L \cdot N = 59.3333 \cdot in$ span lenth

$b \cdot N = 8 \cdot in$ beam width

$h \cdot N = 8.5 \cdot in$ beam height

Reinforcement:

$d_{cc} \cdot N = 0.6667 \cdot in$ clear cover

Flexure

$n_a = 2$ number of assemblies

$s_m \cdot N = 0.9583 \cdot in$ assembly spacing

$t_s \cdot N = 0.3333 \cdot in$ strand thickness

$w_{si} \cdot N = 0.3967 \cdot in$ inner strand width

$w_{so} \cdot N = 0.5289 \cdot in$ outter strand width

$ID \cdot N = 2 \cdot in$ inner diameter

$OD \cdot N = 2.6667 \cdot in$ outter diameter

$A_m \cdot N^2 = 0.2946 \cdot in^2$ single unit area

$s_w \cdot N = 0.9583 \cdot in$ assembly horizontal clear spacing

$A_t \cdot N^2 = 0.5892 \cdot in^2$ total reinforcement area

$d \cdot N = 6.323 \cdot in$ effective depth

$cl \cdot N = 0.6608 \cdot in$ strand clearance

$D_a \cdot N = 0.5 \cdot in$ max coarse aggregate

$A_{cz} \cdot N^2 = 6.2832 \cdot in^2$ area of compression zone in beam cross-section

Shear

$n_v = 30$ number of required stirrups

$t_s \cdot N = 0.177 \cdot in$ stirrup strand thickness

$A_v \cdot N = 0.094 \cdot in^2$ area of stirrup bar

$r_b \cdot N = 0.531 \cdot in$ radius of stirrup bend

$l_{tmin} \cdot N = 2.124 \cdot in$ legnth of stirrup tail beyond hook

$s_v \cdot N = 1.4167 \cdot in$ stirrup centroid spacing

$x \cdot N = 5.8333 \cdot in$ cut-off distance from midpoint

Loading:

$P \cdot N^2 = 5.3981 \cdot kip$ model load capacity

$M \cdot N^3 = 8.8969\,ft \cdot kip$ model moment capacity

Type III

Sinusoidal Weave FRP Reinforced Beam

Input values & definitions

Beam Dimensions

$L := 178in$ span length

$h := 24in$ beam height

$b := 24in$ beam width

Scaling

$N := \frac{1}{3}$ model scale factor

Reinforcement

$dc := 2in$ clear cover distance (AASHTO 5.12.3)

Flexure

$sA := 2in$ strand amplitude

$st := 0.1703in \cdot N^{-1} = 0.5109 \cdot in$ strand thickness

$sw := 0.1703in \cdot N^{-1} = 0.5109 \cdot in$ strand width

Shear

$vt := N^{-1} \cdot 0.177in = 0.531 \cdot in$ stirup strand height

FRP Specifications

$CE := 0.8$ environmental reduction factor - glass/not exposed [ACI-440.1a Table 7.1]

$FFU := 72 \cdot ksi$ FRP tensile strength

$Ef := 5864 \cdot ksi$ FRP modulus of elasticity

Concrete Specifications

$FC := 4000psi$ concrete compressive strength

$\varepsilon cu := 0.003$ concrete ultimate strain

$Dconc := 150 \cdot \frac{lbf}{ft^3}$ density of concrete

$ca := 1.5in$ maximum coarse aggregate

Flexure Design

$ffu := CE \cdot FFU = 57.6 \cdot ksi$ design tensile strength of FRP, considering reductions for service environment

$\beta 1 := if\left(FC \le 4 \cdot ksi, 0.85, if\left(FC < 8 \cdot ksi, -.05 \cdot \frac{FC}{ksi} + 0.95, 0.65\right)\right) = 0.85$

$\rho fb := 0.85 \cdot \frac{FC}{ffu} \cdot \beta 1 \cdot \frac{Ef \cdot \varepsilon cu}{Ef \cdot \varepsilon cu + ffu} = 0.0117$ balanced reinforcement ratio

$uw := \sqrt{2}(sA + st) = 3.5509 \cdot in$ single unit width

$uh := \sqrt{2} \cdot (sA + st + sw) = 4.2735 \cdot in$ single unit height

$d := h - dc - vt - \frac{uh}{2} = 19.3323 \cdot in$ distance from extreme compression fiber to centroid of tension reinforcement

$n := Floor\left[\frac{b - 2(dc + uh)}{uw}, 1\right] + 2 = 5$ number of units

$Am := 4 \cdot st \cdot sw = 1.0441 \cdot in^2$ single unit cross-sectional area

$At := n \cdot Am = 5.2204 \cdot in^2$ total reinforcement area

$\rho f := \frac{At}{b \cdot d} = 0.0113$ FRP reinforcement ratio

$Fmode := if(\rho f < \rho fb, "FRP\ rupture", "Concrete\ crushing")$

Failure Mode

$Fmode = "FRP\ rupture"$

$ff := \sqrt{\frac{(Ef \cdot \varepsilon cu)^2}{4} + \frac{0.85 \cdot \beta 1 \cdot FC}{\rho f} \cdot Ef \cdot \varepsilon cu} - 0.5 \cdot Ef \cdot \varepsilon cu = 58.9977 \cdot ksi$ stress in FRP reinforcement in tension at concrete failure

$Mn := \rho f \cdot ff \cdot \left(1 - 0.59 \cdot \frac{\rho f \cdot ff}{FC}\right) \cdot b \cdot d^2 = 447.5971 \cdot kip \cdot ft$ nominal moment capacity

$\Phi f := if\left(\rho f \le \rho fb, 0.55, if\left(\rho f < 1.4\rho fb, 0.3 + 0.25\frac{\rho f}{\rho fb}, 0.65\right)\right) = 0.55$ flexural strength reduction factor

$\Phi f \cdot Mn = 246.1784 \cdot kip \cdot ft$ factored ultimate moment capacity

$P := \frac{3 \cdot \Phi f \cdot Mn}{L} = 49.7889 \cdot kip$ factored ultimate load capacity

Shear Design

$Vu := P = 49.7889 \cdot kip$ factored shear force at section

$\Phi v := 0.75$ strength reduction factor

$Ec := 57000psi \cdot \sqrt{\frac{FC}{psi}} = 3604.9965 \cdot ksi$ modulus of elasticity of concrete

$nf := \frac{Ef}{Ec} = 1.6266$ ratio of modulus of elasticity of FRP bars to modulus of elasticity of concrete

$k := \sqrt{2 \cdot \rho f \cdot nf + (\rho f \cdot nf)^2} - \rho f \cdot nf = 0.1739$ ratio of depth of neutral axis to reinforcement depth

$c := k \cdot d = 3.3617 \cdot in$ distance from extreme compression fiber to the neutral axis

$Vc := 5 \cdot \sqrt{\frac{FC}{psi}} psi \cdot b \cdot c = 25.5138 \cdot kip$ nominal shear strength provided by concrete

$Ts := if\left(Vu \le \Phi v \cdot \frac{Vc}{2}, "No\ Stirrups\ Reqd", "Stirrups\ Needed"\right)$

Stirrup Check

$Ts = "Stirrups\ Needed"$

$Av := vt^2 = 0.282 \cdot in^2$ cross-sectional area of single stirrup bar

$rb := 3 \cdot vt = 1.593 \cdot in$ internal radius of bend in FRP reinforcement

$ffb := \left(0.3 + 0.05 \cdot \frac{rb}{vt}\right) \cdot ffu = 25.92 \cdot ksi$ strength of bent portion of stirrup

$ffv := \min(ffb, 0.004 \cdot Ef) = 23.456 \cdot ksi$ tensile strength of stirrup

$smax := \min\left[\frac{2Av \cdot ffv}{50psi \cdot b}, \frac{\Phi v \cdot 2Av \cdot ffv \cdot d}{(Vu - \Phi v \cdot Vc)}, 24in, \frac{d}{2}\right] = 6.2566 \cdot in$ maximun stirrup spacing

$s := Floor\left(\frac{1.5^{-1} smax}{in}, 0.125\right) in = 4.125 \cdot in$ stirrup centroid spacing (modified for x1.5 reqd)

$x := Ceil\left(\frac{L \cdot \Phi v \cdot Vc}{4 \cdot Vu}, 0.25in\right) = 17.25 \cdot in$ cut-off distance from midpoint

$ltmin := 12 \cdot vt = 6.372 \cdot in$ minimum stirrup tail length

$nv := ceil\left(\frac{\frac{L}{2} - dc - x}{s + vt}\right) \cdot 2 = 30$ number of stirrups

$Vs := \frac{2Av \cdot ffv \cdot d}{s} = 61.9914 \cdot kip$ shear strength from stirrups (approximation based on ACI 318)

$Vn := Vs + Vc = 87.5053 \cdot kip$ nominal shear strength

$\Phi v \cdot Vn = 65.629 \cdot kip$ factored shear strength

Shear Reinforcement Check

$TV := if(Vu \le \Phi v \cdot Vn, "Pass", "Fail")$

$TV = "Pass"$

$\frac{\Phi v \cdot Vn}{Vu} = 1.3181$

Type III - Prototype Summary

Dimensions:

$Lb := L + 2in = 15ft$ beam length

$L = 178 \cdot in$ span length

$b = 24 \cdot in$ beam width

$h = 24 \cdot in$ beam height

Reinforcement:

$dc = 2 \cdot in$ clear cover

Flexure

$n = 5$ number of units

$st = 0.5109 \cdot in$ strand thickness

$sw = 0.5109 \cdot in$ strand width

$sA = 2 \cdot in$ strand amplitude

$Am = 1.0441 \cdot in^2$ single unit area

$aw := 2 \cdot uh + (n - 2) \cdot uw = 19.1998 \cdot in$ assembly total width

$At = 5.2204 \cdot in^2$ total reinforcement area

$d = 19.3323 \cdot in$ effective depth

Shear

$nv = 30$ number of required stirrups

$vt = 0.531 \cdot in$ stirrup strand thickness

$Av = 0.282 \cdot in^2$ area of stirrup bar

$rb = 1.593 \cdot in$ radius of stirrup bend

$ltmin = 6.372 \cdot in$ legnth of stirrup tail beyond hook

$s = 4.125 \cdot in$ stirrup centroid spacing

$x = 17.25 \cdot in$ cut-off distance from midpoint

Loading:

$P = 49.7889 \cdot kip$ prototype load capacity

$M := \frac{P \cdot L}{3} = 246.1784 \cdot kip \cdot ft$ prototype moment capacity

Type III - Model Summary

$N = 0.3333$ scale factor

Dimensions:

$Lb\_N = 5\,ft$ beam length

$L\_N = 59.3333\,in$ span lenth

$b\_N = 8\,in$ beam width

$h\_N = 8\,in$ beam height

Reinforcement:

$dc\_N = 0.6667\,in$ clear cover

Flexure

$n = 5$ number of units

$st\_N = 0.1703\,in$ strand thickness

$sw\_N = 0.1703\,in$ strand width

$sA\_N = 0.6667\,in$ strand amplitude

$Am\_N^2 = 0.116\,in^2$ single unit area

$aw\_N = 6.3999\,in$ assembly total width

$At\_N^2 = 0.58\,in^2$ total reinforcement area

$d\_N = 6.4441\,in$ effective depth

Shear

$nv = 30$ number of required stirups

$vt\_N = 0.177\,in$ stirup strand thickness

$Av\_N = 0.094\,in^2$ area of stirup bar

$rb\_N = 0.531\,in$ radius of stirup bend

$ltmin\_N = 2.124\,in$ legnth of stirup tail beyond hook

$s\_N = 1.375\,in$ stirup centroid spacing

$x\_N = 5.75\,in$ cut-off distance from midpoint

Loading:

$P\_N^2 = 5.5321\,kip$ model load capacity

$M\_N^3 = 9.1177\,ft{\cdot}kip$ model moment capacity

Appendix B - Specimen Design Drawings[5]

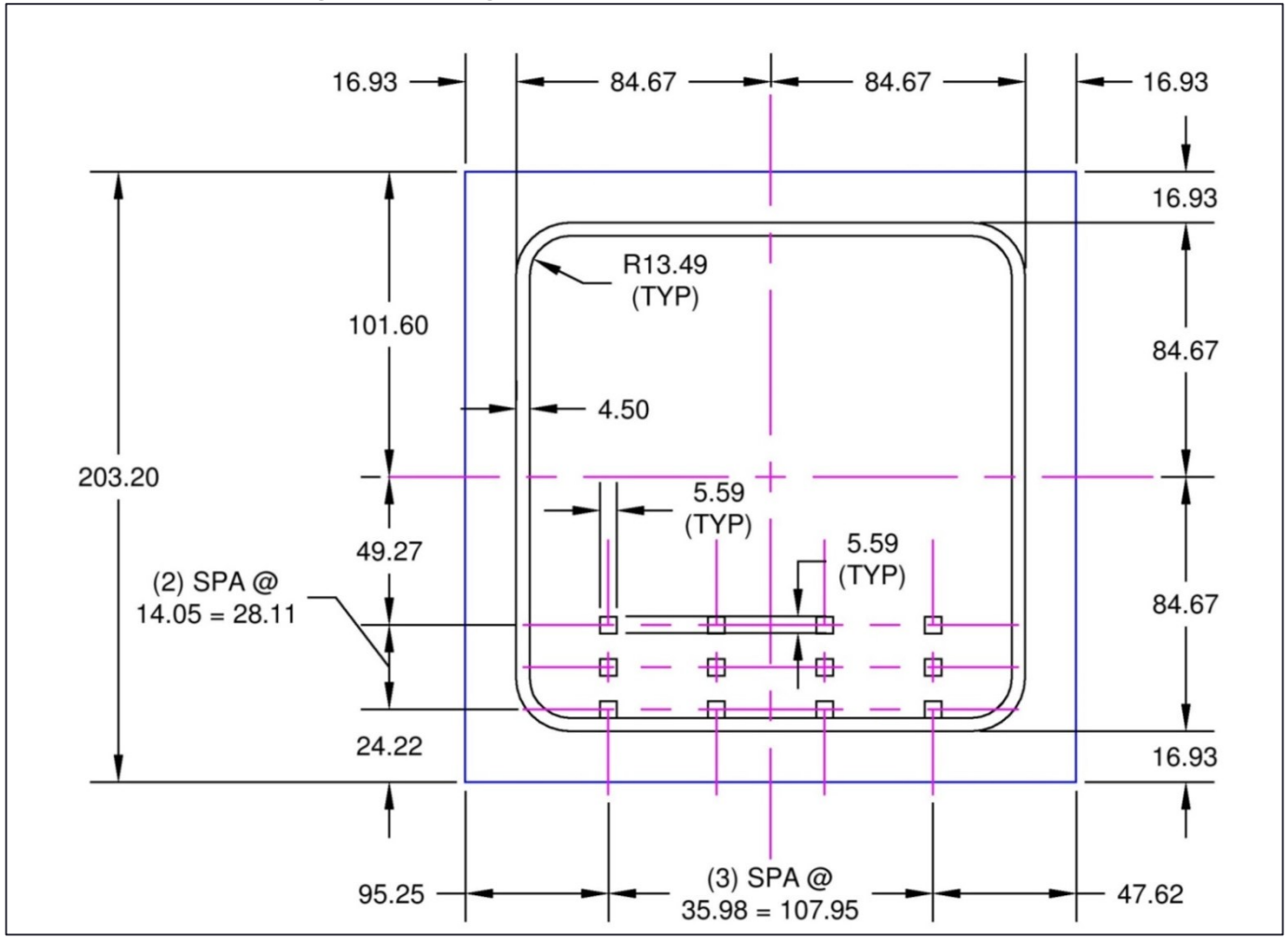

Figure B.1: Ia Cross-section

[5] Note: All dimensions are presented in millimeters.

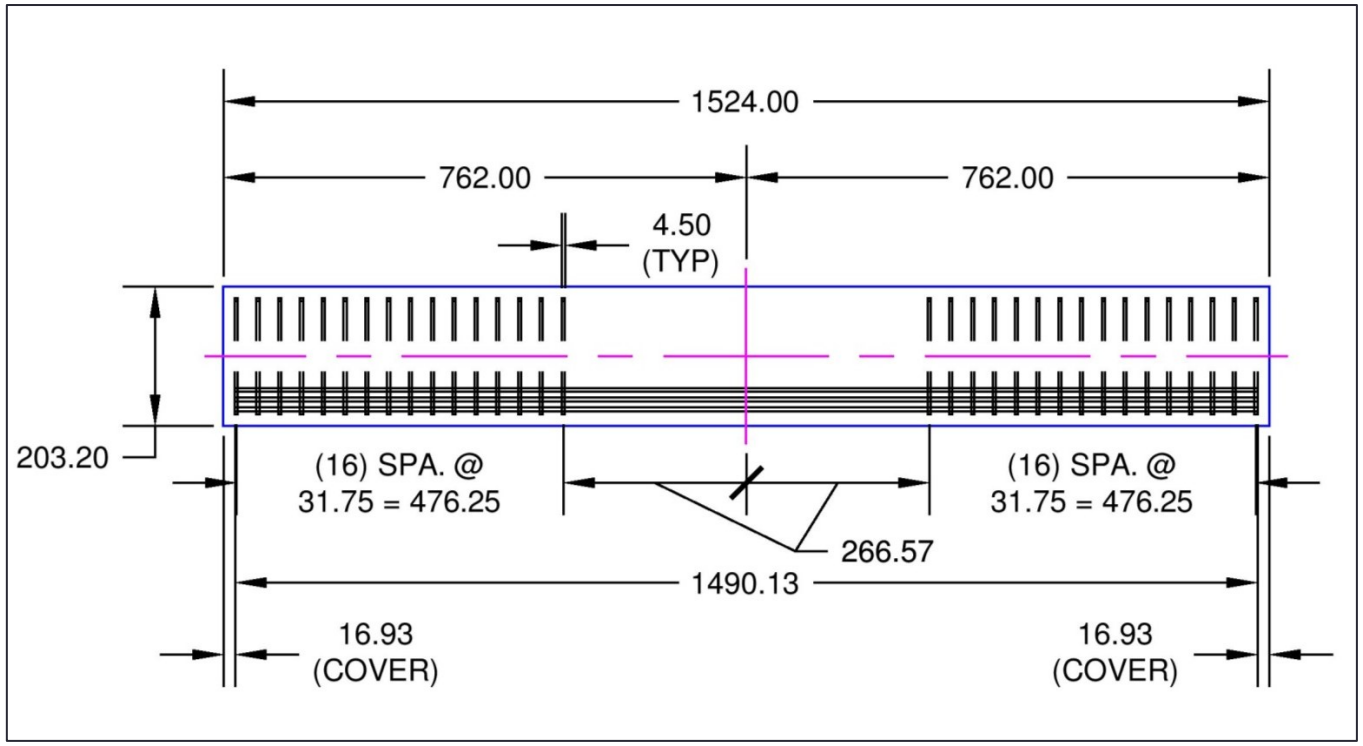

Figure B.2: Ia Side

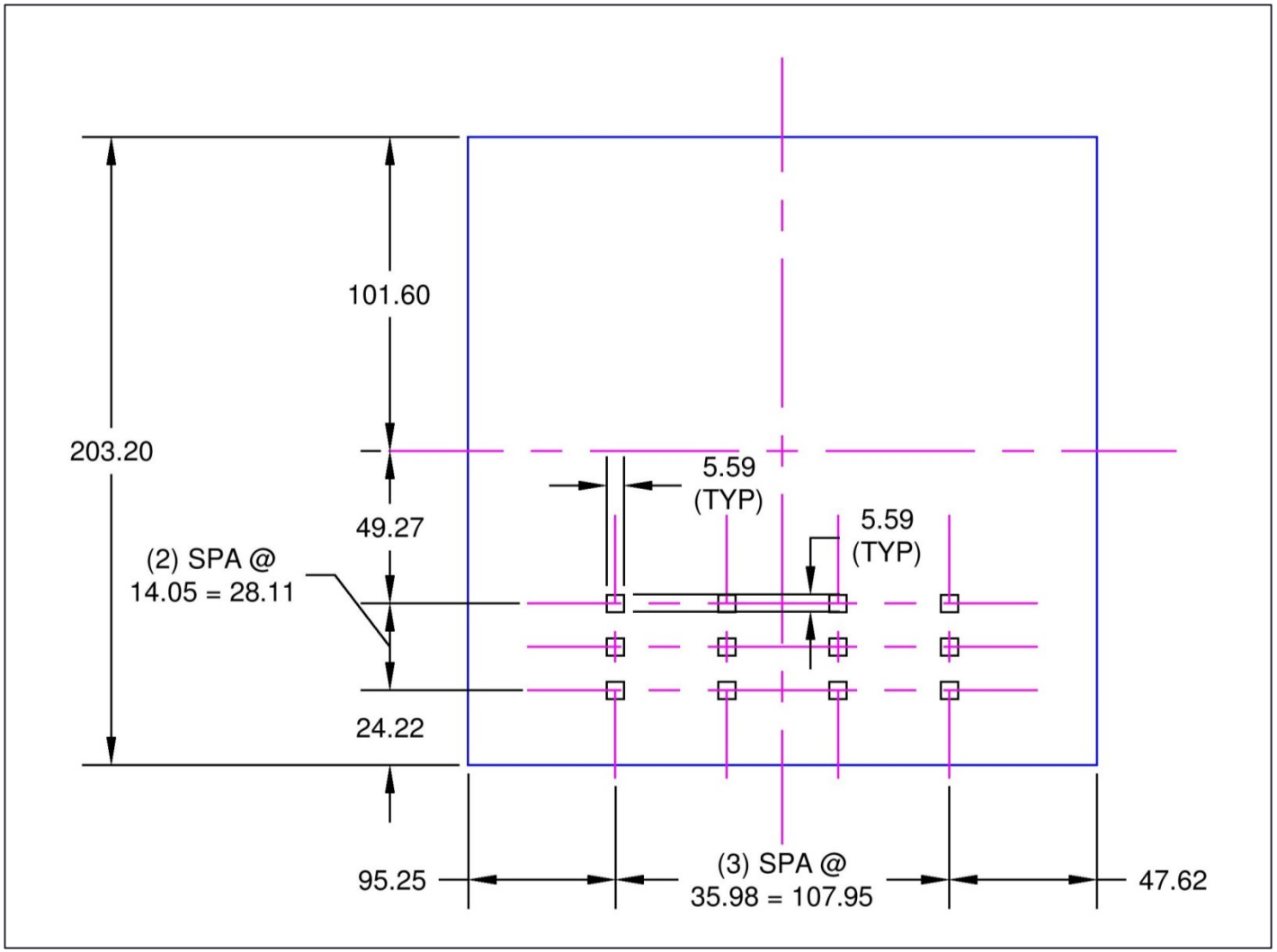

Figure B.3: Ib Cross-section

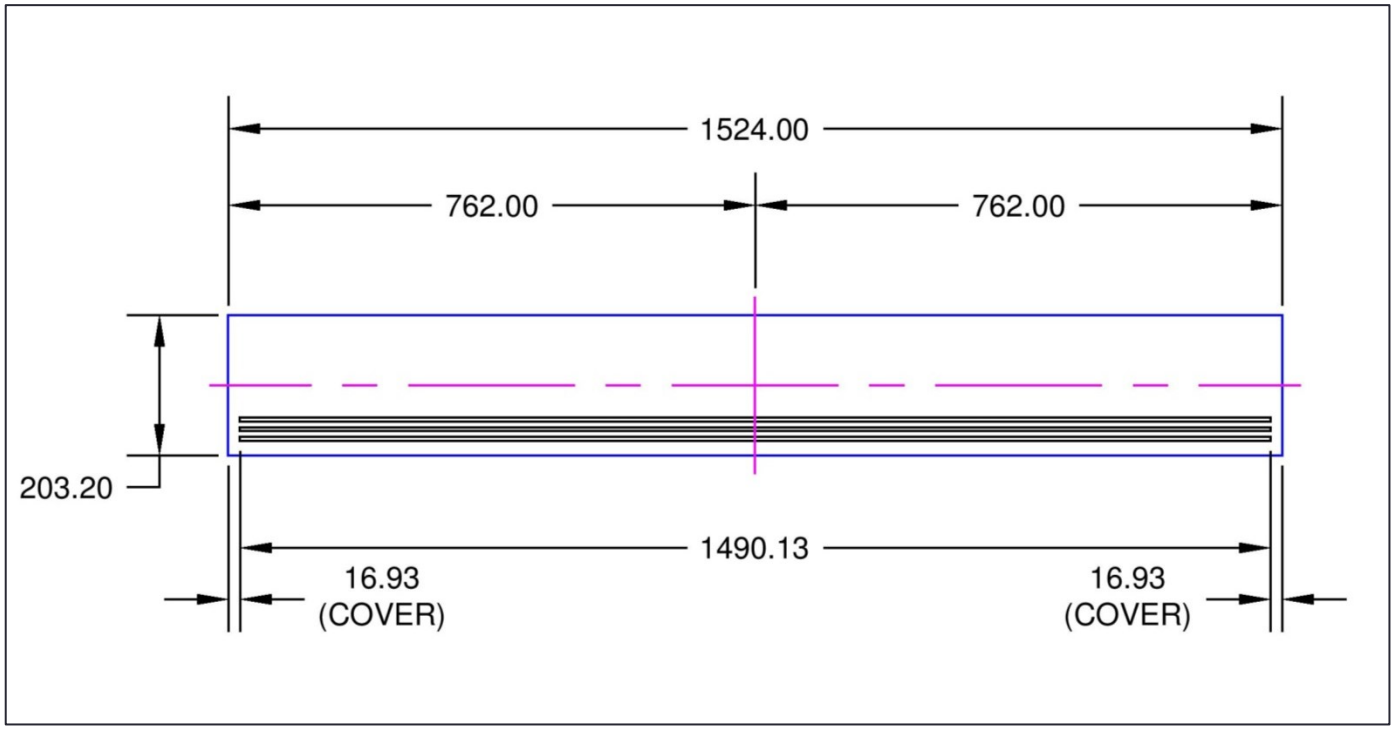

Figure B.4: Ib Side

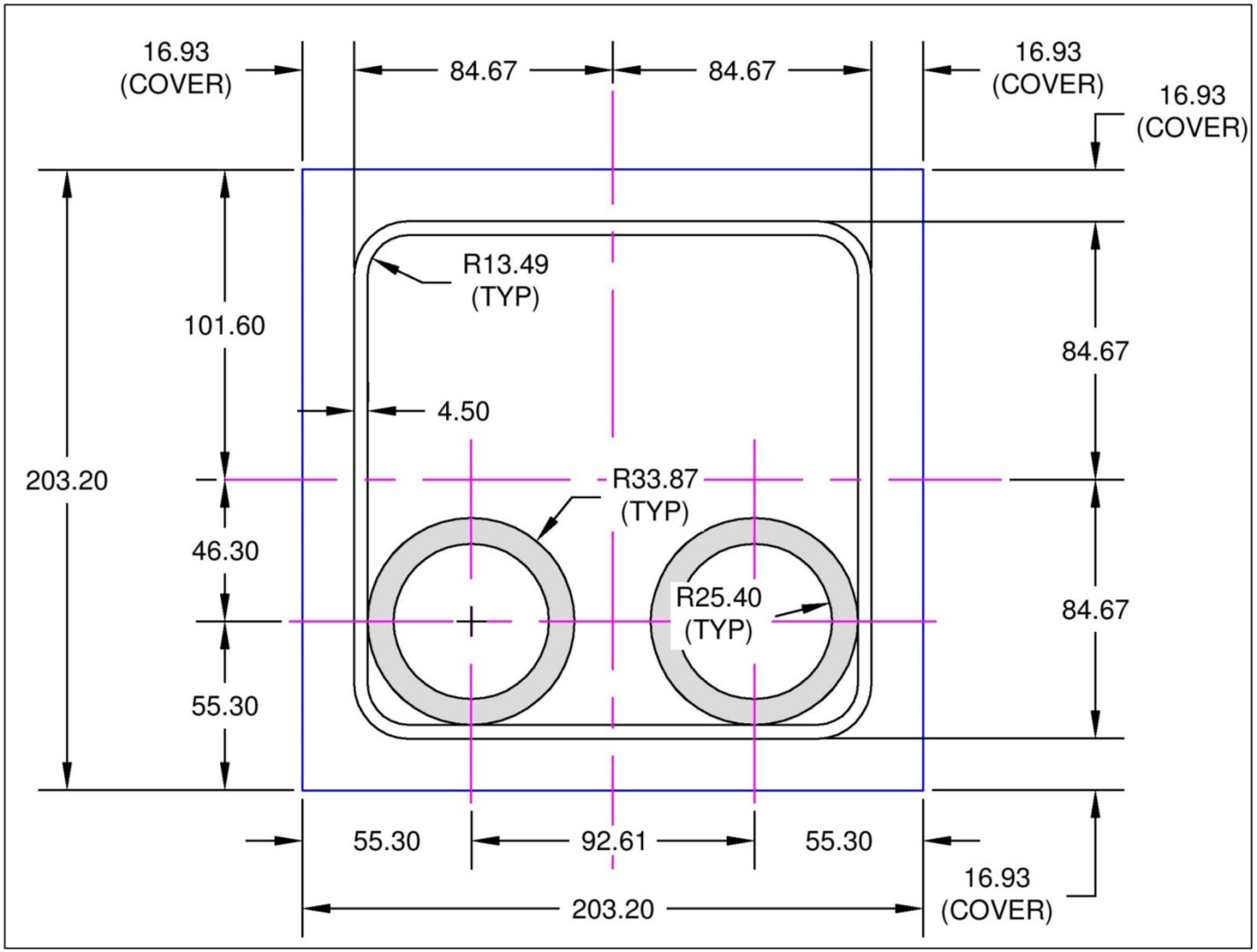

Figure B.5: IIa Cross-section

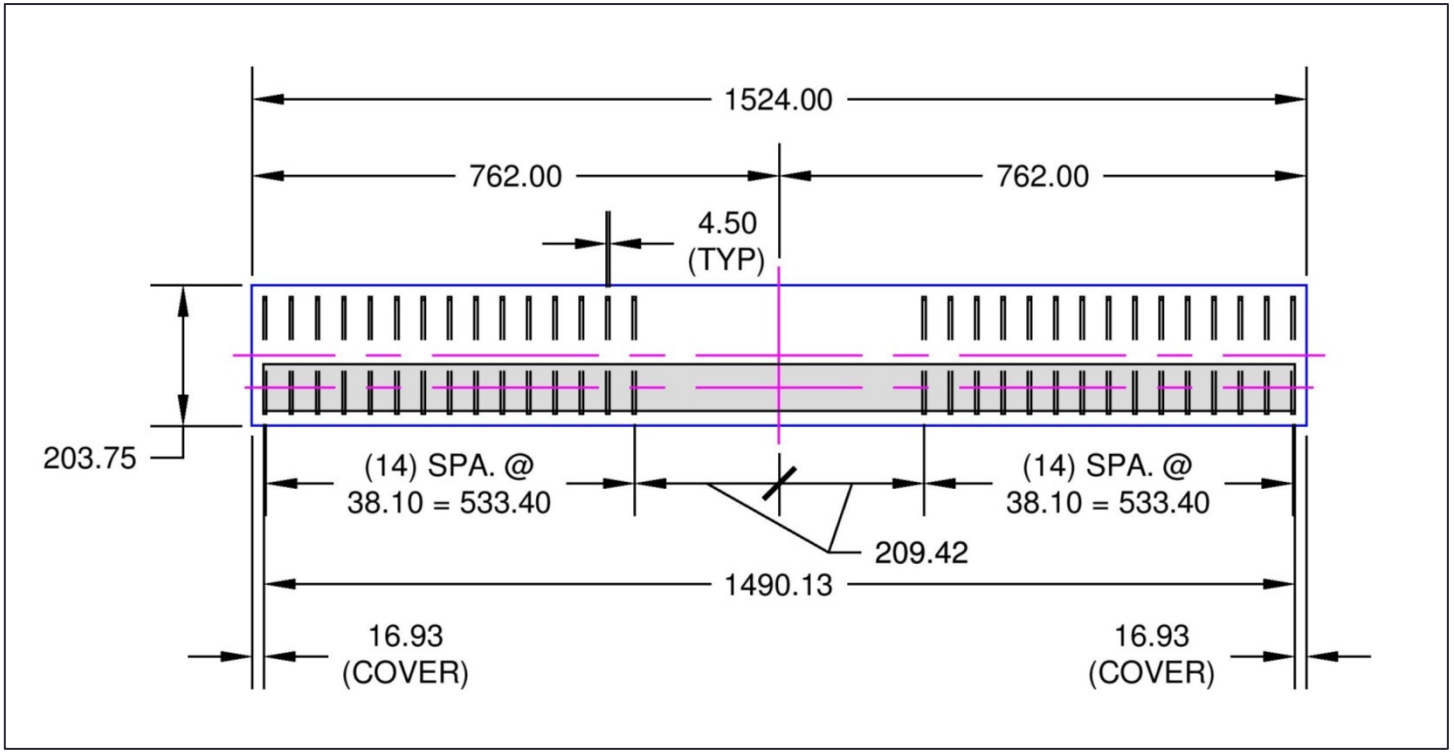

Figure B.6: IIa Side

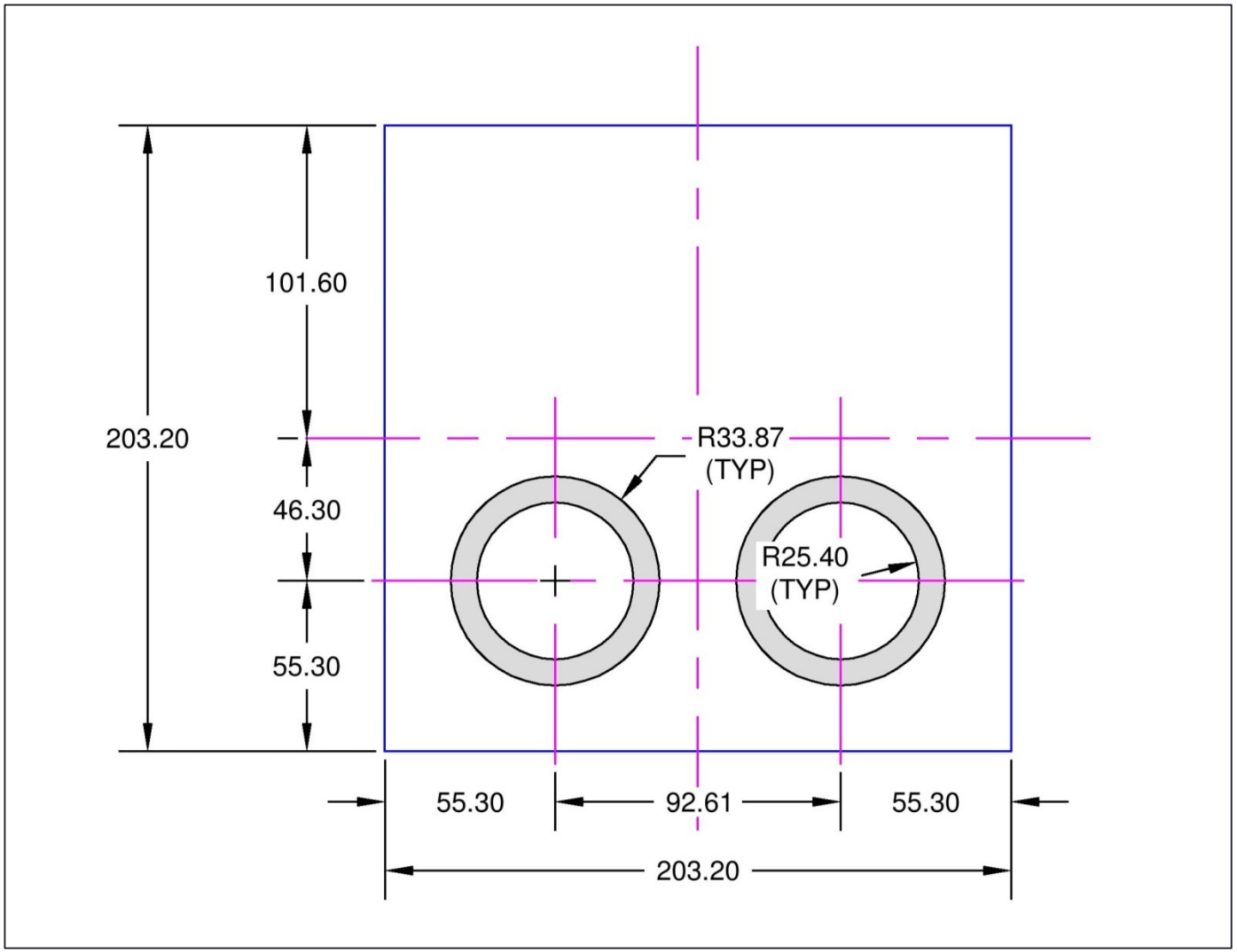

Figure B.7: IIb Cross-section

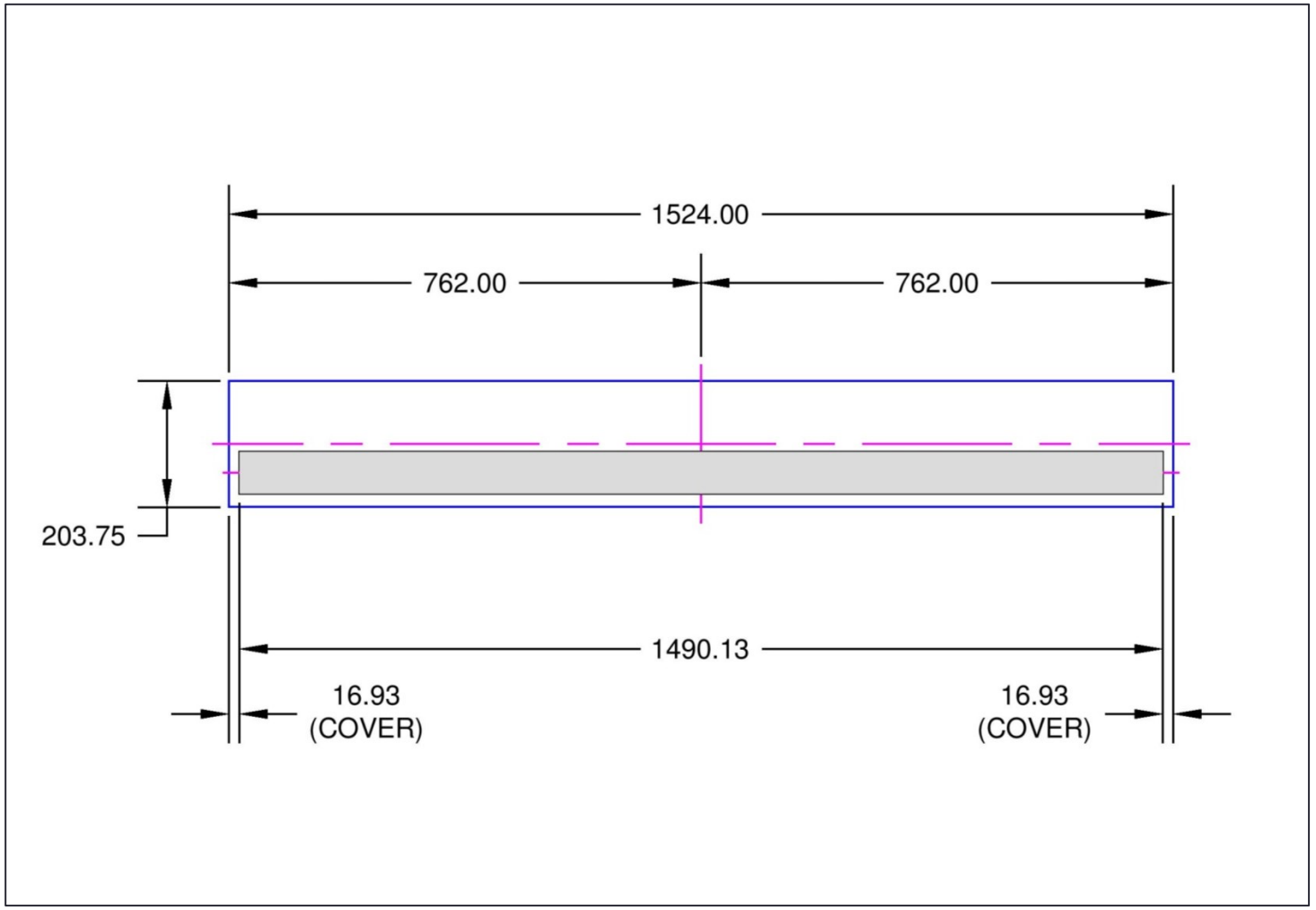

Figure B.8: IIb Side

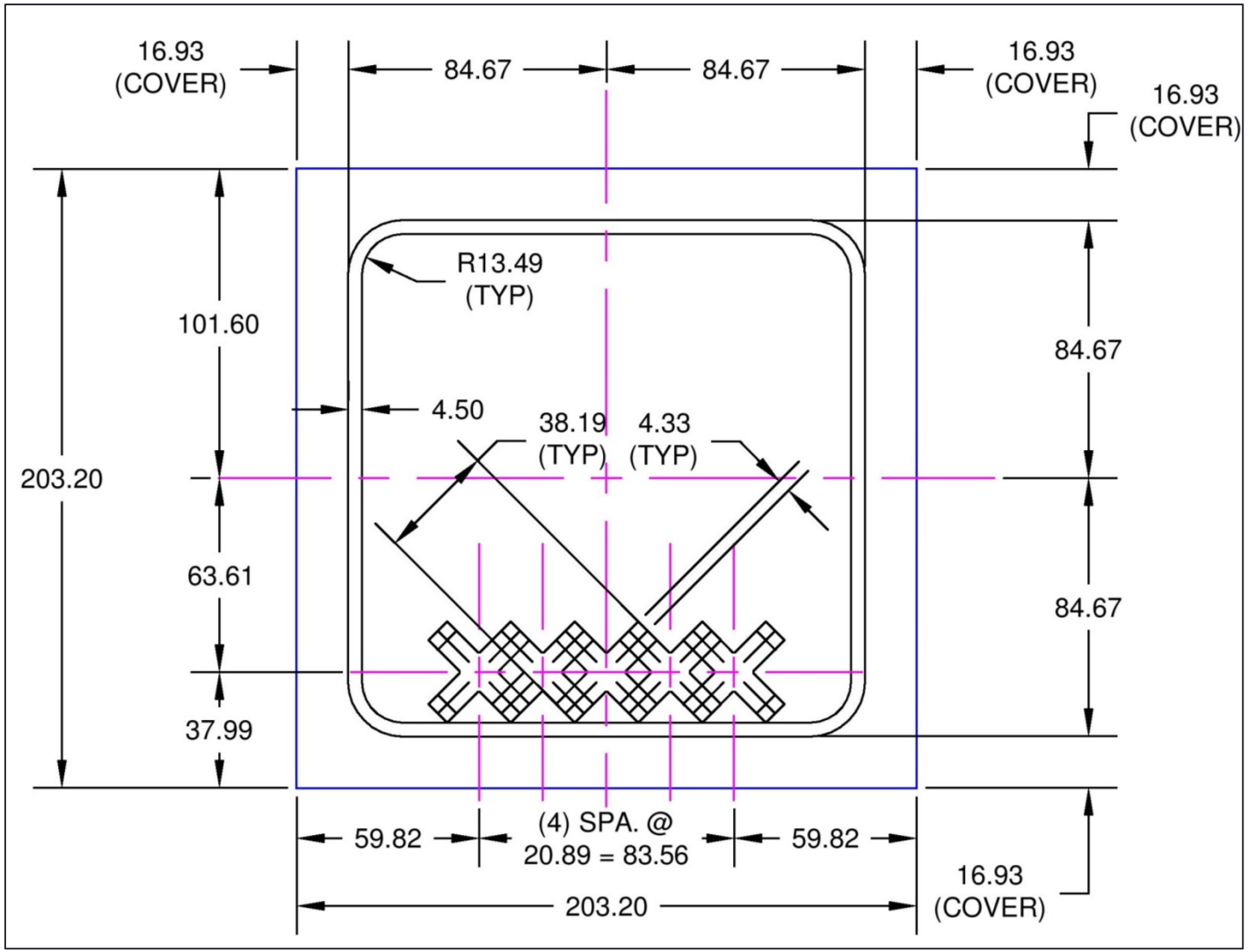

Figure B.9: IIIa Cross-section

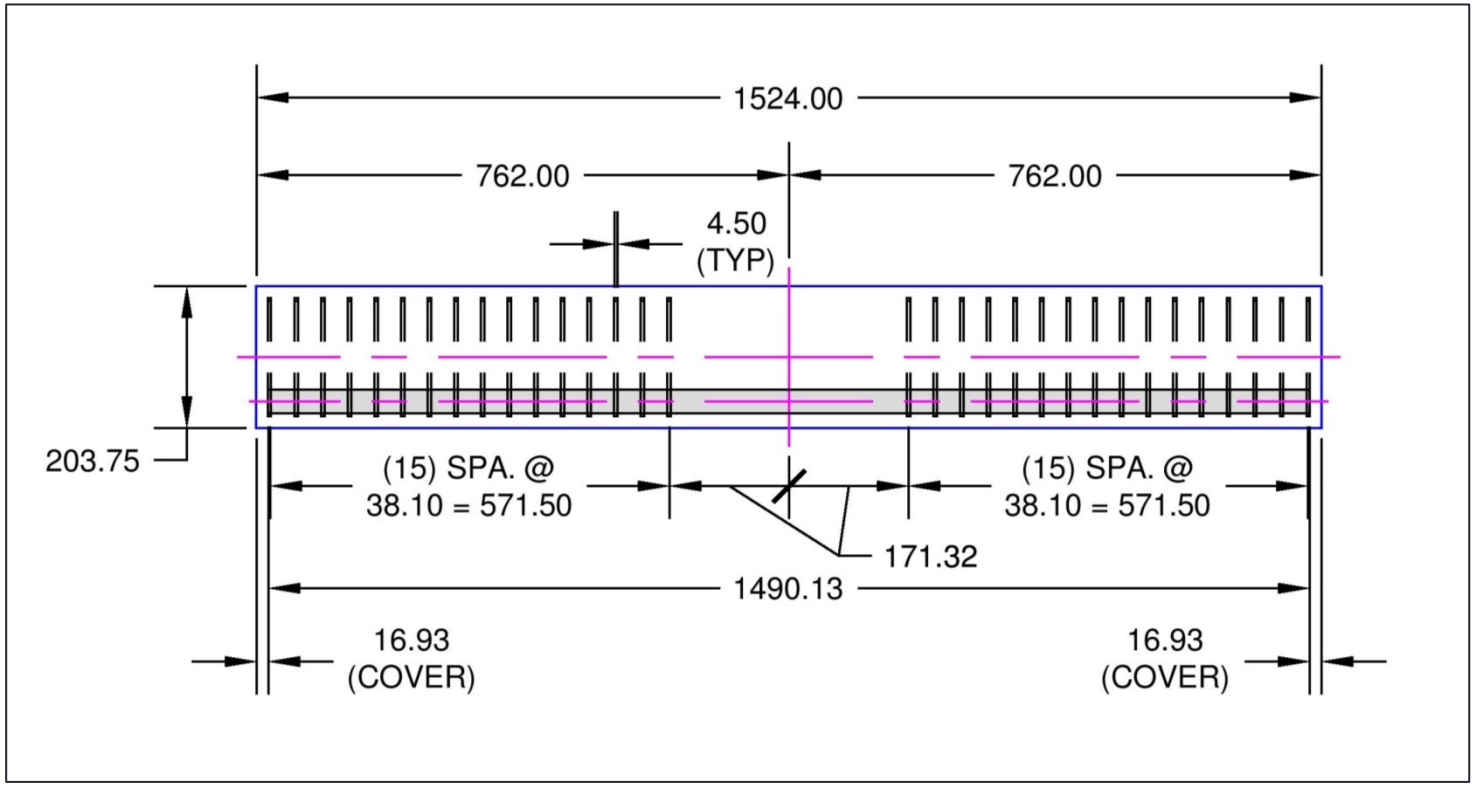

Figure B.10: IIIa Side

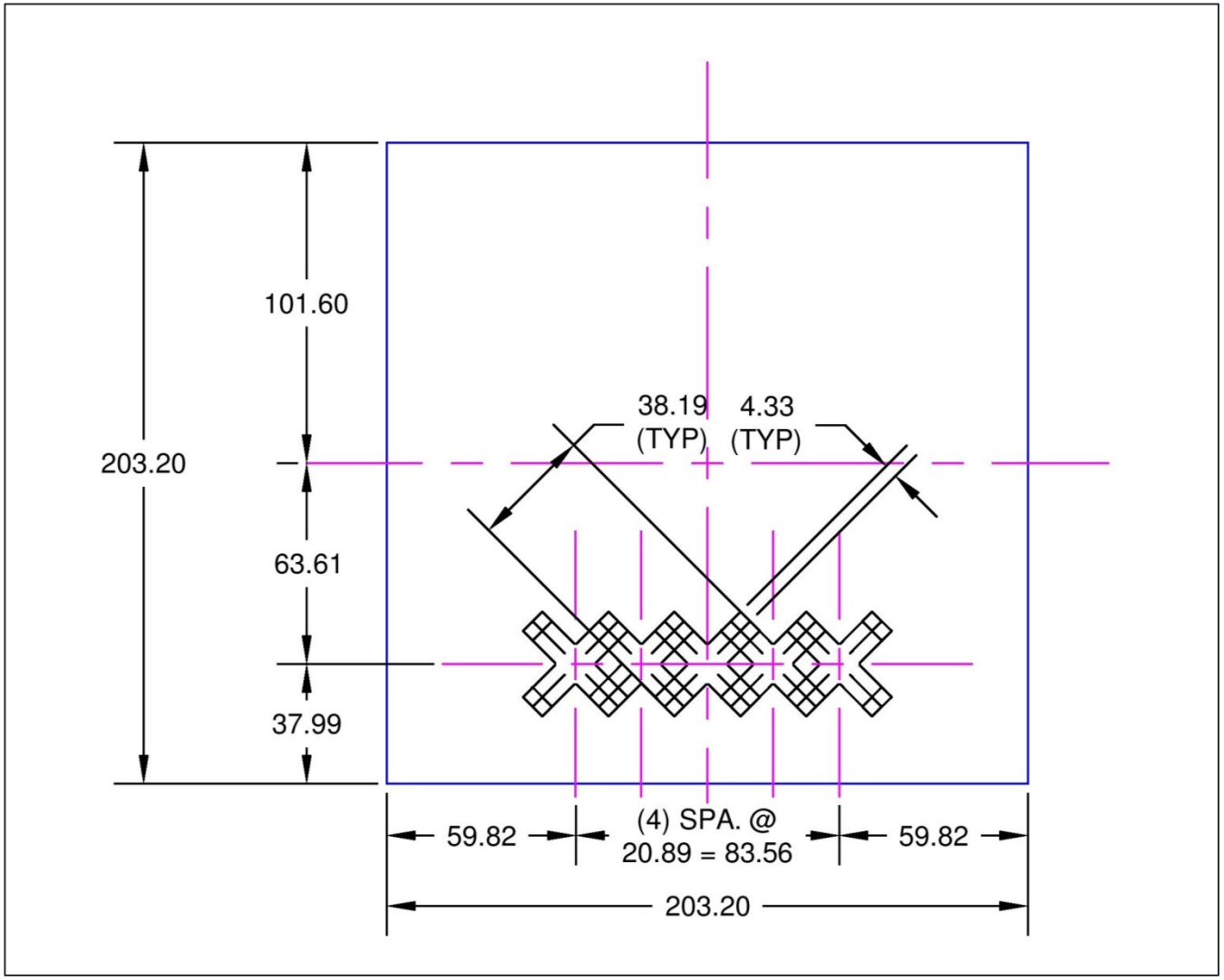

Figure B.11: IIIb Cross-section

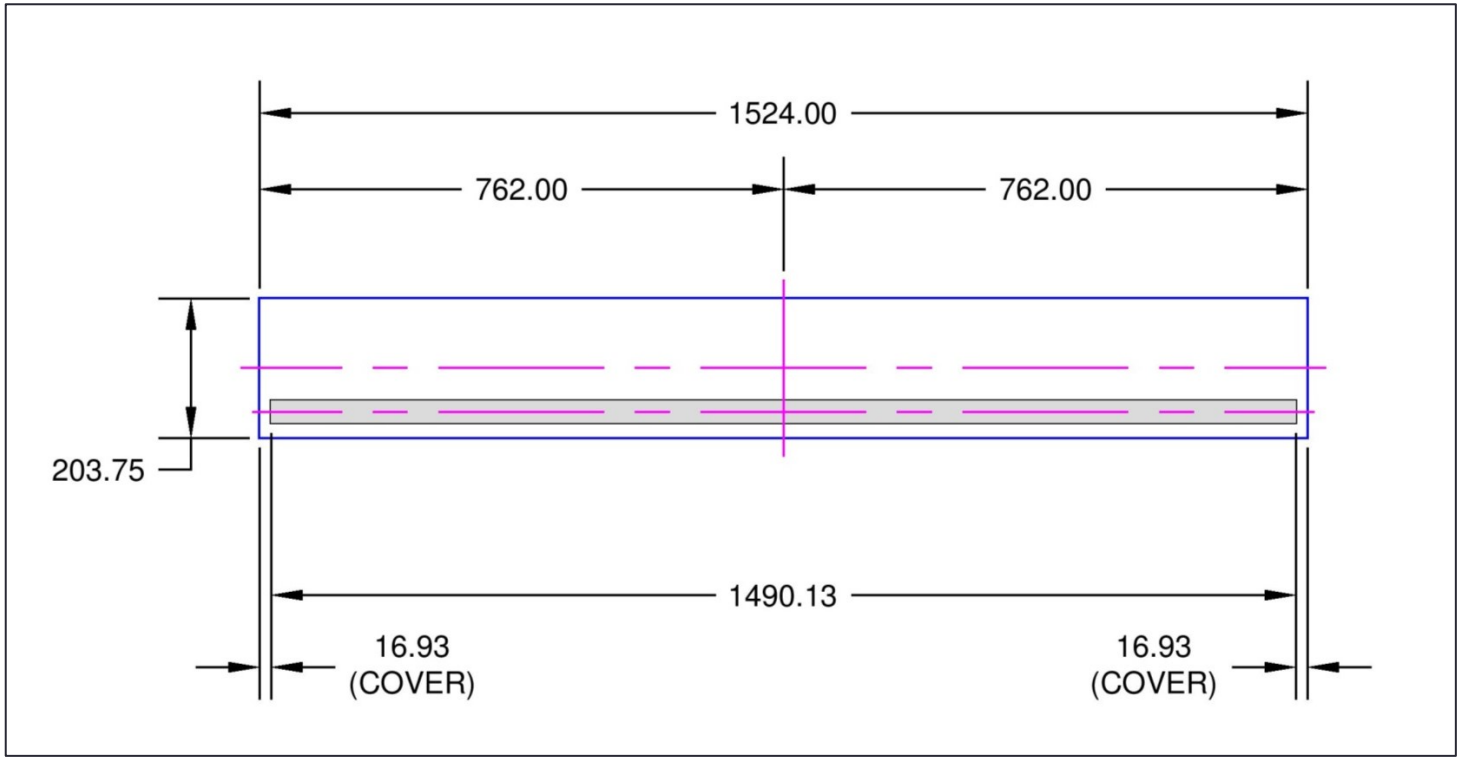

Figure B.12: IIIb Side

Appendix C - Experimental Data

Deflection Data

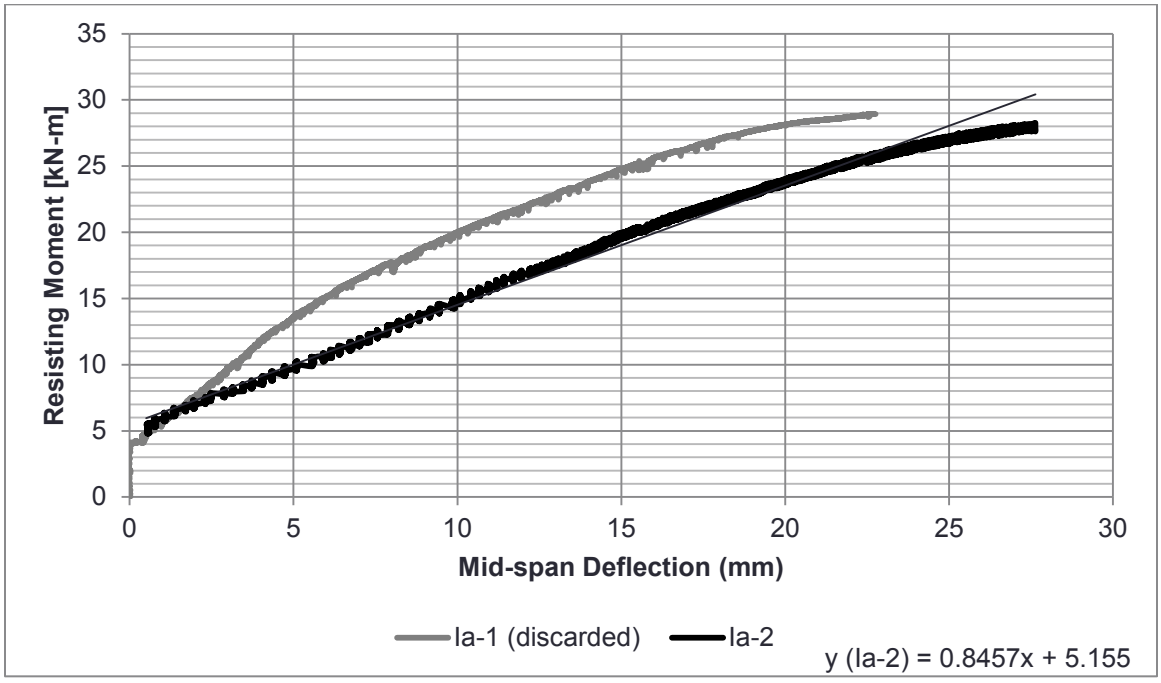

Figure C.1: Ia Deflection Curve

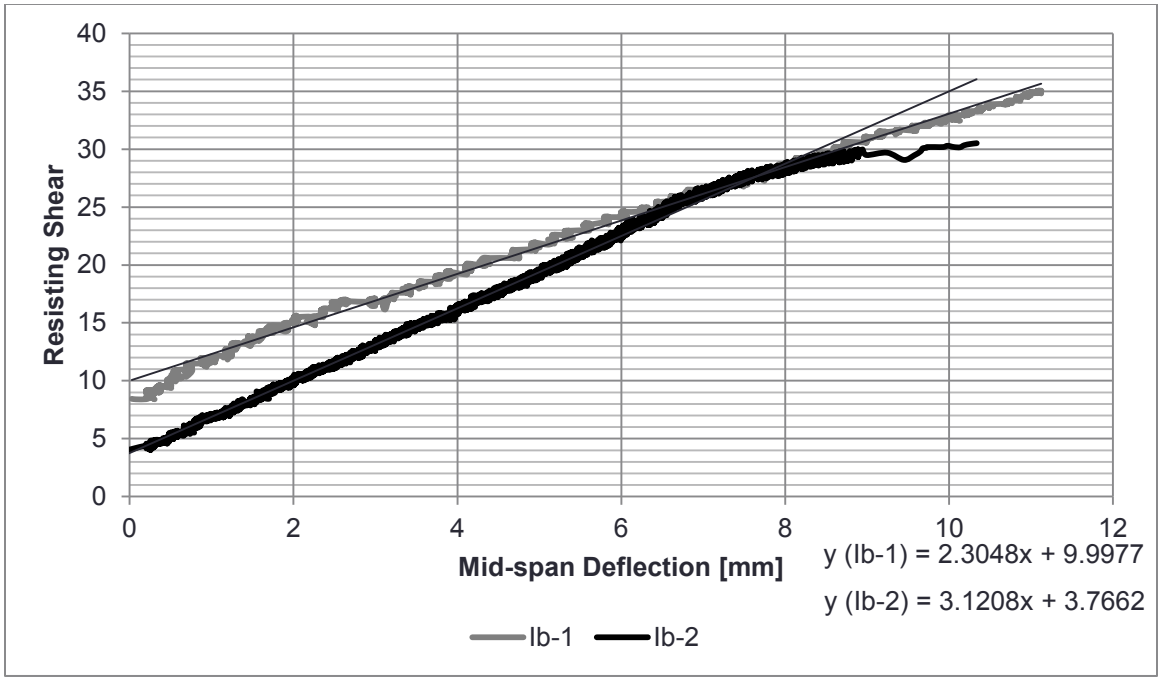

Figure C.2: Ib Deflection Curve

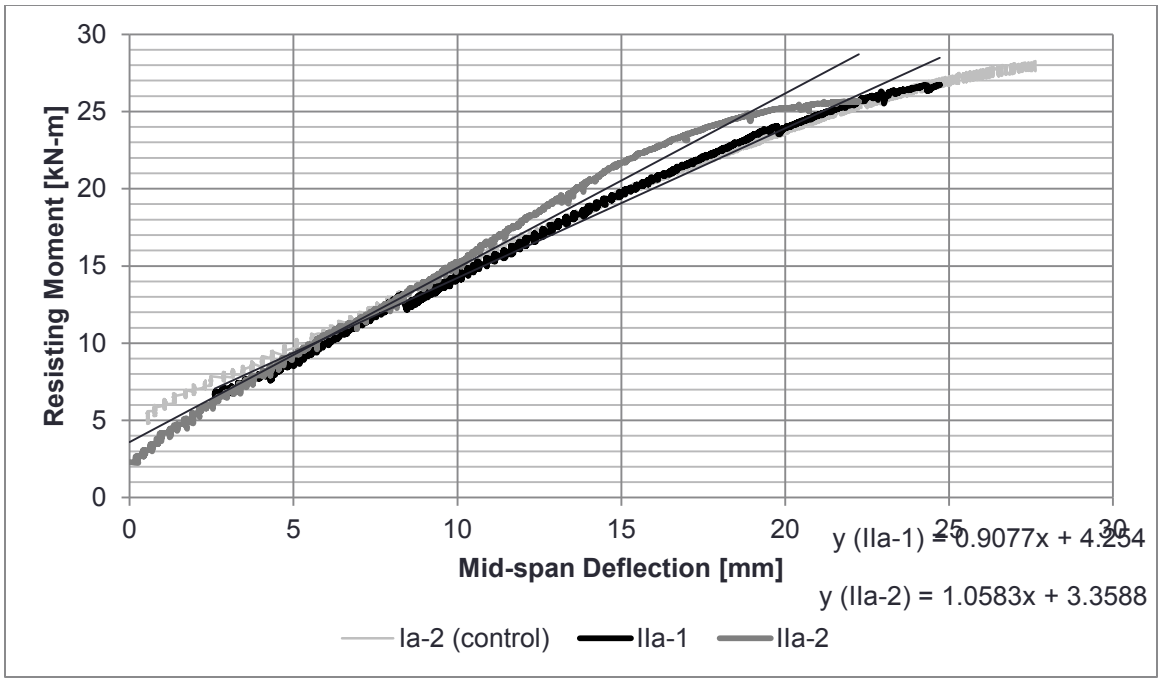

Figure C.3: IIa Beam Deflection Curve

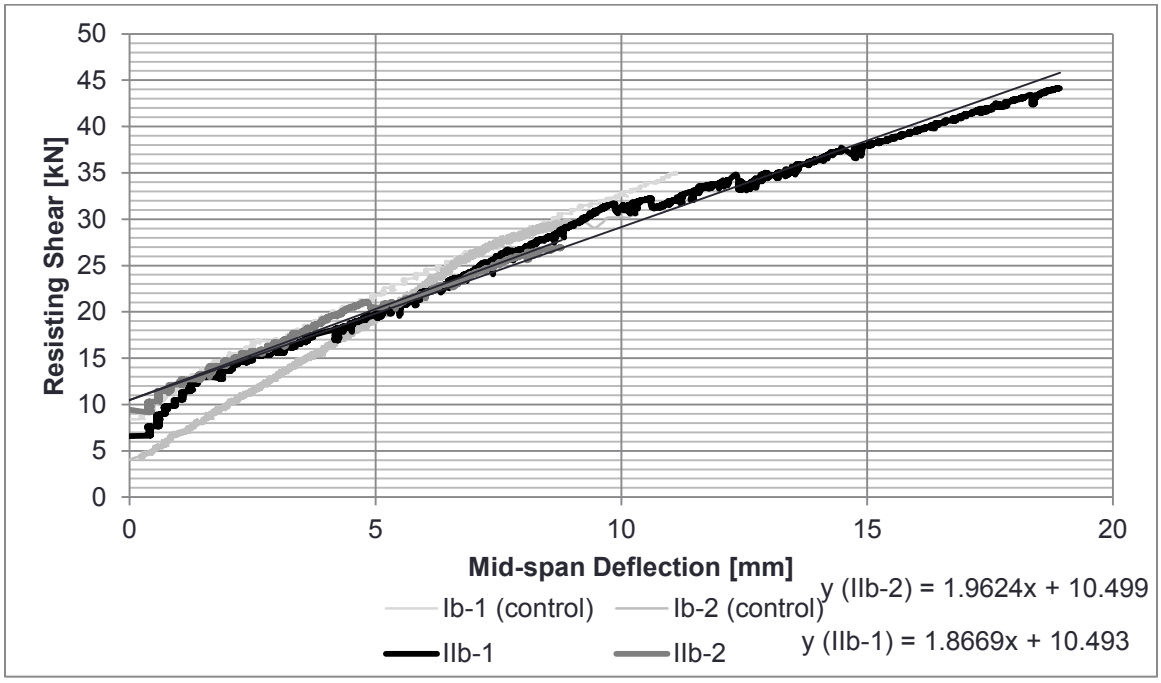

Figure C.4: IIb Beam Deflection Curve

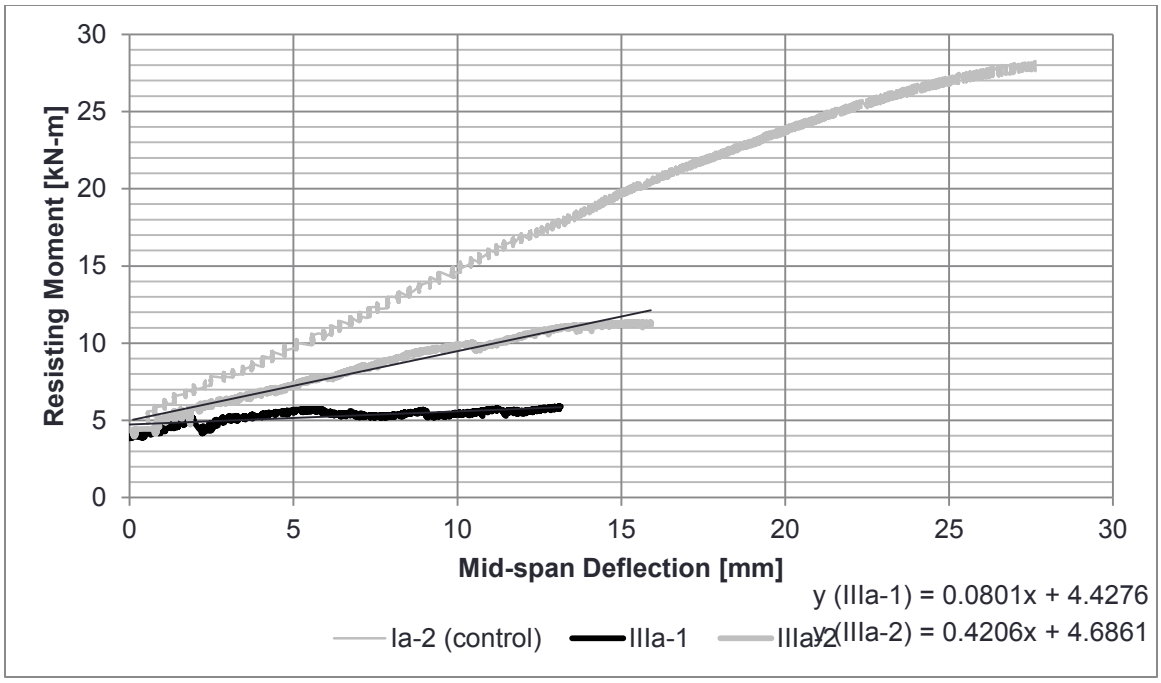

Figure C.5: IIIa Beam Deflection Curve

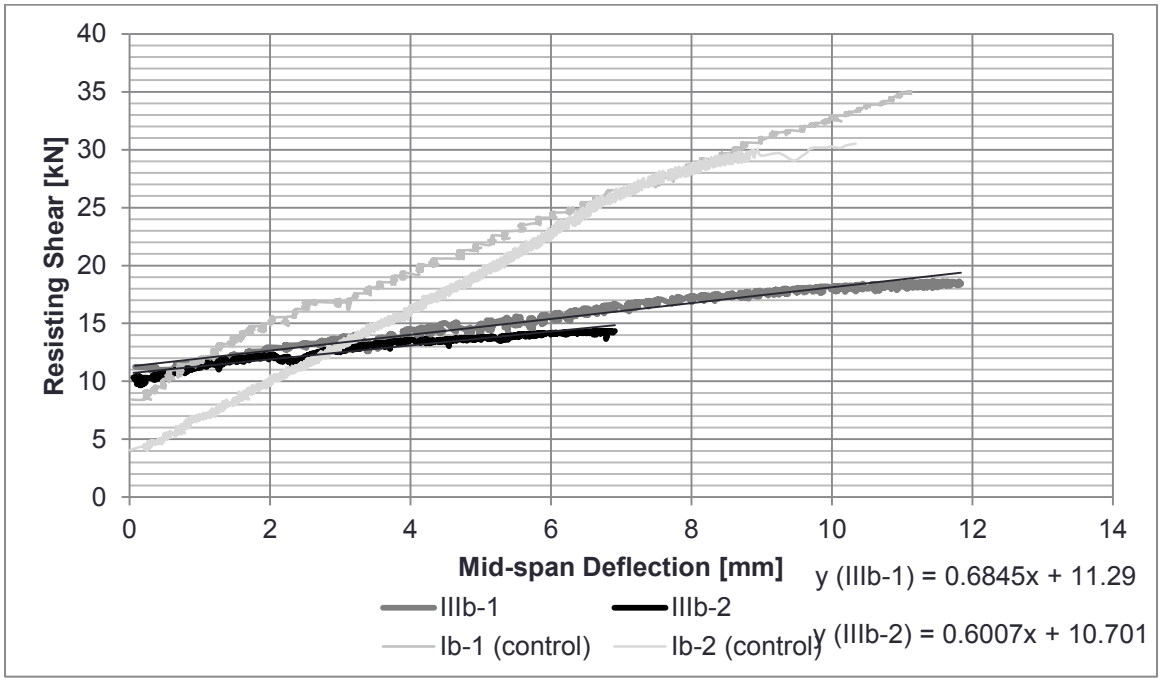

Figure C.6: IIIb Beam Deflection Curve

Reinforcement Elastic Modulus Index

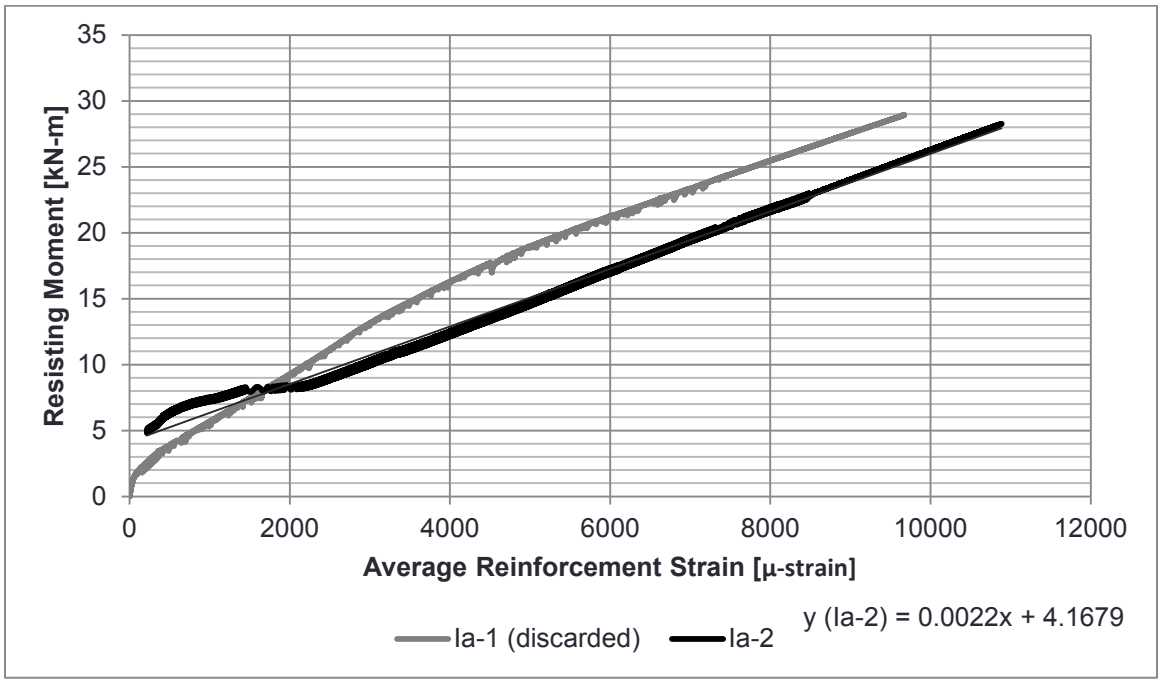

Figure C.7: Ia Reinforcement Elastic Modulus Index

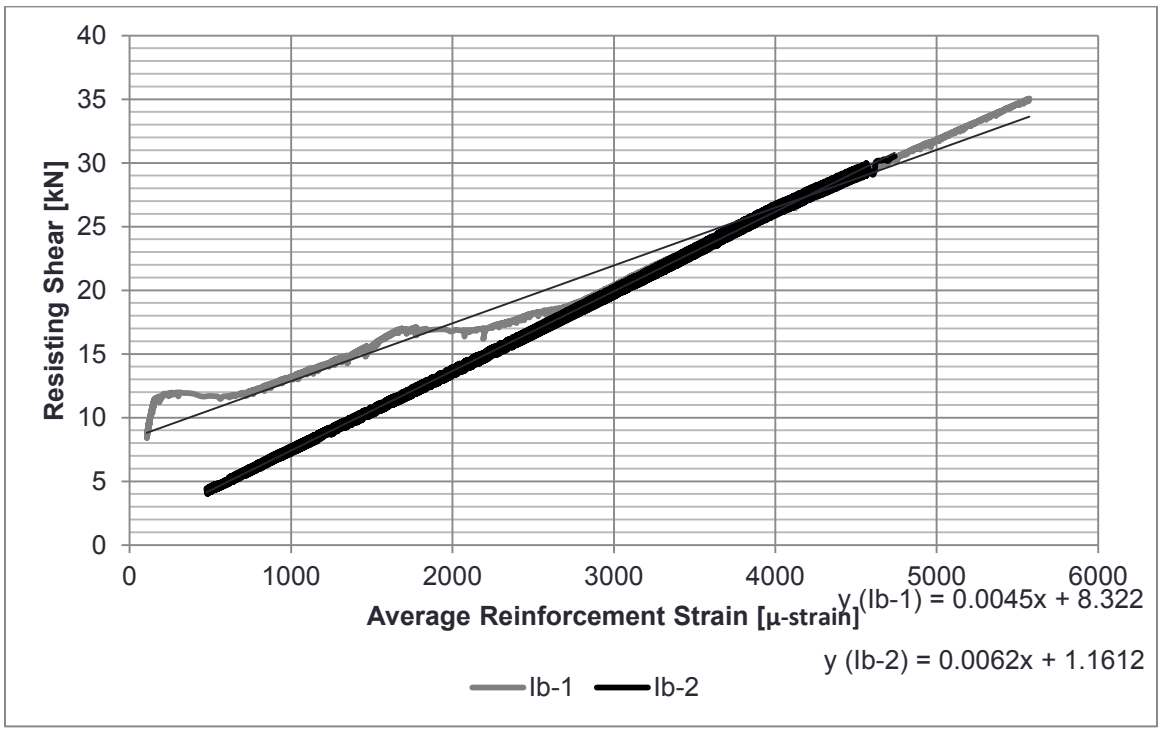

Figure C.8: Ib Reinforcement Elastic Modulus Index

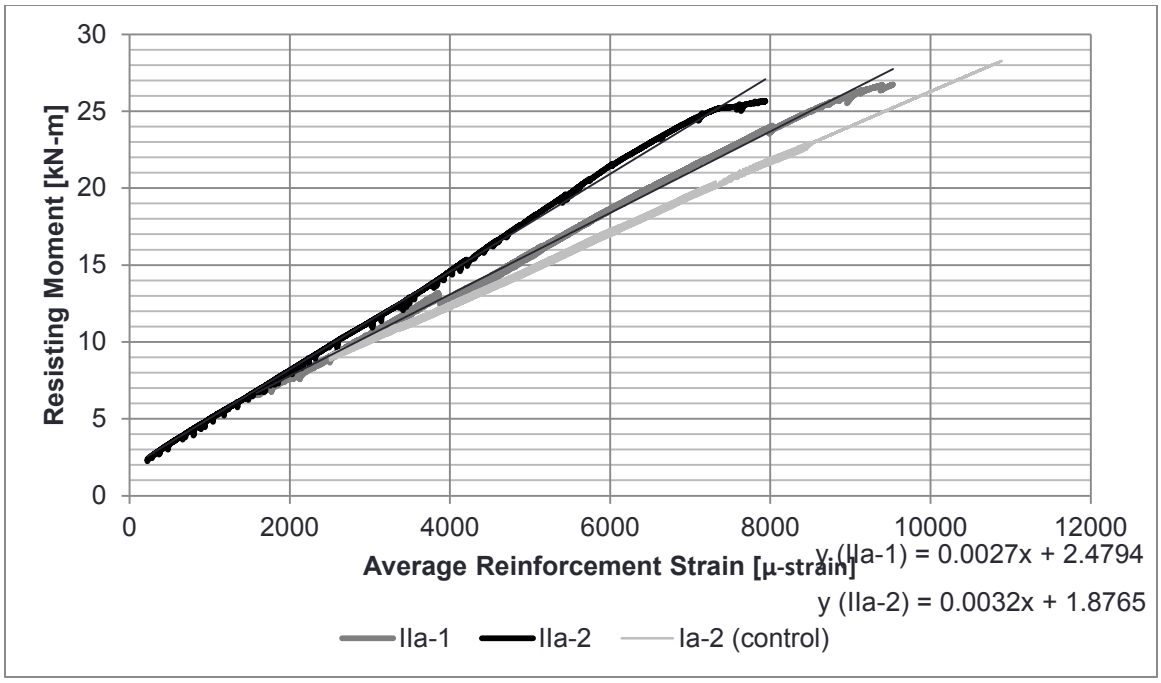

Figure C.9: IIa Reinforcement Elastic Modulus Index

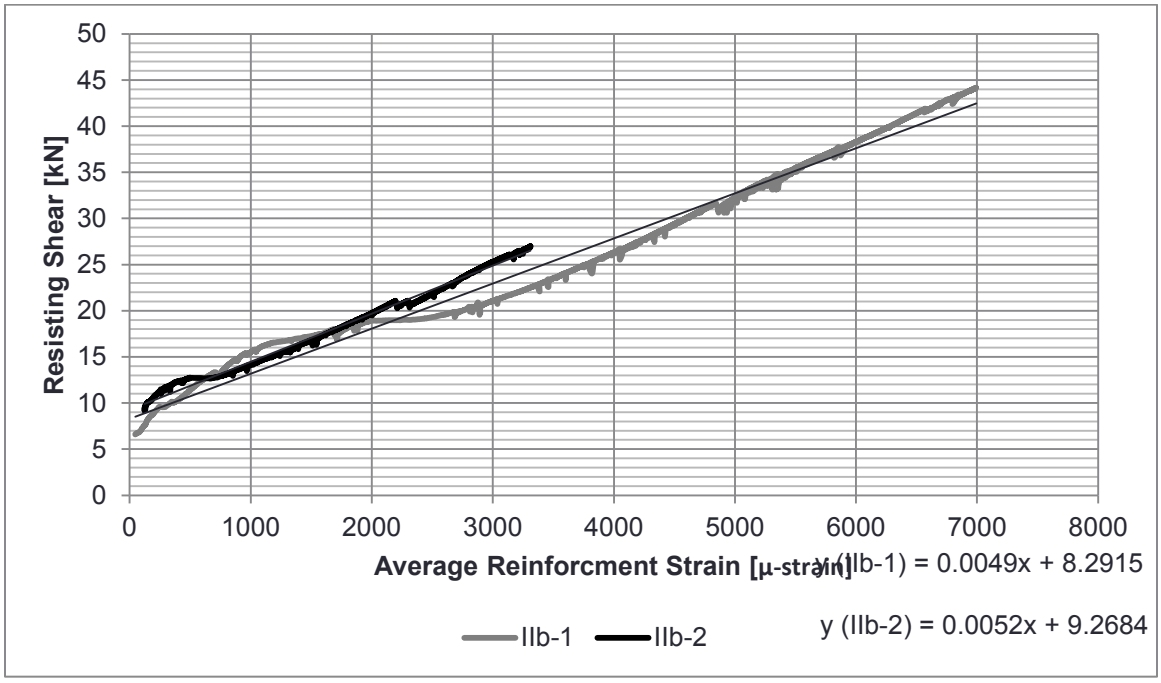

Figure C.10: IIb Reinforcement Elastic Modulus Index

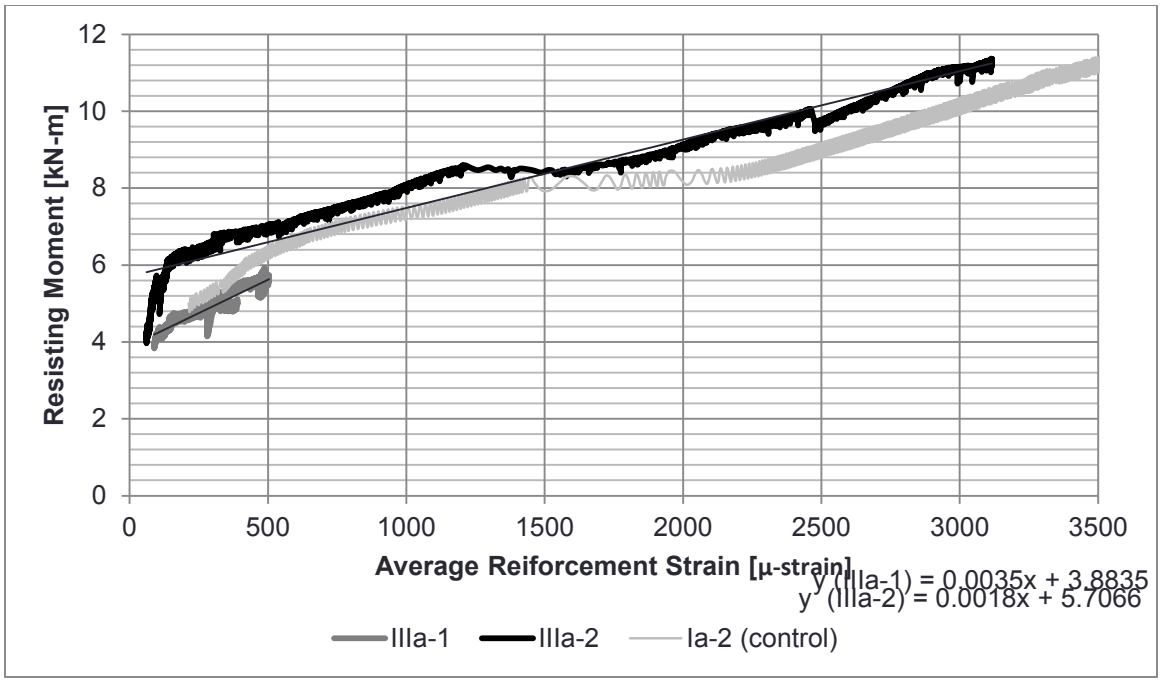

Figure C.11: IIIa Reinforcement Elastic Modulus Index

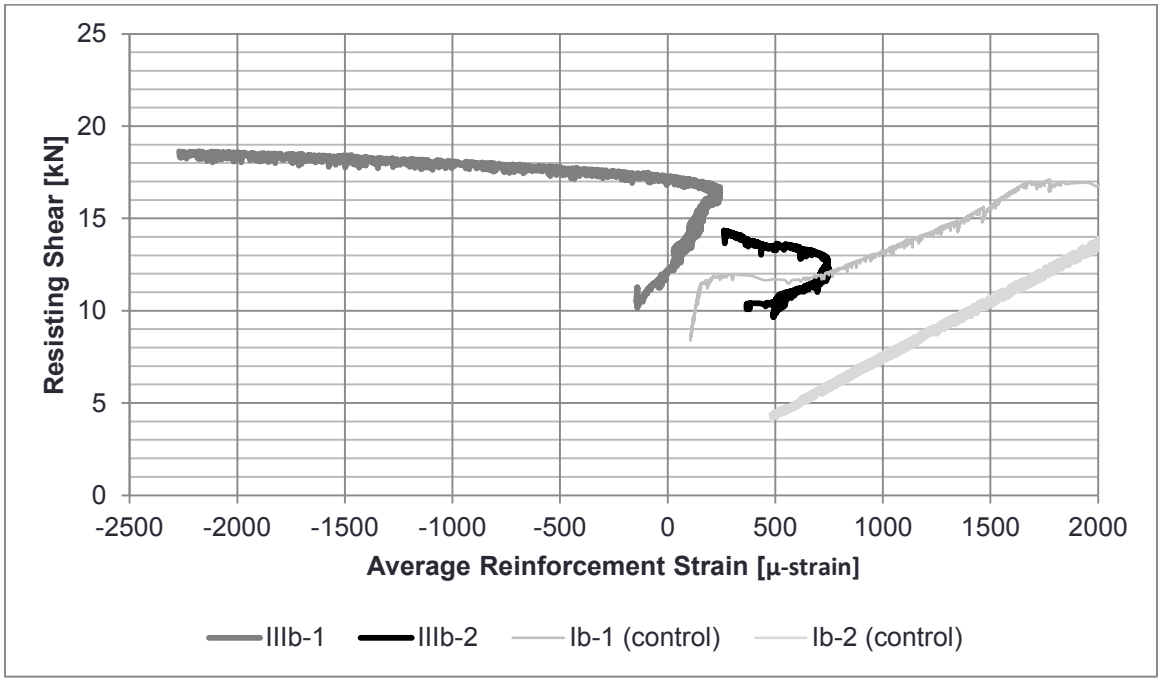

Figure C.12: IIIb Reinforcement Elastic Modulus Index

Appendix D – Section Analysis Photos

Figure D.1: Section cut A.1

Figure D.2: Section cut A.2

Figure D.3: Section cut B.1

Figure D.4: Section cut B.2

Figure D.5: Section cut C

Figure D.6: Section cut D

Figure D.7: Section cut E.1

Figure D.8: Section cut E.2

Figure D.9: Section cut F.1

Figure D.10: Section cut F.2